



JOHANNES GUTENBERG  
UNIVERSITÄT MAINZ

# **Effective equation of motion of a passive particle immersed in an active fluid**

written by

**Jeanine Shea**

This dissertation is submitted to the Faculty of Physics, Mathematics and  
Informatics of Johannes Gutenberg University Mainz for the degree of  
“Doctor of Natural Sciences”

Mainz, March 2023



# Abstract

Implicit models of passive, equilibrium systems have been used for many years to study and understand the physical behavior of such systems. Given the success of understanding equilibrium systems through such models, recent studies have focused on coarse-graining non-equilibrium systems. However, non-equilibrium systems are highly dependent on the system's dynamic properties, which are necessarily altered in a coarse-grained model. Furthermore, certain assumptions which are made in equilibrium coarse-grained modeling are no longer valid beyond equilibrium. Therefore, coarse-graining of non-equilibrium systems must be done with extreme care and consciousness of the true system dynamics.

Perhaps the most ubiquitous example of a coarse-grained model is the Brownian particle model, in which the motions of fluid particles surrounding a much larger, immersed particle are only implicitly represented to eliminate these degrees of freedom. In this thesis, we address the question: what happens when the fluid is far from equilibrium? We explore the dynamics of a passive probe particle immersed in an active bath and its implications for coarse-grained modeling. We use effective generalized Langevin equations, which explicitly include memory effects, to examine the immersed probe dynamics.

In the first part of this thesis, we classify the behaviors that signify the system's non-equilibrium nature. Although the probe adopts many active-particle-like behaviors, the trajectory of the probe does not exhibit obvious non-equilibrium signatures. To tell that the probe is out of equilibrium requires examination of its behavior *in tandem* with that of the active fluid. Alternatively, applying a small perturbation to the probe, reveals a violation of the first fluctuation dissipation theorem. In the second part of this thesis, we determine the mechanism behind the active-particle-like behavior of the probe. This behavior cannot simply be attributed to the convective motion of the active bath. Instead, the boundary of the probe contributes significantly to these adopted dynamics by causing active bath particles to accumulate behind the probe with respect to its instantaneous velocity. This gathering of active bath particles then pushes the probe, which in turn promotes its active-particle-like behavior. In the final part of this thesis, we map the dynamics of a probe immersed in an active bath and subject to an external force onto an equilibrium coarse-grained model. We find that this system can be mapped onto a physically meaningful coarse-grained model. However, due to the activity of the bath, the external force in such an equation is not equal to the physical external force, but rather a renormalized external force.



# Zusammenfassung

Implizite Modelle von passiven Gleichgewichtssystemen (GGS) werden seit vielen Jahren verwendet, um das physikalische Verhalten solcher Systeme zu untersuchen und zu verstehen. Angesichts dieses Verständniserfolges von GGS haben sich neuere Studien auf coarse-grained (cg) Nicht-Gleichgewichtssysteme (NGGS) konzentriert. NGGS sind jedoch in hohem Maße von dynamischen Eigenschaften des Systems abhängig, die in einem cg Modell zwangsläufig verändert werden. Außerdem sind bestimmte Annahmen der cg Modellierung von GGS jenseits des Gleichgewichts nicht mehr gültig. Daher muss die cg Modellierung von NGGS mit äußerster Sorgfalt und im Bewusstsein der tatsächlichen Systemdynamik durchgeführt werden.

Eins der bekanntesten Beispiele eines cg Modells ist das Brownsche Teilchenmodell. In diesem werden die Bewegungen von Flüssigkeitsteilchen, die ein viel größeres Teilchen umgeben, nur implizit dargestellt, um die Freiheitsgrade zu eliminieren. Hier beschäftigt uns die Frage: Was passiert, wenn das Bad weit vom Gleichgewicht entfernt ist? Wir untersuchen die Dynamik eines passiven Probeteilchen, das in ein aktives Bad eingetaucht ist, und deren Auswirkungen auf die cg Modellierung. Wir verwenden effektive verallgemeinerte Langevin-Gleichungen, die explizit Memory Effects einschließen, um die Dynamik der eingetauchten Probe zu untersuchen.

Im ersten Teil dieser Arbeit klassifizieren wir die Verhaltensweisen, die die Nicht-Gleichgewichtsnatur des Systems kennzeichnen. Obwohl die Probe viele Aktivteilchen-ähnliche Verhaltensweisen zeigt, weist die Flugbahn der Probe keine offensichtlichen Nicht-Gleichgewichtssignaturen auf. Um festzustellen, dass die Probe nicht im Gleichgewicht ist, muss ihr Verhalten im Tandem mit dem der aktiven Flüssigkeit untersucht werden. Alternativ kann eine kleine Störung der Probe eine Verletzung des ersten Fluktuationdissipationstheorems aufzeigen. Im zweiten Teil bestimmen wir den Mechanismus, der hinter dem Aktivteilchen-ähnlichen Verhalten der Probe steht. Dieses Verhalten kann nicht auf die konvektive Bewegung des aktiven Bades zurückgeführt werden. Stattdessen trägt die Begrenzung der Probe wesentlich zu der angenommenen Dynamik bei. Sie bewirkt, dass sich aktive Badteilchen hinter der Probe in Bezug auf ihre momentane Geschwindigkeit ansammeln. Diese Ansammlung aktiver Badteilchen schiebt die Probe an, was ihr Aktivteilchen-ähnliches Verhalten fördert. Im letzten Teil bilden wir die Dynamik einer in ein aktives Bad eingetauchten und einer äußeren Kraft ausgesetzten Probe auf ein cg Gleichgewichtsmodell ab. Wir sehen, dass das System auf ein physikalisch sinnvolles, cg Modell abgebildet werden kann. Aufgrund der Aktivität des Bades ist die äußere Kraft in einer solchen Gleichung jedoch nicht gleich der physikalischen äußeren Kraft, sondern eher eine renormierte äußere Kraft.



# Contents

<b>Abstract</b>	<b>1</b>
<b>Zusammenfassung</b>	<b>3</b>
<b>1 Introduction</b>	<b>9</b>
<b>I Background</b>	<b>12</b>
<b>2 The Langevin equation</b>	<b>13</b>
2.1 The Mori-Zwanzig formalism . . . . .	14
2.1.1 Calculation of the memory kernel and stochastic forces . . . . .	16
2.2 The second fluctuation dissipation theorem . . . . .	18
<b>3 The Fokker-Planck equation</b>	<b>19</b>
<b>4 Linear response theory</b>	<b>21</b>
<b>5 Microrheology</b>	<b>24</b>
<b>6 Active matter</b>	<b>25</b>
6.1 Active Brownian particle model . . . . .	26
6.2 Active Langevin particle model . . . . .	28
6.3 Collective behavior . . . . .	29
6.4 Boundary interactions . . . . .	32
6.5 Active-passive systems . . . . .	32
<b>7 Simulation details</b>	<b>34</b>
<b>II Non-equilibrium signatures of a passive probe in an active bath</b>	<b>36</b>
<b>8 Isolated active Langevin particle</b>	<b>38</b>
<b>9 Probe in an active Langevin particle bath</b>	<b>41</b>

9.1	Velocity distributions and autocorrelation functions . . . . .	42
9.2	Non-Markovian behavior of the probe . . . . .	44
9.3	Entropy production . . . . .	46
9.4	Response to small perturbations . . . . .	47
<b>10</b>	<b>Part II: conclusions and outlook</b>	<b>50</b>
<b>III</b>	<b>Boundary interactions of active matter with an immersed passive probe</b>	<b>52</b>
<b>11</b>	<b>Kinetic temperature</b>	<b>54</b>
<b>12</b>	<b>Transparent, convective probe</b>	<b>59</b>
<b>13</b>	<b>Spherical harmonics</b>	<b>63</b>
<b>14</b>	<b>Part III: conclusions and outlook</b>	<b>67</b>
<b>IV</b>	<b>Probe immersed in an active bath subject to external forces</b>	<b>69</b>
<b>15</b>	<b>Harmonic potential</b>	<b>71</b>
15.1	Position probability distribution . . . . .	71
15.2	Velocity autocorrelation function and memory kernel . . . . .	73
15.3	Stochastic force distribution . . . . .	74
15.4	Spherical harmonics . . . . .	76
<b>16</b>	<b>Drag force</b>	<b>78</b>
16.1	Static mobility . . . . .	79
16.2	Beyond linear response . . . . .	81
16.3	Velocity autocorrelation function and memory kernel . . . . .	81
16.4	Stochastic force distribution . . . . .	84
16.5	Spherical harmonics . . . . .	86
16.6	Effective drift force . . . . .	88
<b>17</b>	<b>Part IV: conclusions and outlook</b>	<b>89</b>
<b>18</b>	<b>Conclusions and outlook</b>	<b>90</b>
<b>A</b>	<b>Calculation of an isolated ALP VACF</b>	<b>91</b>
<b>B</b>	<b>Calculation of <math>P(\hat{v})</math></b>	<b>92</b>



B.1	From simulation data . . . . .	92
B.2	From the Fokker-Planck equation . . . . .	92
<b>C</b>	<b>Stochastic force distribution relative entropy</b>	<b>94</b>
<b>D</b>	<b>Test of linear response regime for perturbation force</b>	<b>95</b>
<b>E</b>	<b>1FDT for an isolated ALP</b>	<b>96</b>
<b>F</b>	<b>Velocity distribution for probes of different sizes</b>	<b>97</b>
<b>G</b>	<b>Active Langevin particle persistence length</b>	<b>99</b>
<b>H</b>	<b>Spherical harmonics calculation</b>	<b>101</b>
<b>I</b>	<b>Correlations and density in an active Langevin particle bath</b>	<b>102</b>
<b>J</b>	<b>Peclet number as a function of drag force</b>	<b>104</b>
	<b>Bibliography</b>	<b>105</b>
	<b>Acknowledgements</b>	<b>115</b>
	<b>Curriculum Vitae</b>	<b>116</b>
	<b>Publications</b>	<b>117</b>



# Introduction

The systems that we encounter in everyday life generally occur on macroscopic length scales, meaning that they consist of a number of particles at least on the order of magnitude of Avogadro's number. Consequently, it is intractable to derive their macroscopic behaviors from a microscopic starting point. However, some of the difficulties of deriving macroscopic behaviors can be mitigated if the system has processes which occur on different length and time scales.

In this case, the fast degrees of freedom in the system can be integrated out, under the assumption that their effects are irrelevant to the slow degrees of freedom. Most commonly, the interactions between the fast and slow degrees of freedom are then represented as stochastic noise and systematic dissipation rather than being explicitly calculated. This method is one type of *coarse-grained modeling*. One of the most common examples of this type of modeling is that of a large particle immersed in a fluid of significantly smaller particles. In this case, the motions of the fluid particles are only represented implicitly, rather than explicitly. This model is known as the *Brownian particle* model.

Such implicit models make studying the properties of macroscopic systems much more feasible because they greatly reduce the degrees of freedom in the system. Therefore, it is of great importance to find implicit models for systems of interest. However, in order to make implicit models that accurately represent the dynamics of a system, it is necessary to determine the form of the fluctuating and dissipative forces of that particular system, which requires careful consideration of its physical properties as well as data from experimental or explicit all-atom simulations. Furthermore, not all systems have dynamics which occur on well-separated time scales, in which case interactions between the fast and slow degrees of freedom are time dependent. Coarse grained models for such systems can still be constructed using the *Mori-Zwanzig formalism*, however, this method is only feasible for relatively simple systems.

In addition to being macroscopic, most systems that we encounter are *non-equilibrium*, i.e. they are subject to the continuous addition and/or dissipation of energy. Such systems pose a challenge for coarse-graining because they do not necessarily reach a stationary probability distribution and *fluctuation-dissipation relations* are no longer

guaranteed to be valid. Consequently, coarse-graining methods from equilibrium must be applied with care to non-equilibrium systems and thorough understanding of the system dynamics is necessary. One particular class of non-equilibrium systems is active matter systems, in which bodies within the system exhibit self-propulsion, thereby adding energy to the system. Such active systems exhibit significantly different behavior from passive systems due to their non-equilibrium nature; however, they are simple enough to model that they provide an excellent testing ground for coarse-grained models out of equilibrium.

To facilitate the understanding and further study of such systems, we investigate the stochastic and dissipative forces that are present in mixed passive and active systems. In particular, we investigate such forces in the system of a passive probe immersed in a bath of active particles. The first part of this thesis provides a literature review of relevant research areas. We first recapitulate previous work concerning stochastic, implicit modeling for equilibrium systems. In particular, we focus on the most common types of equations used to describe such models: Langevin (Chapter 2) and Fokker-Planck (Chapter 3) equations. In Chapter 2, we particularly emphasize systems which do not necessarily have well-separated time/length scales and, consequently, must be described by a generalized Langevin equation.

The success of implicit models relies on adequate knowledge of the stochastic and dissipative forces in a system. We therefore describe linear response theory in Chapter 4, which allows us to derive a direct relation between stochastic and dissipative forces. We furthermore introduce the field of microrheology in Chapter 5, which also enables the acquisition of stochastic and dissipative properties. Following this, in Chapter 6, we introduce the idea of active matter systems and highlight the research in this field which we find to be relevant to understanding the dynamics of our system. In Chapter 7, we describe the details of how we simulated our model system.

In the second part of this thesis, we investigate the non-equilibrium signatures of a passive probe immersed in an active bath. Given that previous studies have shown that a probe immersed in an active bath behaves like an active particle itself, we begin by diagnosing the non-equilibrium signatures of an active particles itself in Chapter 8. We then use these results to search for the non-equilibrium signatures of the probe in Chapter 9. We conclude this section in Chapter 10.

The third part focuses on understanding the mechanism through which a probe immersed in an active bath acquires properties similar to those of an active particle itself. Specifically, we aim to disentangle the convective properties of the active bath from those which are resultant of boundary interactions. We therefore expand our

study to encompass probes of different sizes and examine their kinetic temperature in Chapter 11. To isolate the bath's convective properties, we study a transparent, convective probe immersed in an active bath in Chapter 12. We then assess the importance of boundary interactions by calculating the spherical harmonics of the bath in the vicinity of the probe in Chapter 13. We conclude this section in Chapter 14.

In the fourth and final part, we subject a probe immersed in an active bath to two types of external forces which are highly relevant to microrheological studies: a harmonic, trapping force in Chapter 15 and a constant, 'drag' force in Chapter 16. We then map the dynamics of these probes to a coarse-grained model and gauge the physical implications of such a mapping. We conclude this section in Chapter 17. In Chapter 18, we summarize our findings and conclude with an outlook on future research.

# Part I

---

Background

## The Langevin equation

Implicit models eliminate fast degrees of freedom and only explicitly represent slow processes in the system. However, they maintain dynamics which are largely similar to those of the original system through the addition of random, stochastic noise and systematic, dissipative forces. These forces mimic the effects of the ‘irrelevant,’ fast variables in the explicit system. One of the most famous and well studied examples of this type of modeling is that of Brownian motion [1, 2, 3, 4, 5]. The Brownian particle model describes a large particle which is immersed in a solvent fluid made up of significantly smaller particles. Due to the difference in size between the solvent particles and the immersed particle, the time scales associated with the solvent fluid are fast compared to those of the immersed particle. The random collisions between the immersed particle and the solvent fluid particles can be represented by stochastic noise and a linear dissipative term. The equation of motion associated with the dynamics of the larger, immersed ‘Brownian’ particle is known as the Langevin equation [5]:

$$m\dot{\mathbf{v}}(t) = -\gamma\mathbf{v}(t) + \mathbf{\Gamma}(t), \quad (2.1)$$

where  $m$  is the mass of the larger, immersed particle and  $\mathbf{v}$  is its velocity. For a particle of radius  $R$  immersed in a fluid with viscosity  $\eta$ , the damping constant is  $\gamma = 6\pi\eta R$  [6]. From this damping constant, we can also define a translational diffusion coefficient  $D_T = \frac{k_B T}{\gamma}$  using the Stokes–Einstein relation [7, 8]. The first term on the right-hand side of Eq. (2.1) represents the dissipative, damping force on a particle from the fast degrees of freedom. The second term of Eq. (2.1) represents the fluctuating, stochastic force on a particle from these same degrees of freedom. In the physical picture, this term mimics the occasional collisions between the immersed and solvent particles. The stochastic force ( $\mathbf{\Gamma}(t)$ ) can be represented by Gaussian white noise such that:

$$\langle \mathbf{\Gamma}(t) | \mathbf{\Gamma}(t') \rangle = 0 \quad \langle \mathbf{\Gamma}_i(t) | \mathbf{\Gamma}_j(t') \rangle = 2\gamma k_B T \delta_{ij} \delta(t - t'). \quad (2.2)$$

## 2.1 The Mori-Zwanzig formalism

However, Eq. (2.1) assumes that there is a perfect separation of times scales, essentially assuming that the mass of the immersed large particle is infinite compared to that of the smaller bath particles. In this case, the system is ‘Markovian,’ meaning that its future dynamics are governed only by its current state, i.e. it has no ‘memory.’ Systems which do not have a perfect separation of time scales are ‘Non-Markovian’ and the memory of the system is important in determining future behavior.

To include memory effects in implicit models of systems in which there is not a perfect separation of time scales, we can use the Mori-Zwanzig projection operator formalism [9, 10, 11, 12]. The Mori-Zwanzig formalism assumes a system of  $N$  particles defined by the Hamiltonian equations of motion:

$$\begin{aligned}\dot{\mathbf{q}}_i &= \frac{\partial \mathcal{H}}{\partial \mathbf{p}_i} \\ \dot{\mathbf{p}}_i &= -\frac{\partial \mathcal{H}}{\partial \mathbf{q}_i},\end{aligned}\tag{2.3}$$

for a particle  $i$  in a system with Hamiltonian  $\mathcal{H}$  where variables  $\xi = \{\{\mathbf{q}_i\}, \{\mathbf{p}_i\}\}$  describe the phase space of the system. The time dependence of any relevant variable in the system,  $\{A_i(\xi)\}$ , is:

$$\frac{d}{dt}A_i(\xi(t)) = \sum_i \left[ \frac{\partial \mathcal{H}}{\partial \mathbf{p}_i} \frac{\partial}{\partial \mathbf{q}_i} - \frac{\partial \mathcal{H}}{\partial \mathbf{q}_i} \frac{\partial}{\partial \mathbf{p}_i} \right] A_i(\xi) \equiv \mathcal{L}A_i,\tag{2.4}$$

where  $\mathcal{L}$  is the Liouville operator, which describes the evolution of the phase space probability distribution over time. For simplicity of the derivation, we assume that  $A_i$  is a scalar; however, this derivation can easily be extended to vector variables. The solution of Eq. (2.4) is:

$$A_i(t) = \exp(\mathcal{L}t)A_i(0).\tag{2.5}$$

Now, for illustrative purposes, we assume our system is in equilibrium such that its phase space variables are Boltzmann distributed according to:

$$\rho(\xi) = \frac{\exp(-\beta\mathcal{H}(\xi))}{\int d\xi \exp(-\beta\mathcal{H}(\xi))},\tag{2.6}$$

where  $\beta = 1/k_B T$ . However, this assumption is not necessary for the Mori-Zwanzig formalism. The Mori-Zwanzig formalism only requires that the stochastic process is



stationary, i.e. the system can be described with a probability density and stochastic equations of motion which do not explicitly depend on time.

With the probability density of our system, as described in Eq. (2.6), we can then define a scalar product between system observable  $A$  and  $B$ ,

$$\langle A_i|B \rangle = \int d\xi \rho(\xi) A_i(\xi) B^*(\xi), \quad (2.7)$$

to determine the correlation between the two observables. From this definition we can then define a projection operator  $\mathcal{P}$  which can be used to differentiate between relevant and irrelevant dynamic variables. Acting  $\mathcal{P}$  on another observable of the system,  $B$ , gives:

$$\mathcal{P}B = \sum_i \sum_j \langle A_j|B \rangle \left[ \langle A|A \rangle^{-1} \right]_{ij} A_i, \quad (2.8)$$

which projects the selected observable on the entire space of relevant variables  $\{A_i\}$ . The converse projector,  $\mathcal{Q} = 1 - \mathcal{P}$ , consequently projects an observable onto the entire space of irrelevant variables. With these definitions of  $\mathcal{P}$  and  $\mathcal{Q}$  combined with Eq.(2.4), after some transformations, we can write [9, 13]:

$$\frac{d}{dt} A_i(\xi(t)) = i\Omega_{ji} A_j(t) - \int_0^t ds K_{ji}(t-s) A_j(s) + \Gamma_i(t). \quad (2.9)$$

The first term of Eq. (2.9) represents the direct interactions between relevant observables, where we define the frequency matrix of the relevant variable interactions,  $i\Omega_{ij}$ , as:

$$i\Omega_{ji} = -\langle A_k|\mathcal{L}A_j \rangle \left[ \langle A|A \rangle^{-1} \right]_{ik}. \quad (2.10)$$

Because the Mori-Zwanzig formalism is a linear theory, non-linear interaction forces and dissipative terms are absorbed in the random force term and a renormalized memory kernel. This linearization is not always desirable; therefore, a number of modified projection operator formalisms have been proposed [13, 14, 15, 16]. Since the particle described in Eq. (2.1) is not subject to a potential, this term has no analogous counterpart in Eq. (2.1).

The third term of Eq. (2.9) corresponds to the random fluctuations of the force due to interactions between relevant and irrelevant variables. This term is analogous to the stochastic force of Eq. (2.1) and is given by:

$$\Gamma_i(t) = \exp(\mathcal{Q}\mathcal{L}t) \mathcal{Q}\mathcal{L}A_i. \quad (2.11)$$

The second term of Eq. (2.9) corresponds to the dissipative forces due to interactions between the relevant and irrelevant variables, where

$$K_{ji}(t) = \langle \mathcal{L}A_k | \Gamma_i(t) \rangle \left[ \langle A | A \rangle^{-1} \right]_{jk}. \quad (2.12)$$

This is analogous to the dissipative term of Eq. (2.1),  $-\gamma \mathbf{v}(t)$ . The form of the dissipative term in Eq. (2.1) is only valid in the limit that there is a perfect separation of time scales.

In the case that time scales are not perfectly separated, when we consider observables  $\{\mathbf{A}_i\}$  to be the position and velocity of a particle, Eq. (2.9) can no longer be approximated as Eq. (2.1), but instead as:

$$M \dot{\mathbf{V}}(t) = - \int_0^t ds K(t-s) \mathbf{V}(s) + \mathbf{\Gamma}(t), \quad (2.13)$$

where  $M$  is the particle mass,  $\mathbf{V}(t)$  is its velocity,  $K(t-s)$  is the memory kernel, and  $\mathbf{\Gamma}(t)$  is the stochastic force. This equation is known as the generalized Langevin equation (GLE). In this equation we have again assumed that the particle is not subject to external forces, so the first term of Eq. (2.9) is eliminated. The second term, analogously to Eq. (2.9), is the friction force. The important difference to note between the friction of Eq. (2.13) and that of Eq. (2.1) is that, in Eq. (2.13), the friction force depends on the entire history, or ‘memory,’ of the particle. This dependence is because of the non-Markovian nature of the system. The third and final term again represents the random collisions of the particle with the implicit bath.

### 2.1.1 Calculation of the memory kernel and stochastic forces

While there have been many techniques created to extract the memory kernel from simulations [17, 18, 19, 20, 21, 22, 23, 24], we use the technique proposed by Shin et al. [17], which we will refer to as the inverse Volterra technique, because this is the most direct method of extraction. This technique relies on transforming Eq. (2.13) into the Volterra equation:

$$M \dot{C}_V(t) = - \int_0^t ds K(t-s) C_V(s), \quad (2.14)$$

where  $C_V(t) = \frac{1}{\mathcal{T}} \int_0^{\mathcal{T}} ds \mathbf{V}(t+s) \mathbf{V}(t'+s)$  in the limit  $\mathcal{T} \rightarrow \infty$  is the velocity autocorrelation function (VACF). The transformation of Eq. (2.13) into Eq. (2.14)

is done simply by multiplying Eq. (2.13) by  $\mathbf{V}(0)$ . It is important to note that Eq. (2.14) is free of stochastic noise because, by definition, the stochastic noise must be orthogonal to all relevant variables; thus,  $\langle \mathbf{\Gamma}(t) | \mathbf{V}(0) \rangle = 0$ .

Although this equation itself can already theoretically be inverted to determine the memory kernel, Shin et al. [17] showed that it is more stable to invert a Volterra equation of the second kind. We can obtain such an equation by taking the time derivative of Eq. (2.14), from which we find,

$$M\ddot{C}_V(t) = -C_V(0)K(t) - \int_0^t ds K(s)\dot{C}_V(t-s). \quad (2.15)$$

We can then identify the time derivatives of the VACF as:

$$\begin{aligned} \dot{C}_V(t) &= \frac{1}{M} \langle \mathbf{F}(t) | \mathbf{V}(0) \rangle = \frac{1}{M} C_{FV}(t) \\ \ddot{C}_V(t) &= -\frac{1}{M^2} \langle \mathbf{F}(t) | \mathbf{F}(0) \rangle = -\frac{1}{M^2} C_F(t), \end{aligned} \quad (2.16)$$

the velocity-force correlation function (VFCF) and the force-autocorrelation function (FACF) of the particle, respectively.

From these correlation functions, we can reconstruct the memory kernel of the colloid directly from our simulation data [17]:

$$K(j\Delta t) = \frac{\frac{1}{M} C_F(j\Delta t) - \frac{\Delta t}{M} \sum_{k=0}^{j-1} \omega_k C_{FV}((j-k)\Delta t) K(k\Delta t)}{C_V(0) + \frac{\Delta t \omega_j}{M} C_{FV}(0)}, \quad (2.17)$$

where  $\Delta t$  is the time resolution of the correlation function calculated from the simulation and  $\omega_j$  is a weight factor such that:

$$\omega_j = \begin{cases} \frac{1}{2} & j = 0 \\ 1 & j \neq 0. \end{cases} \quad (2.18)$$

In addition to Eq. (2.17), we also know the initial condition that  $MK(0) = \frac{C_F(0)}{C_V(0)}$ .

After reconstructing the memory kernel, we can exploit this knowledge to find the stochastic noise of the system. We can do this by a trivial re-ordering of Eq. (2.13) as [17]:

$$\mathbf{\Gamma}(t) = \mathbf{F}(t) + \int_0^t ds K(t-s) \mathbf{v}(s), \quad (2.19)$$

where  $\mathbf{F}(t)$  is the instantaneous force acting on the particle, which is calculated during the simulated trajectory. Thus, from Eq. (2.19), we can examine the properties of the stochastic force.

## 2.2 The second fluctuation dissipation theorem

The dissipative and stochastic terms of Eq. (2.9) (thus Eq. (2.13) as well) can be related through the Mori-Zwanzig formalism [9, 11, 10, 13] by inserting Eq. (2.11) into Eq. (2.12). This relation is known as the second fluctuation dissipation theorem (2FDT) [25]:

$$\langle \mathbf{\Gamma}_i(0) | \mathbf{\Gamma}_j(t) \rangle = K_{ik}(t) \langle A_k | A_j \rangle. \quad (2.20)$$

When this relation is applied to the dynamics of Eq. (2.1), we recover Eq. (2.2). In the case of the GLE (Eq. (2.13)), we can formulate the 2FDT as:

$$\langle \mathbf{\Gamma}(0) | \mathbf{\Gamma}(t) \rangle = M \langle |\mathbf{V}|^2 \rangle K(t). \quad (2.21)$$

Although the validity of the 2FDT in non-equilibrium systems has been controversial in literature [26, 27, 28, 29, 30, 31, 32], it can be explicitly shown that, if the correlation function is described by an inverse Volterra equation such as Eq. (2.14), then Eq. (2.21) *must* hold [33].

## The Fokker-Planck equation

In Chapter 2, we described the dynamics of a Brownian particle through its individual trajectory. However, we would now like to change lenses and describe its evolution through a probability density,  $\mathcal{P}(\mathbf{x}, t)$ , where  $\mathbf{x}$  is some observable. In order to make this jump to a probability density, we will need to make three assumptions: that our process is Markovian (i.e. it is described by Eq. (2.1) rather than Eq. (2.13)), that our process is stationary, and that the noise is white and Gaussian distributed.

Because the probability distribution is a conserved quantity, we know its time derivative must be balanced by a flux. Therefore, for a stationary, Markov process we can write down that:

$$\frac{\partial \mathcal{P}(\mathbf{x}, t)}{\partial t} = \int dx' \mathcal{P}(\mathbf{x}', t) R(\mathbf{x}, \mathbf{x}') - \int dx' \mathcal{P}(\mathbf{x}, t) R(\mathbf{x}', \mathbf{x}), \quad (3.1)$$

where  $R(\mathbf{x}, \mathbf{x}')$  is the transition rate between two states. This equation essentially states that the change in the probability distribution is equal to the difference between the flow in and the flow out. Assuming that it is unlikely for a large jump in space to occur (i.e.  $R(\mathbf{x}, \mathbf{x}') \approx 0$  for large  $(\mathbf{x} - \mathbf{x}')$ ), then we can rewrite Eq. (3.1) as an expansion:

$$\frac{\partial \mathcal{P}(\mathbf{x}, t)}{\partial t} = \sum_{k=1}^{\infty} \frac{(-1)^k}{k!} \frac{\partial^k}{\partial \mathbf{x}^k} [\alpha_k(\mathbf{x}) \mathcal{P}(\mathbf{x}, t)], \quad (3.2)$$

where  $\alpha_k(\mathbf{x}) = \int d\epsilon \epsilon^k \tilde{R}(\epsilon, \mathbf{x})$  and  $R(\mathbf{x}, \mathbf{x}') =: \tilde{R}(\mathbf{x} - \mathbf{x}', \mathbf{x}')$  for a small variation,  $\epsilon$ . This is known as the Kramers-Moyal expansion [34, 35].

If we now assume that  $R(\mathbf{x}, \mathbf{x}')$  only varies slowly as a function of  $\mathbf{x}$  and, therefore,  $\mathcal{P}(\mathbf{x}, t)$  also varies slowly, then we can cut off the expansion after the second moment. This results in the Fokker-Planck equation:

$$\frac{\partial \mathcal{P}(\mathbf{x}, t)}{\partial t} = -\frac{\partial}{\partial \mathbf{x}} (\alpha_1(\mathbf{x}) \mathcal{P}(\mathbf{x}, t)) + \frac{1}{2} \frac{\partial^2}{\partial \mathbf{x}^2} (\alpha_2(\mathbf{x}) \mathcal{P}(\mathbf{x}, t)). \quad (3.3)$$

When Eq. (3.3) is applied to the dynamics of Eq. (2.1), then the resulting Fokker-Planck equation for the probability density  $\mathcal{P}(\mathbf{x}, \mathbf{v}, t)$  is:

$$\frac{\partial \mathcal{P}(\mathbf{x}, \mathbf{v}, t)}{\partial t} = -\frac{\partial}{\partial \mathbf{x}} (\mathbf{v} \mathcal{P}(\mathbf{x}, \mathbf{v}, t)) + \frac{\partial}{\partial \mathbf{v}} \left( \frac{\gamma}{m} \mathbf{v} \mathcal{P}(\mathbf{x}, \mathbf{v}, t) \right) + \frac{\gamma k_B T}{m^2} \frac{\partial^2 \mathcal{P}(\mathbf{x}, \mathbf{v}, t)}{\partial \mathbf{v}^2}. \quad (3.4)$$

We would once again like to emphasize that Eqs. (2.1) and (3.4) describe the same dynamics, just through different lenses. Whereas Eq. (2.1) describes the dynamics through a single trajectory, Eq. (3.4) describes the dynamics through the evolution of the probability distribution over time. In order to move to the probability distribution picture given by the Fokker-Planck equation, it is necessary to assume that the system is Markovian. Therefore, the Fokker-Planck equation cannot describe systems without perfect time scale separation. Such systems must instead be described by a Langevin-type equation, in particular Eq. 2.9 of Section 2.1.

## Linear response theory

The response function of a system relates the change of an ensemble-averaged observable to an external, perturbing force. The goal of linear response theory is to determine the dynamical response function of an observable ( $\delta Y(t)$ ) to a small perturbation ( $\alpha(t)$ ), where  $\alpha(t)$  is sufficiently small that  $\delta Y(t)$  scales linearly with  $\alpha(t)$ . The linear response of a classical system can be derived in a variety of manners (see e.g. Refs. [9, 36, 37]). Here we follow the derivation of Ref. [9].

We assume that the system is initially (for  $t < 0$ ) characterized by an equilibrium Hamiltonian  $H_0(\xi)$  with phase space variable  $\xi$ . Thus, the system has an unperturbed distribution function:

$$f_{\text{eq}}(\xi) = \frac{1}{Z} e^{-\beta H_0(\xi)}; \quad Z = \text{Tr} e^{-\beta H_0(\xi)}, \quad (4.1)$$

where  $Z$  is the partition function and  $\beta = 1/k_B T$ . The perturbed Hamiltonian is then  $H(\xi, \alpha) = H_0(\xi) - \alpha(t)X(\xi)$ , where  $X(\xi)$  is another system observable.

Due to the time dependence of the perturbation, the distribution function is also now time dependent ( $f(\xi, t)$ ) and evolves according to the Liouville equation:

$$\begin{aligned} \frac{\partial f}{\partial t} &= -\{f, H\} \\ &= -\mathcal{L}_0 f - \mathcal{L}_1 \alpha(t) f. \end{aligned} \quad (4.2)$$

Here,  $\mathcal{L}_0$  is the unperturbed Liouville operator and  $\mathcal{L}_1$  is the Liouville operator of the perturbation.  $\mathcal{L}_0 f$  is the Poisson bracket of  $H_0$  and  $f$ ;  $\mathcal{L}_1 f$  is the Poisson bracket of  $-X$  and  $f$ .

Since we only want to find the first order response of the system, we now do a first order expansion of  $f$  in powers of  $\alpha(t)$ :

$$f = f_0 + f_1 + \mathcal{O}(\alpha^2), \quad (4.3)$$

where  $f_0$  and  $f_1$  are the zeroth and first order terms respectively. Plugging Eq. (4.3) into Eq. (4.2), we can now write two separate equations for the zeroth and first order terms:

$$\frac{\partial f_0}{\partial t} = -\mathcal{L}_0 f_0, \quad (4.4)$$

$$\frac{\partial f_1}{\partial t} = -\mathcal{L}_0 f_1 - \mathcal{L}_1 \alpha(t) f_0. \quad (4.5)$$

Because the system starts in equilibrium,  $\alpha(t)$  vanishes for  $t < 0$ . Therefore, Eqs. (4.4) and (4.5) are subject to the initial conditions:

$$f_0(0) = f_{\text{eq}}; \quad f_1(0) = 0. \quad (4.6)$$

We know that  $\mathcal{L}_0 f_{\text{eq}} = 0$ . Thus, solving Eq. 4.4,  $f_0(t) = f_{\text{eq}}$  for all values of  $t$ .

Eq. (4.5) is an inhomogenous first-order differential equation with a vanishing initial value. Consequently, we can write down the solution:

$$f_1(t) = - \int_0^t ds e^{-(t-s)\mathcal{L}_0} \mathcal{L}_1 \alpha(s) f_0(s). \quad (4.7)$$

We can immediately substitute  $f_{\text{eq}}$  for  $f_0(s)$  from our solution to Eq. 4.4. Now, explicitly writing the Poisson bracket  $\mathcal{L}_1 f_{\text{eq}}$  and using the known distribution  $f_{\text{eq}}$ , we can write:

$$\mathcal{L}_1 \alpha(s) f_{\text{eq}} = -\beta \alpha(s) \dot{X} f_{\text{eq}}. \quad (4.8)$$

Thus, Eq. (4.7) becomes:

$$f_1(t) = \int_0^t ds \beta \alpha(s) e^{-(t-s)\mathcal{L}_0} \dot{X} f_{\text{eq}}. \quad (4.9)$$

We can now use these results to find the time-dependent fluctuations of observable  $Y$ :

$$\begin{aligned} \delta Y(t) &= Y(t) - \langle Y_{\text{eq}} \rangle \\ &= \int_0^t ds \beta \alpha(s) \int d\xi Y(\xi) e^{-(t-s)\mathcal{L}_0} \dot{X} f_{\text{eq}}, \end{aligned} \quad (4.10)$$

where  $\langle Y_{\text{eq}} \rangle$  is the equilibrium average of observable  $Y$ . We can now operate the Liouville operator backwards on  $Y$ . The phase space integral then simply generates an equilibrium average such that:

$$\delta Y(t) = \beta \int_0^t ds \alpha(s) \langle Y(t-s) \dot{X}(0) \rangle_{\text{eq}} + \dots, \quad (4.11)$$



where we ignore higher order terms. This equation suggests that we define the time dependent susceptibility:

$$\phi_{XY}(t) = \beta \langle Y(t) \dot{X}(0) \rangle_{\text{eq}}. \quad (4.12)$$

Now we can finally write down the standard linear response equation [38]:

$$\delta Y(t) = \beta \int_0^t ds \phi_{XY}(s) \alpha(t-s), \quad (4.13)$$

where we have again disregarded higher orders of  $\alpha$ .

This relation is also known as the first fluctuation dissipation theorem (1FDT). The 1FDT relates the non-equilibrium response of an observable to some small perturbation to the equilibrium relaxation of that observable. This is in contrast to the 2FDT (see Section 2.2), which connects dissipative interactions in a system with stochastic noise in the same system. It has been previously shown that the 1FDT will hold even in a non-equilibrium steady-state, provided certain assumptions which imply that the system remains close to equilibrium [39, 40, 41].

## Microrheology

Rheology is the study of the deformation and flow of matter, in particular through the observation of macroscopic behaviors. For example, a typical rheological study may aim to quantify the viscoelastic properties of a complex fluid by relating its stresses and strains [42]. Microrheology, on the other hand, focuses on linking the microscopic dynamics of a system to its macroscopic response. These studies primarily use the behavior of a immersed probe particle to gain knowledge about the surrounding medium [43, 44, 45].

In general, microrheological studies can be classified in two categories: passive and active [46, 47]. Passive microrheology monitors the diffusive motion of an immersed probe to gain knowledge about the (thermal) fluctuations in the medium. For example, the Stokes-Einstein relation relates the diffusion of a spherical probe to the viscosity of the medium in which it is immersed [7, 8]. Active microrheology either measures the mobility of the probe, by applying a constant external force, or measures the frequency dependence of the mobility, by applying an oscillating external force.

In the case of a probe subject to a constant external force, the average force exerted on the probe ( $\langle F \rangle$ ) can be related to its average velocity ( $\langle V \rangle$ ) by the equation:

$$\langle V \rangle = \mu \langle F \rangle, \quad (5.1)$$

where  $\mu$  is the mobility of the probe. Within the linear response regime, the results of passive and active microrheology are related and consistent with one another. However, unlike passive microrheology, active microrheology extends beyond the linear response regime, at which point the mobility becomes dependent on the external pulling force. Beyond the linear response regime, both ‘thinning’ (increased mobility) [48, 49, 50, 51, 52] and thickening (decreased mobility) [50, 52, 53, 54] behavior have been observed for different systems.

## Active matter

Active matter systems have recently gained popularity as exemplary non-equilibrium systems. Active matter systems are characterized by the fact that (at least some) constituent bodies are autonomous and add energy to the system as directed motion. As such, the total momentum of two active bodies before and after a collision is not necessarily the same [55]. Examples of active bodies range all the way from the microscopic example of bacteria, to the macroscopic example of birds, or even people.

Many different models of active bodies have been proposed to mimic behaviors of different real-life systems. Generally, these models all share the fact that they assign each active body an orientation along which it propels itself. However, they differ in the manner in which the orientation of these bodies changes. For example, one of the first active matter models, the Vicsek model [56], aligns a particle's orientation based on the average orientation of its neighbors. The run-and-tumble model of an active particle, based largely on the experimental behavior of bacteria [57], consists of a random walk with two distinct actions: the run, in which the particle moves in a straight line with a constant speed, and the tumble, in which the particle reorients itself according to a Poisson-distribution [58]. Perhaps the simplest active particle model is the active Brownian particle (ABP) model. This model consists of an overdamped Brownian particle, which propels itself at a constant speed and whose orientation is subject to thermal rotational diffusion [58].

Recently, studies have additionally considered the active Langevin particle (ALP) model, in which an underdamped Brownian particle propels itself with a constant force, the orientation of which is subject to thermal rotational diffusion [59, 60, 61, 62, 63, 64, 65, 66]. This model is very similar to the ABP model, except the particle is underdamped rather than overdamped.

In general, the propulsion force of ABPs and ALPs can be regarded as a form of 'active noise;' however, this 'active noise' must be distinguished from the white noise assumed in Langevin equations for passive particles. Unlike white noise, the magnitude of the propulsion speed is bounded by the value of  $v_0$  (for ALPs, propulsion force  $F_0$ ). Furthermore, the propulsion speed (force) has an exponentially

decaying autocorrelation function and its different components  $(x, y, z)$  are correlated with each other [67].

In the following sections, we consider the last two of these models, the ABP and ALP models, in more detail. In particular, we elaborate on the equations of motion for these models (ABPs: Section 6.1, ALPs: Section 6.2), the collective behavior of such particles (Section 6.3), and how such active particles interact with boundaries (Section 6.4) and passive particles (Section 6.5) in the same system. We specifically consider the dynamics of spherical ABPs and ALPs. Although we particularly highlight these two active particle models, many of their phenomenological behaviors (e.g. motility-induced phase separation) are widely generalizable to other active particle models [68].

## 6.1 Active Brownian particle model

ABPs are overdamped particles which propel themselves with a velocity of a constant magnitude, whose orientation changes with thermal rotational diffusion. Although such particles are not subject to hydrodynamic interactions, they are subject to random fluctuations of an implicit bath. The equation of motion for an isolated ABP is [59]:

$$\dot{\mathbf{r}}(t) = v_0 \mathbf{e}(t) + \boldsymbol{\xi}(t) \quad (6.1)$$

where  $v_0$  is the ABP propulsion velocity and  $\mathbf{e}(t)$  is its orientation.  $\boldsymbol{\xi}(t)$  is Gaussian distributed white noise with a variance given by the 2FDT in Eq. (2.2). The orientation,  $\mathbf{e}(t)$ , is governed by thermal rotational diffusion, such that,

$$\dot{\mathbf{e}}(t) = \mathbf{N}(t) \times \mathbf{e}(t). \quad (6.2)$$

Here,  $\mathbf{N}(t)$  is Gaussian white noise with a mean of 0 and a variance of:

$$\langle N_\alpha(t) N_\beta(t') \rangle = 2D_R \delta_{\alpha\beta} \delta(t - t'), \quad (6.3)$$

where  $D_R = \frac{3}{4} \frac{D_T}{R^2}$  for a particle of radius  $R$ . Eq. (6.3) is equivalent to the 2FDT in Eq. (2.2) except for the rotational degree of freedom.

These dynamical equations of motion lead to ABP behaviors which are distinct from those of a passive particle. In particular, ABPs have a finite persistence length,

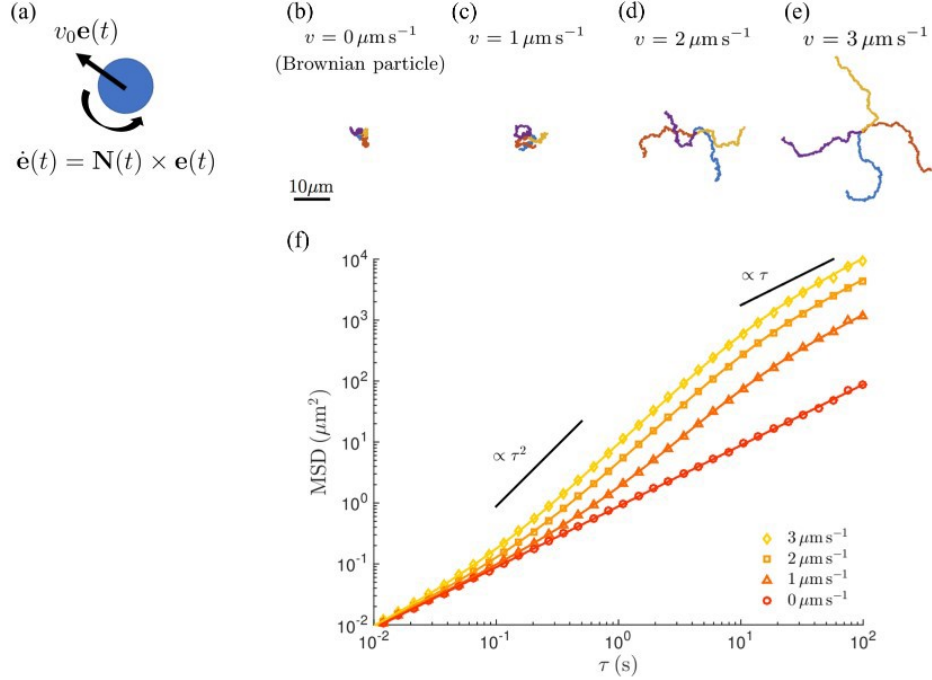


**Figure 6.1.:** Active Brownian particles. **a)** Schematic model of an active Brownian particle characterized by propulsion speed  $v_0$  and orientation  $\mathbf{e}(t)$ . Trajectories of active Brownian particles (in 2D) for propulsion velocities **b)**  $v_0 = 0 \mu\text{ms}^{-1}$  (passive Brownian particle), **c)**  $v_0 = 1 \mu\text{ms}^{-1}$ , **d)**  $v_0 = 2 \mu\text{ms}^{-1}$ , and **e)**  $v_0 = 3 \mu\text{ms}^{-1}$ . For each propulsion velocity, four different trajectories are shown, each in a different color. **f)** Mean square displacements of active Brownian particles (in 2D) with aforementioned propulsion speeds. Figs. **b-f)** are adapted from Ref. [68].

$l_p = v_0/D_R$ , during which they travel along their initial orientation before changing direction [68]. This persistence can be seen qualitatively by comparing the trajectory of a passive particle in Fig. 6.1b) to the trajectory of an ABP in Fig. 6.1e).

The mean square displacement (MSD) of an ABP is also distinct from that of a passive particle. Whereas an overdamped passive particle exhibits diffusive behavior ( $\text{MSD}(t) \propto t$ ) at all time scales, an ABP exhibits superdiffusive behavior ( $\text{MSD}(t) \propto t^\alpha$ , for  $\alpha > 1$ ) at intermediate time scales ( $t \approx 1/D_R$ ), as can be seen in Fig. 6.1(f). At long time scales, its motion once again becomes diffusive (Fig. 6.1(f)) [69]; however, its motion is characterized by the an enhanced diffusion coefficient,  $D_{\text{eff}} = D_T + v_0^2/D_R$  (in 2D).

## 6.2 Active Langevin particle model

Similarly to the ABP model, ALPs propel themselves with a constant force  $F_0$  subject to rotational diffusion with a diffusion constant  $D_R$  [59, 60, 61, 62, 63, 64, 65, 66]. The difference between the ABP and the ALP model is that ALPs are underdamped, i.e. they have inertia. Therefore, the equation of motion for an isolated ALP is:

$$m\dot{\mathbf{v}}(t) = F_0\mathbf{e}(t) - \gamma\mathbf{v}(t) + \boldsymbol{\xi}(t), \quad (6.4)$$

where  $F_0$  is the propulsion force of the ALP,  $\mathbf{e}(t)$  is its orientation, and  $\gamma = 6\pi\eta R$  is the damping constant for an ALP radius  $R$  in a thermal bath with viscosity  $\eta$ . The stochastic force on the ALPs,  $\boldsymbol{\xi}(t)$ , represents implicit collisions of the ALPs with thermal bath particles. These collisions can be represented as Gaussian white noise with a variance described by the 2FDT given in Eq. (2.2). From the damping constant,  $\gamma$ , we define the translational diffusion coefficient of an isolated ALP,  $D_T$ , as  $D_T = k_B T / \gamma$ . In Eq. (6.4), we have assumed that the damping force is Markovian.

The orientation of the ALP,  $\mathbf{e}(t)$ , is governed by rotational diffusion, such that,

$$J\ddot{\mathbf{e}}(t) = -\gamma_R\dot{\mathbf{e}}(t) + \mathbf{N}(t) \times \mathbf{e}(t), \quad (6.5)$$

where  $J$  is the moment of inertia of the ALP,  $\gamma_R = k_B T_R / D_R$  is its rotational damping constant for a rotational temperature of  $T_R$ , and  $\mathbf{N}(t)$  is Gaussian white noise with a mean of 0 and a variance given in Eq. (6.2).

The addition of both translational and rotational inertia to the equations of motion leads to characteristic rotational and translational inertial relaxation times for the ALPs ( $\tau_R = J/\gamma_R$  and  $\tau = m/\gamma$ , respectively). These characteristic inertial times are in addition to the persistence time  $\tau_p = 1/D_R$ , which characterizes the rotational relaxation of the random walk and is also present in the case of no rotational inertia. These additional time scales are exhibited in the MSD of an ALP: the MSD is ballistic at very short time scales due to its inertia, then it becomes diffusive due to fluctuations of the implicit solvent, then it once again becomes ballistic due to its self propulsion, and finally at very long times it becomes diffusive [59]. As is the case for an ABP, the long time diffusion coefficient of an ALP is enhanced from that of a passive particle.

Although Eqs. (6.4) and (6.5) describe the most general model of an ALP [59], in Parts II-IV, we follow Refs. [60, 62] and set the rotational inertia of ALPs to zero for

simplicity. Therefore, Eq. (6.5) simplifies to Eq. (6.2) and the two time scales which characterize the system are  $\tau$  and  $\tau_p$ .

## 6.3 Collective behavior

Collective motion occurs when the movement of a singular unit in a system is almost entirely determined by its interactions with other units. In other words, the behavior of an isolated unit significantly differs from that of its behavior in a group [55]. This type of phenomenon can occur in both passive and active systems; however, it has garnered particular attention in the field of active matter because of the emergence of motility-induced phase separation (MIPS).

Although passive Brownian particles (PBPs) can undergo liquid-vapor phase separation, this is only possible in systems in which the interactions between particles have an attractive component. In purely repulsive passive systems, it is impossible for liquid-vapor phase separation to occur. However, active systems can undergo phase separation even when the interactions are purely repulsive; a phenomenon known as MIPS, in which a high density and a dilute gas coexist in the same system [70, 71, 72, 64, 59, 73].

The two primary characteristics of active particles which drive MIPS are that active particles tend to cluster in areas where they move more slowly [74] and that the local propulsion speed depends on the local density [75]. Although these behaviors are not hard-coded into the behavior of the ABPs, they emerge due to collisions between the particles, which occur more frequently in high density regions.

The mechanism by which clusters form in active systems is shown in Figs. 6.2a-c). When two active particles collide (Fig. 6.2a)), they become stuck together (Fig. 6.2b)) for some finite time which is determined by their rotational diffusion. Only after this finite time, are they able to separate (Fig. 6.2c)). The clusters in MIPS are dynamic, as can be seen in Figs. 6.2e-h), which show the time evolution of MIPS clusters [68].

Although MIPS occurs in both ABPs [71, 72] and ALPs [64, 59, 73], the characteristics of MIPS in baths of ABPs and ALPs differ. In particular, MIPS is harder to achieve for ALPs because their translational inertia causes them to bounce off each other when they collide, rather than stick together [59]. In fact, above a certain critical reduced mass ( $M \equiv D_R m / \gamma \approx 0.08$ , which measures the impact of inertia), MIPS does not occur in baths of ALPs (see Fig. 6.3a)) [59]. Conversely, the

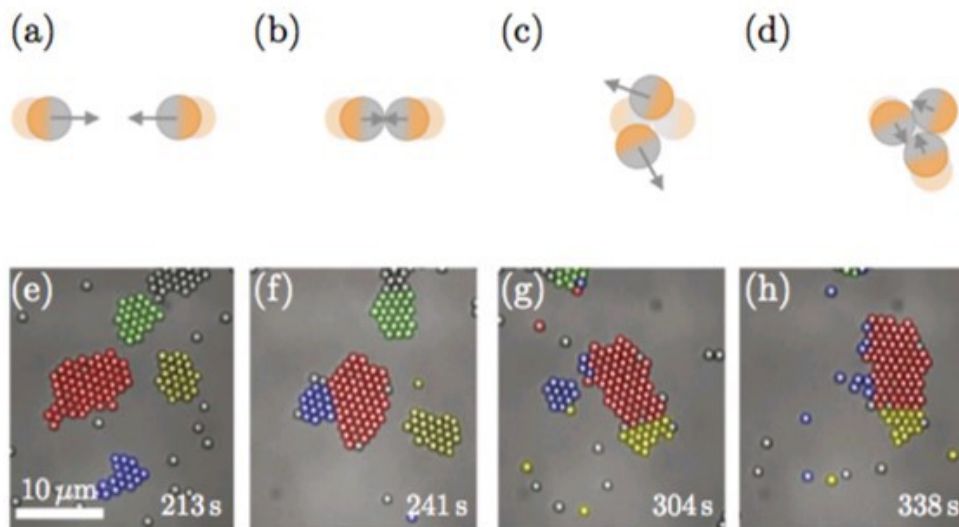


**Figure 6.2:** Clustering of active particles. **a-d)** Schematic diagram of how clusters form in groups of active particles: **a)** two active particles collide and, consequently, **b)** block each other, thereby forming a two particle cluster. **c)** After a finite amount of time (on the time scale of rotational diffusion), the particles are able to break free of each other. **d)** Depending on the properties of the active particles (density, speed, etc.), further particles can also join the cluster. **e-h)** Clusters formed in a homogeneous distribution of active particles with area fraction  $\phi = 0.14$  in Ref. [76]. The overlaid color of each particle shows to which cluster it belongs, thus highlighting the dynamic nature of the clusters. Figure adapted from Ref. [68].



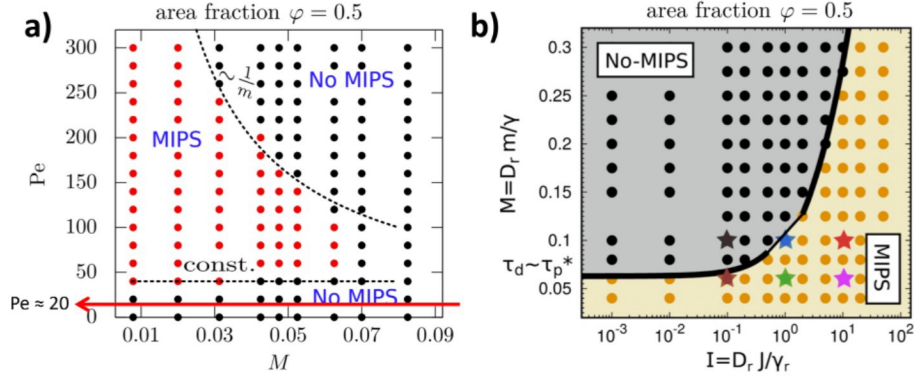


**Figure 6.3.:** Phase diagram of ALPs in 2D with packing area  $\phi = 0.5$ . **a)** Peclet number vs. reduced mass ( $M = D_R m / \gamma$ ), where the moment of inertia of the ALPs is  $J = 0.066\epsilon / D_R^2$ . Figure adapted from Ref. [64]. The red horizontal line with an arrow shows  $Pe \approx 20$ , the upper limit of the Peclet numbers used in Parts II-IV. **b)** Reduced mass vs. reduced moment of inertia ( $I = D_R J / \gamma r$ ), where the Peclet number is  $Pe = 50$ . In Parts II-IV,  $M \approx 0.03$ , there is no rotational inertia (i.e.  $J = I = 0$ ), and  $Pe \leq 20$ . Figure adapted from Ref. [73].

increase of rotational inertia in ALPs actually enhances the stability of MIPS (see Fig. 6.3b)) [73].

In Parts II-IV, our ALPs have a reduced mass of  $M \approx 0.03$ , below the critical reduced mass. However, we limit ourselves to ALPs with Peclet numbers  $Pe \equiv F_0 / (2D_R \gamma R) \leq 20$ , which is below the threshold necessary to induce MIPS in a system of ALPs (see Fig. 6.3a)). We note that Fig. 6.3a) was constructed from simulations of ALPs with rotational inertia, whereas we use overdamped rotational equations of motion in Parts II-IV. However, Ref. [64] found that the results presented in Fig. 6.3a) remained qualitatively the same for multiple values of rotational inertia, implying that the rotational dynamics are close to overdamped. We therefore infer that these results extend to systems with overdamped rotational dynamics.

The systems used to construct Fig. 6.3 are performed in 2D, whereas those presented in Parts II-IV are in 3D. To our knowledge, no phase diagrams have been constructed for ALPs in 3D. Based on the fact that, for ABPs, the Peclet number necessary for phase separation is significantly higher in 3D than in 2D [77], we infer that this will also be the case for ALPs. Consequently, we expect the low Peclet numbers studied in Parts II-IV are well below the threshold for MIPS.

## 6.4 Boundary interactions

Self-propelled particles tend to accumulate at boundaries [78, 79, 80, 81, 82, 83, 84, 85]. This accumulation is in part due to complex swimming dynamics of the active particles (e.g. cilia- and flagella-boundary interactions [85] or hydrodynamic interactions [79, 83]) as well as the geometric constraints of the boundary [80, 81]. However, the most simple explanation for this accumulation is the finite persistence time of active particles, which causes them to maintain their orientation for a finite time even after encountering an obstacle.

This persistent motion of active particles exerts a force perpendicular to the boundary, which accumulates over time and space to generate a ‘swim pressure,’ which represents the pressure exerted by the boundary in order to contain the active particle [86]. Although for free (i.e. no external forces acting on it) symmetric bodies the net force on the body will always be zero, free asymmetric bodies can experience a net force which leads to directed motion (see Section 6.5) [87, 88, 89].

## 6.5 Active-passive systems

In addition to studies of purely active systems, other studies have focused on systems with a mixture of passive and active elements. We focus on one such active-passive system: that of a passive probe immersed in an active bath. One of the first investigations of such a system was done by Wu and Libchaber, who put micron scale beads in a quasi-two-dimensional bath of bacteria [90]. In this setup, Wu and Libchaber found that the passive colloids immersed in the bacterial bath had MSDs with two distinct time scales. Whereas on the long time scale the passive colloid exhibited normal diffusive behavior, on the short time scale, it was superdiffusive (see Fig. 6.4), much like the different time scales exhibited by an ABP itself [69].

Since the experiments of Wu and Libchaber [90] reported this enhanced diffusion of a probe in a bacterial bath, a plethora of both experimental and theoretical studies have been published on the behavior of a probe in an active bath [28, 29, 31, 87, 88, 89, 91, 92, 93, 94, 95, 96, 97, 98, 99, 100, 101, 102]. A number of such studies have asserted that the dynamical behavior of a probe immersed in an active bath is analogous to that of an isolated active particle [28, 58, 68]. Other studies have derived equations for the net force exerted on bodies immersed in active baths, as well as the density profile surrounding such a body [88, 89]. Unlike analogous passive systems, active baths can generate a net force on immersed probe particles.

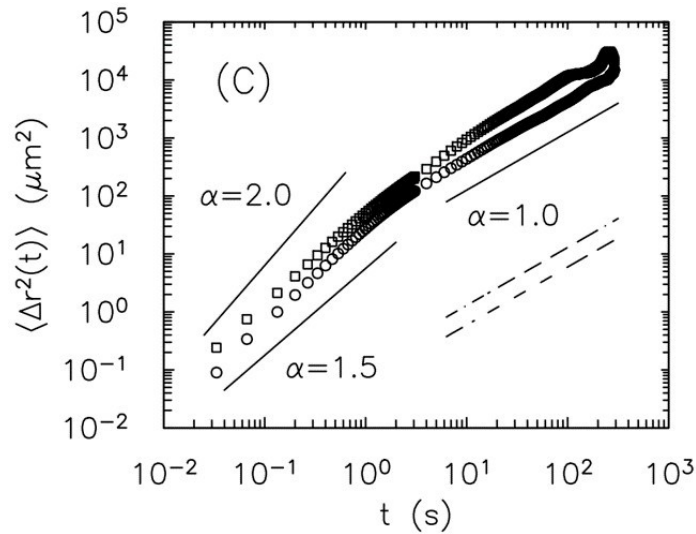


**Figure 6.4.:** Mean square displacement measurements of passive beads with diameters  $4.5\mu\text{m}$  (squares) and  $10\mu\text{m}$  (circles) immersed in a bath of motile bacteria. The dashed lines correspond to the thermal diffusion of  $4.5\mu\text{m}$  and  $10\mu\text{m}$  beads. Solid lines with slopes  $\alpha = 1.0, 1.5, 2.0$  are added for ease of visualization. Figure from Ref. [90].

However, as one would expect from symmetry, in the case that the probe is free (i.e. no external forces are acting on it), this is only possible for asymmetric probes (see the example in Fig. 6.5). The net force on a free, symmetric probe in an active bath remains zero, as it would in a passive bath. This ability to generate directed motion from an active bath has led researchers to investigate whether useful work can be extracted from active baths [103, 104, 105, 106].

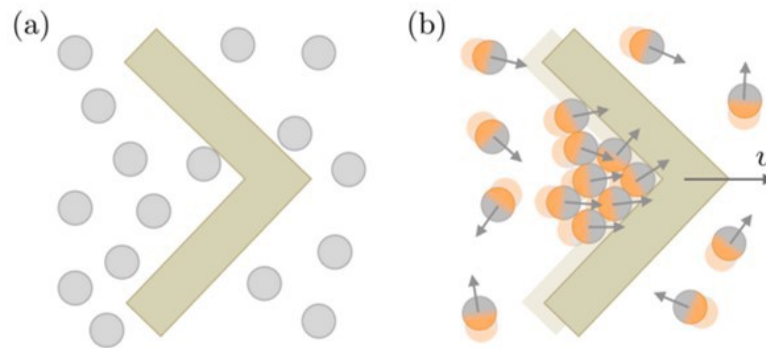


**Figure 6.5.:** Motion of an asymmetric wedge. **a)** In a passive bath, the wedge displays no directed motion, whereas **b)** in an active bath, the particles gather in the corner of the wedge, resulting in directed motion. Figure taken from Ref. [68].

## Simulation details

The simulation data discussed in this thesis have all been obtained using the molecular dynamics (MD) method [107, 108, 109, 110]. This method numerically solves Newton's equations of motion for both translational,

$$\dot{x}(t) = v(t) \quad \dot{v}(t) = \frac{1}{m}F(t), \quad (7.1)$$

and rotational,

$$\dot{\phi}(t) = \omega(t) \quad \dot{\omega}(t) = \frac{1}{J}\tau(t), \quad (7.2)$$

degrees of freedom and evolves them in time. In Eq. 7.1,  $x(t)$  is the position,  $v(t)$  the velocity, and  $m$  is the mass. The force field,  $F(t)$  is defined by the underlying microscopic model. In Eq. 7.2,  $\phi(t)$  is the orientation,  $\omega(t)$  is the angular velocity,  $\tau(t)$  is the net torque, and  $J$  is moment of inertia.

All simulations are performed using LAMMPS [111]. The length, energy, and mass scales in the system are defined by the Lennard-Jones (LJ) diameter  $\sigma$ , energy  $\epsilon$ , and mass  $m$ , respectively, which defines the LJ time scale  $t_{\text{LJ}} = \sigma\sqrt{m/\epsilon}$ . We use truncated and shifted LJ potentials with the energy scale  $\epsilon$  which are cut off at  $r_c = 2^{\frac{1}{6}}\sigma$ , resulting in purely repulsive interactions according to the Weeks-Chandler-Anderson (WCA) potential [112]:

$$U(r) = \begin{cases} 4\epsilon \left( \left(\frac{\sigma}{r}\right)^{12} - \left(\frac{\sigma}{r}\right)^6 \right) + \epsilon & r \leq 2^{\frac{1}{6}}\sigma \\ 0 & r > 2^{\frac{1}{6}}\sigma. \end{cases} \quad (7.3)$$

The simulation box has periodic boundary conditions in all three dimensions and a side length based on the desired density of the bath. The box is cubic in all cases except for simulations of the dragged colloid in Chapter 16, in which case the x-axis of the box is three times longer than that of the other axes.

The active bath consists of spherical ALPs with a mass of  $m_{\text{ALP}} = 1m$  and a radius of  $R = 0.5\sigma$ . The passive bath is modeled by ALPs with an active force  $F_0 = 0$ . The number of ALPs in the bath is determined by the desired density of the bath. In order to sample at our desired temperature,  $k_{\text{B}}T = 1\epsilon$ , we couple the ALP bath particles to a thermal bath using a Langevin thermostat. The parameters of the thermal bath

are chosen such that  $\eta = 1 m/(\sigma t_{LJ})$ , resulting in  $\gamma = 3\pi m/t_{LJ}$ ,  $D_T = (3\pi)^{-1}\sigma^2/t_{LJ}$ , and  $D_R = \pi^{-1}/t_{LJ}$ . The ALPs interact through the WCA potential (Eq. (7.3)) with both other bath particles and, in the case of all sections except Chapter 12, with the probe. Isolated ALP simulations are performed for a single ALP with the same properties ( $m_{ALP} = 1m$ ,  $R = 0.5\sigma$ ) as those of a bath ALP.

In Parts II and IV, the probe has a mass of  $M = 100m$  and is defined as a rigid body with a radius  $R_p = 3\sigma$ . In Part III, we vary the radius of the rigid probe while maintaining its mass to volume ratio. In all these sections (except Chapter 12), the body of the probe is constructed so that its surface is smooth, resulting in full slip boundary conditions for the LJ fluid. The probe interacts with the bath particles through the WCA potential of Eq. (7.3).

In Chapter 12, the probe is transparent and convective, so it does not interact with the ALPs through the WCA potential, but rather if ALPs  $j = 1 \dots N$  are contained in the volume  $\mathcal{V}$  of the probe, then the velocity of the probe is  $\mathbf{V} = \frac{1}{N} \sum_{j=1}^N \mathbf{v}_j$  and the squared velocity is  $\langle \mathbf{V}^2 \rangle = \frac{1}{N^2} \sum_{jk} \langle \mathbf{v}_j \mathbf{v}_k \rangle$ . We vary the radius of the transparent, convective probe to match the radii tested in Part III.

To test the 1FDT for the immersed passive particle in Section 9.4, we perform two simulations simultaneously: one in which a perturbation of force  $\alpha(t) = MV_0\delta(t)$  is applied to the immersed particle (pert) and one in which no perturbation is applied to the immersed particle (unpert). Aside from this perturbation, the simulations are identical; in particular, the same random numbers are used in the thermostat. We then calculate the response as  $\delta V(t) = V_{\text{pert}}(t) - V_{\text{unpert}}(t)$  and average this function over many systems to reduce statistical noise. This method is identical to that used in Refs. [33, 41, 113].

Throughout all the following sections, to simplify notation, we will use dimensionless quantities  $\hat{t} = t \gamma/m$ ,  $\hat{\mathbf{v}} = \mathbf{v} \sqrt{m/k_B T}$ ,  $\hat{F}_0 = F_0 \frac{1}{\gamma} \sqrt{m/k_B T}$ , and  $\hat{D}_R = D_R m/\gamma$ . Density values, the mass to volume ratio of the immersed passive probe, the spring constant of the harmonic potential, and all distances are given in LJ units. In these cases, the LJ units are explicitly written with the value. All values without explicitly written units are given in dimensionless units.

# Part II

---

Non-equilibrium signatures of a passive  
probe in an active bath

As we have discussed in Chapter 6, active systems exhibit vastly different behavior from passive systems. Furthermore, we have seen in Section 6.5 that when active and passive elements are mixed, the dynamics of the passive elements in the system are also significantly altered. In particular, we highlighted the system of a probe in an active bath, which has received growing attention since the experiments of Wu and Libchaber [90]. Nevertheless, in spite of an increasing volume of literature, a comprehensive understanding of this system is still lacking — especially regarding the question of how to use such a probe for measuring bath properties. As mentioned in Section 6.5, the net force on a free (i.e. no external forces acting on it) symmetric probe in an active bath remains zero [88, 89]. However, this begs the question: how can we tell that a free, symmetric probe in an active bath is out of equilibrium?

This problem is addressed in the present section. We consider a system of a passive probe particle immersed in a bath of ALPs. We limit ourselves to low Peclet numbers ( $Pe \leq 20$  where  $Pe = F_0/(2D_R\gamma R)$ ) where MIPS does not occur. Our central question is: What are non-equilibrium signatures in the motion of the passive probe in this active fluid?

As mentioned in Section 6.5, a number of previous studies have asserted that the dynamical behavior of a probe immersed in an active bath is analogous to that of an isolated active particle [28, 58, 68]. Therefore, we will also characterize the behavior of an isolated ALP, as a reference and to identify its characteristic non-equilibrium signatures.

The results presented in this part have been published in:

Passive probe particle in an active bath: can we tell it is out of equilibrium?

**J. Shea**, G. Jung, F. Schmid, *Soft Matter* **18**, 6965-6973 (2022).

## Isolated active Langevin particle

The equations of motion of an isolated ALP without rotational inertia (see Section 6.2) in dimensionless units read:

$$\begin{aligned}\frac{d}{dt}\hat{\mathbf{v}}(t) &= \hat{F}_0\mathbf{e}(t) - \hat{\mathbf{v}}(t) + \hat{\boldsymbol{\xi}}(t) \\ \frac{d}{dt}\mathbf{e}(t) &= \hat{\mathbf{N}}(t) \times \mathbf{e}(t)\end{aligned}\quad (8.1)$$

where  $\mathbf{e}(\hat{t})$  is a unit vector and the stochastic contributions  $\hat{\boldsymbol{\xi}}$  and  $\hat{\mathbf{N}}$  satisfy fluctuation-dissipation relations  $\langle \hat{\boldsymbol{\xi}}(\hat{t})\hat{\boldsymbol{\xi}}(\hat{t}') \rangle = 2\mathbf{1}\delta(\hat{t}-\hat{t}')$  and  $\langle \hat{\mathbf{N}}(\hat{t})\hat{\mathbf{N}}(\hat{t}') \rangle = 2\hat{D}_R\mathbf{1}\delta(\hat{t}-\hat{t}')$ . From these equations, we can analytically calculate the VACF  $C_{\hat{\mathbf{v}}}(\hat{t}) = \langle \hat{\mathbf{v}}(\hat{t}') \cdot \hat{\mathbf{v}}(\hat{t}' + \hat{t}) \rangle$  of isolated ALPs (see Appendix A):

$$\langle \hat{\mathbf{v}}(\hat{t})\hat{\mathbf{v}}(\hat{t}') \rangle = 3e^{-|\hat{t}-\hat{t}'|} + \frac{\hat{F}_0^2}{1-4\hat{D}_R^2} \left( e^{-2\hat{D}_R|\hat{t}-\hat{t}'|} - 2\hat{D}_R e^{-|\hat{t}-\hat{t}'|} \right). \quad (8.2)$$

The corresponding memory kernel  $K(t)$  which solves the Volterra equation:

$$\frac{d}{dt}\langle \hat{\mathbf{v}}(0)\hat{\mathbf{v}}(\hat{t}) \rangle = -\int_0^{\hat{t}} ds K(t-s)\langle \hat{\mathbf{v}}(0)\hat{\mathbf{v}}(s) \rangle, \quad (8.3)$$

can be calculated by Fourier methods, giving

$$K_{\text{ALP}}(\hat{t}) = \frac{6}{\langle \hat{\mathbf{v}}^2 \rangle} \left( \delta(\hat{t}) - \frac{\tau-1}{6\tau} \frac{\hat{F}_0^2}{1+2\hat{D}_R} e^{-t/\tau} \right), \quad (8.4)$$

with  $\tau = \langle \hat{\mathbf{v}}^2 \rangle / (\hat{F}_0^2 + 6\hat{D}_R)$ . To verify this result, one can simply insert (8.4) and (8.2) into Eq. (8.3).

From Eq. (8.2), we can then find the mean squared velocity of an ALP by taking  $t = t'$ :

$$\langle \hat{\mathbf{v}}^2 \rangle = 3 + \frac{\hat{F}_0^2}{1+2\hat{D}_R}. \quad (8.5)$$

The kinetic temperature of a passive particle in equilibrium is directly proportional to the mean-squared velocity (initial value of the velocity autocorrelation function)



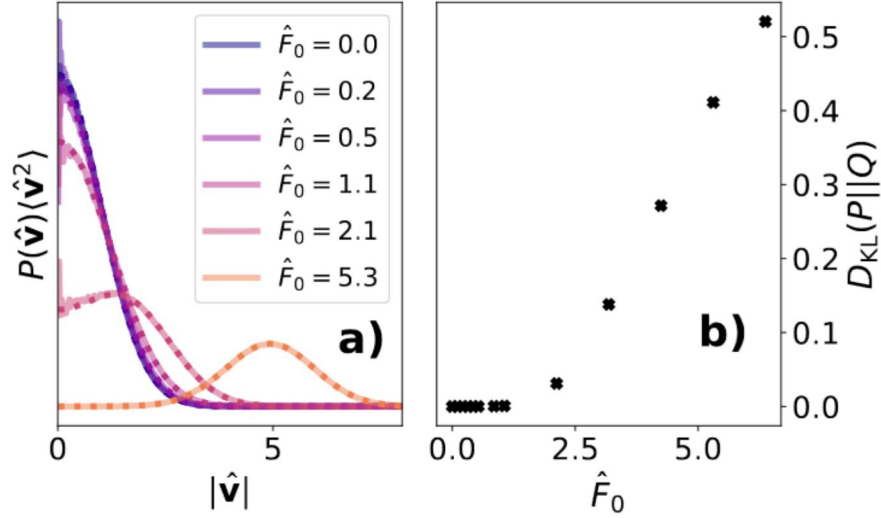


**Figure 8.1.:** **a)** Velocity distribution of isolated ALPs for different driving forces  $\hat{F}_0$  as indicated. Solid lines show simulation data, dashed lines the prediction of Eq. (8.8). The curves have been rescaled by  $\langle \hat{v}^2 \rangle$  for better visibility. **b)** Relative entropy (Eq. (8.9)) between the distributions in **a)** and a Gaussian distribution with same standard deviation as a function of  $\hat{F}_0$ .

through the equation  $\langle \mathbf{v}^2(t) \rangle = dk_{\text{B}}T/m$ , where  $d$  is the number of dimensions in the system [9]. From this equation, we define the kinetic temperature of an ALP as  $k_{\text{B}}T_{\text{eff}} = m\langle \mathbf{v}^2(t) \rangle/d$ . Unlike a passive particle, however,  $T_{\text{eff}}$  of an ALP will not necessarily be equal to the temperature of the thermal bath,  $T$ . In fact, from Eq. (8.5), we find that it is given by:

$$\frac{k_{\text{B}}T_{\text{eff}}}{k_{\text{B}}T} = 1 + \frac{1}{3} \frac{\hat{F}_0^2}{(1 + 2\hat{D}_R)}. \quad (8.6)$$

Therefore, we expect  $(k_{\text{B}}T_{\text{eff}} - k_{\text{B}}T) \propto \hat{F}_0^2$ . This scaling relation is analogous to that between the effective diffusion constant of an ABP and its active velocity [68].

The failure of an ALP to equilibrate to the same temperature as its thermal bath is a hallmark non-equilibrium signature; however, knowledge of the ALP thermostat is required to observe this enhanced temperature.

We also examine the velocity distribution,  $P(\hat{\mathbf{v}})$ , of an ALP, a description of which can be found in Appendix B.1. From simulation data, we observe that as  $\hat{F}_0$  of an ALP increases, its velocity distribution becomes increasingly non-Gaussian, as shown in Fig. 8.1a). This can also be inferred from the Fokker-Planck equation corresponding to Eqs. (8.1), which predicts a stationary velocity distribution:

$$P(\hat{\mathbf{v}}) = \mathcal{N} e^{-\hat{\mathbf{v}}^2/2} \exp(\hat{F}_0 U(|\hat{\mathbf{v}}|)), \quad (8.7)$$

in the limit  $\hat{D}_R \rightarrow 0$  (see Appendix B.2), where  $U'(|\hat{\mathbf{v}}|) = \langle \cos \angle(\hat{\mathbf{v}}, \mathbf{e}) \rangle_{\hat{\mathbf{v}}}$  is the mean cosine of the angle between  $\hat{\mathbf{v}}$  and  $\mathbf{e}$  for given ALP velocity  $\hat{\mathbf{v}}$ . The first factor ( $e^{-\hat{\mathbf{v}}^2/2}$ ) represents a Maxwell distribution at temperature  $k_B T$ . The second factor ( $\exp(\hat{F}_0 U(|\hat{\mathbf{v}}|))$ ) represents the effect of the propelling force. In the limit  $\hat{D}_R \rightarrow 0$ , the ALPs rotate infinitely slowly, and  $U(|\hat{\mathbf{v}}|)$  can be evaluated as  $U(|\hat{\mathbf{v}}|) = \frac{1}{\hat{F}_0} \ln(\sinh(\hat{F}_0 \hat{\mathbf{v}})/\hat{F}_0 \hat{\mathbf{v}})$ . Motivated by this result, we conjecture that  $P(\hat{\mathbf{v}})$  can, in general, be approximated by the expression:

$$P(\hat{\mathbf{v}}) \approx \mathcal{N} e^{-\hat{\mathbf{v}}^2/2} \frac{\sqrt{1 + 2\hat{D}_R}}{\hat{F}_0 |\hat{\mathbf{v}}|} \sinh\left(\frac{\hat{F}_0 |\hat{\mathbf{v}}|}{\sqrt{1 + 2\hat{D}_R}}\right), \quad (8.8)$$

which reproduces the correct limits  $\hat{D}_R \rightarrow 0$  and  $\hat{F}_0 \rightarrow 0$  and the correct kinetic temperature (Eq. (8.6)). Fig. 8.1a) shows that the simulation data (solid lines) are very well captured by this ansatz (dashed line).

The non-Gaussianity of the velocity distribution is another signature of the non-equilibrium nature of an isolated ALP, and one which can be extracted from the ALP trajectory alone. To better quantify this deviation from a Gaussian distribution, we calculate the relative entropy (Kullback-Leibler divergence) between the velocity distribution of an isolated ALP, as calculated from simulation data, and a zero-centered Gaussian distribution whose standard deviation corresponds to the theoretical kinetic temperature given in Eq. (8.6). The relative entropy between these two distributions is defined as:

$$D_{\text{KL}}(\mathcal{P}(\hat{\mathbf{v}}) || \mathcal{Q}(\hat{\mathbf{v}})) = \int_{\infty} d^3 \hat{\mathbf{v}} \mathcal{P}(\hat{\mathbf{v}}) \ln\left(\frac{\mathcal{P}(\hat{\mathbf{v}})}{\mathcal{Q}(\hat{\mathbf{v}})}\right), \quad (8.9)$$

where  $\mathcal{P}(\hat{\mathbf{v}})$  is the velocity distribution from simulation data and  $\mathcal{Q}(\hat{\mathbf{v}})$  is the reference Gaussian distribution. This relative entropy is graphed for an isolated ALP as a function of  $\hat{F}_0$  in Fig. 8.1b). We find that the velocity distribution of an ALP remains approximately Gaussian until an active force of  $\hat{F}_0 \sim 1$ , at which point it becomes increasingly non-Gaussian. This value of  $\hat{F}_0 = 1$  is the point at which the thermal forces are approximately equal to the ‘‘pulling’’ forces; after this point, ‘‘pulling’’ dominates.

## Probe in an active Langevin particle bath

We now consider a three dimensional system of a passive probe immersed in a bath of ALPs (see Fig. 9.1). The ALPs behave as described in Section 6.2, except they now additionally interact with each other and with the immersed probe via repulsive hard core interactions of the WCA type [112]. Consequently, the equation of motion for an interacting ALP,  $n$ , in our bath is:

$$m\dot{\mathbf{v}}_n(t) = F_0\mathbf{e}_n(t) - \gamma\mathbf{v}_n(t) + \boldsymbol{\xi}_n(t) - \nabla U_{\text{WCA}}(\mathbf{r}_n - \mathbf{R}) - \sum_{n \neq m} \nabla U_{\text{WCA}}(\mathbf{r}_n - \mathbf{r}_m), \quad (9.1)$$

where the terms are as defined in Section 6.2. The two final, additional terms describe WCA interactions with the probe and with all other ALPs, respectively.

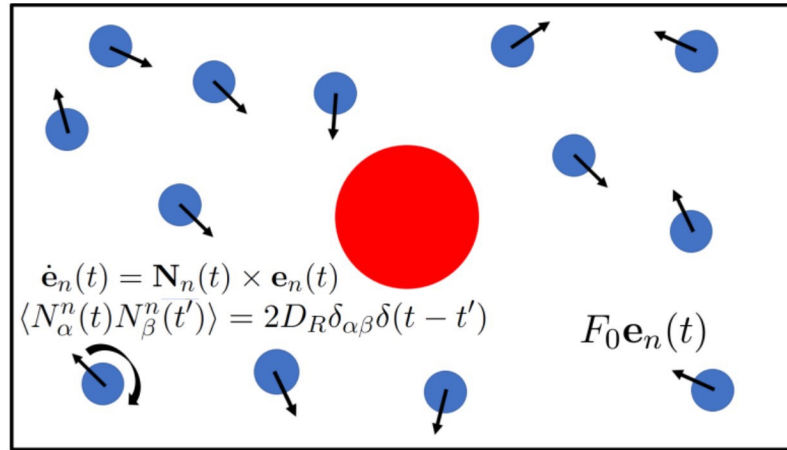


**Figure 9.1.:** System of a passive probe immersed in a bath of active Langevin particles.

The immersed probe only experiences forces from interactions with the surrounding ALPs. Unlike the ALPs, the probe is not coupled to the thermal bath; therefore, its equations of motion do not include stochastic or dissipative terms due to coupling with the thermal bath. Thus, our equation of motion for the probe is:

$$M\dot{\mathbf{V}}(t) = - \sum_n \nabla U_{\text{WCA}}(\mathbf{R} - \mathbf{r}_n), \quad (9.2)$$

where  $M$  is the mass of the probe,  $\mathbf{V}(t)$  is its velocity, and  $U_{\text{WCA}}(\mathbf{R} - \mathbf{r}_n)$  is the WCA potential due to an ALP particle,  $n$ , at position  $\mathbf{r}_n$ .

## 9.1 Velocity distributions and autocorrelation functions

Similar to isolated ALPs, bath ALPs exhibit the non-equilibrium signature of a non-Gaussian velocity distribution for  $\hat{F}_0 \gtrsim 1$ . This is apparent from Fig. 9.2a), which compares their velocity distribution from simulation data to a Gaussian distribution with the same standard deviation, and in Fig. 9.2b), which shows the relative entropy between these two curves. The velocity distribution of the immersed passive particle, on the other hand, remains Gaussian at all values of  $\hat{F}_0$ , independent of both the activity of the bath ALPs and their density (see Figs. 9.2d) and e)). Thus, in contrast to the case for both isolated and bath ALPs, the velocity distribution of the probe particle does not reveal the non-equilibrium nature of the system.

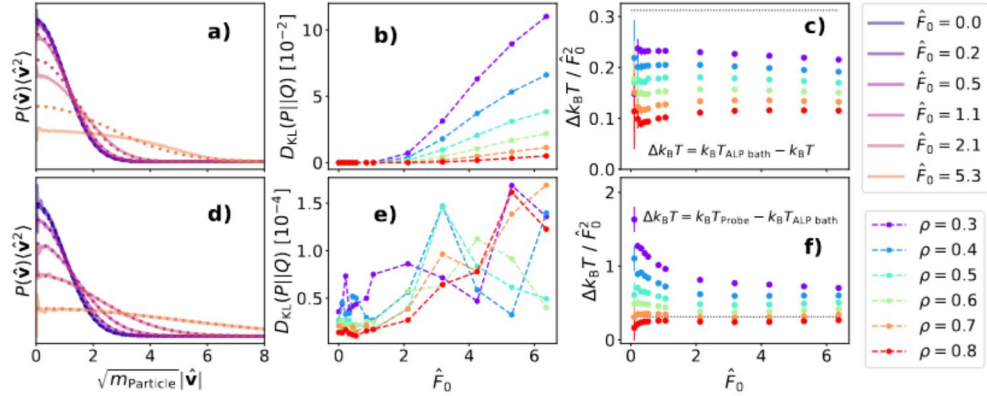


**Figure 9.2.:** **a,d)** Velocity distribution for **a)** bath ALPs and **d)** the immersed probe from simulation data (solid lines) at  $\rho = 0.4\sigma^{-3}$  for different driving forces  $\hat{F}_0$ , as indicated. The dotted lines show Gaussian distributions with the same standard deviation for comparison. The x-axis has been rescaled by  $\sqrt{m_{\text{Particle}}}$  for better visibility, where **a)**  $\sqrt{m_{\text{Particle}}} = \sqrt{m}$  and **d)**  $\sqrt{m_{\text{Particle}}} = \sqrt{M}$ . **b,e)** Corresponding relative entropies (Eq. (8.9)) between the simulation data and Gaussians with the same standard deviation. **c,f)** Kinetic temperature difference scaled by  $\hat{F}_0^2$  between **c)** a bath ALP and the thermal bath, and **f)** the probe and the ALP fluid. The dotted black line shows the difference between the kinetic temperature of an isolated ALP and its thermal bath. Densities in the legend are expressed in LJ units of  $\sigma^{-3}$ .

The immersed probe does, however, still exhibit the non-equilibrium signature of an enhanced kinetic temperature. In fact, for an ALP bath with a given  $\hat{F}_0$ , we find that the kinetic temperature of the immersed probe is even *higher* than that of the ALP bath (Fig. 9.2f)), which is already enhanced from that of an equilibrium bath

(Fig. 9.2c)). Thus, this system has a twofold lack of thermalization: firstly, between the ALP bath and the thermal bath, and secondly, between the probe and the ALP bath. Remarkably, we find these effects persist even when the probe is thermostatted, although the difference is less pronounced (see Fig. 9.3). The fact that the probe does not equilibrate to the same kinetic temperature as the ALP bath clearly reveals the non-equilibrium nature of the system; however, it requires analysis of both bath and probe. To uncover non-equilibrium signatures by solely observing the probe, we further investigate its dynamic properties.

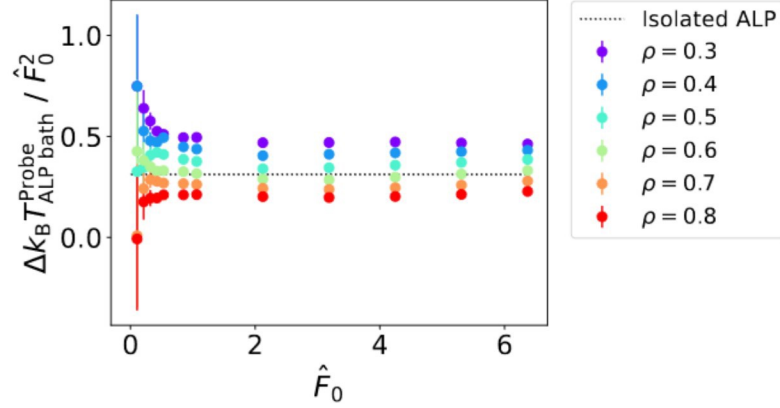


**Figure 9.3.:** Difference between the kinetic temperature of a thermostatted, immersed passive particle and that of the active bath ( $\Delta k_B T_{\text{ALP Bath}}^{\text{Probe}}$ ) divided by  $\hat{F}_0^2$ , as a function of  $\hat{F}_0$ . The dotted black line represents the kinetic temperature of an isolated ALP. Densities in the legend are expressed in LJ units of  $\sigma^{-3}$ .

We first focus on the VACF, which we determined analytically for an isolated ALP in Eq. (8.2). As is the case for the VACF of an isolated ALP (assuming  $\gamma/m > 2D_R$ ), in the limit  $t \rightarrow \infty$ , the VACF of a bath ALP decays exponentially as  $2\hat{D}_R$ , independent of density, as is shown in Fig. 9.4a). However, both for the bath ALPs and the probe, this exponential decay is only observed at sufficiently high values of  $\hat{F}_0$ , as is shown for the probe in Fig. 9.4c).

Despite the significant size difference between an ALP and the probe, the VACF of the probe decays exponentially at a very similar rate to that of an isolated ALP, as shown in Fig. 9.4b). Thus, the probe acquires some properties of the ALPs in the surrounding bath. However, unlike the VACF of bath ALPs, the VACF of the probe in the long-time limit depends on the density of bath ALPs.

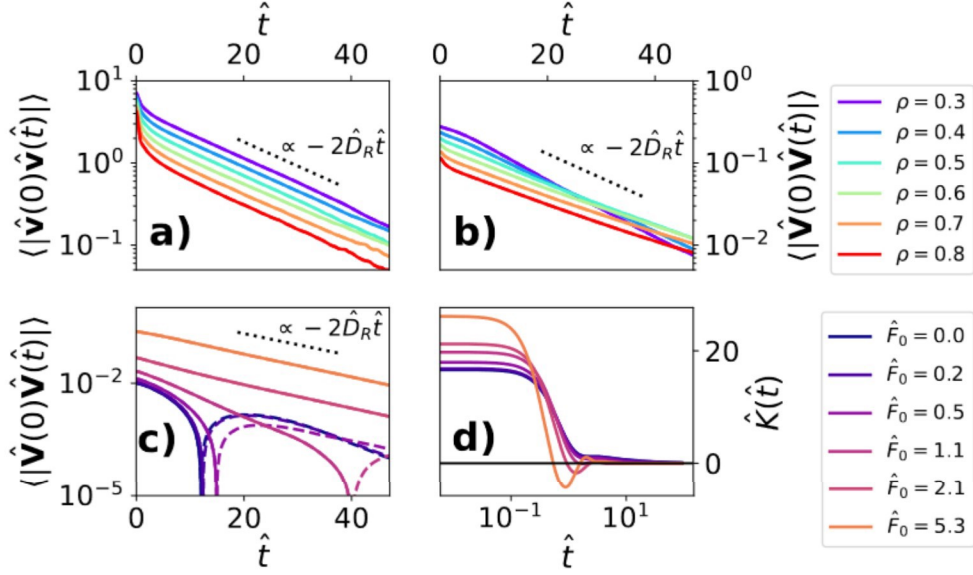


**Figure 9.4.:** VACF and memory kernel. **a,b)** Semi-logarithmic plot of the VACF for different densities with  $\hat{F}_0 = 5.3$  of **a)** a bath ALP, **b)** the immersed probe. **c)** Semi-logarithmic plot of the VACF for the immersed probe in a bath of density  $\rho = 0.4\sigma^{-3}$  for different values of  $\hat{F}_0$ . Dashed lines show the absolute value of the VACF. **d)** Semi-logarithmic plot of the memory kernel of the immersed passive particle in a bath of  $\rho = 0.4\sigma^{-3}$  for different values of  $\hat{F}_0$ . Densities in the legend are expressed in LJ units of  $\sigma^{-3}$ .

## 9.2 Non-Markovian behavior of the probe

Although the behavior of the VACF of a probe in an active bath differs from that of a probe in a passive bath, these differences are not inherent to non-equilibrium. Thus, to continue searching the dynamic behavior of the probe for non-equilibrium signatures, we map its movement onto the GLE given in Eq. (2.13). In mapping the motion of the probe to the GLE, we explicitly allow that the effective dynamics of the colloid in the ALP fluid may be non-Markovian. The memory kernel,  $K(t)$ , is determined from the VACF by Volterra inversion, as described in Sec. 2.1.1. We emphasize that the GLE is a coarse-grained model equation; the true dynamical equation of motion for the probe in the explicit active fluid is given in Eq. (9.2).

As shown in Fig. 9.4d), the shape of the memory kernel changes qualitatively with increasing activity level of the ALP fluid. It becomes non-monotonous and negative at intermediate times, indicating transient positive feedback that promotes superdiffusive behavior. This is also observed in the memory kernel of isolated ALPs (Eq. (8.4)). We conclude that the dynamics of the probe particle does acquire some properties of ALPs, as claimed in Refs. [28, 58, 68, 90]. However, memory kernels

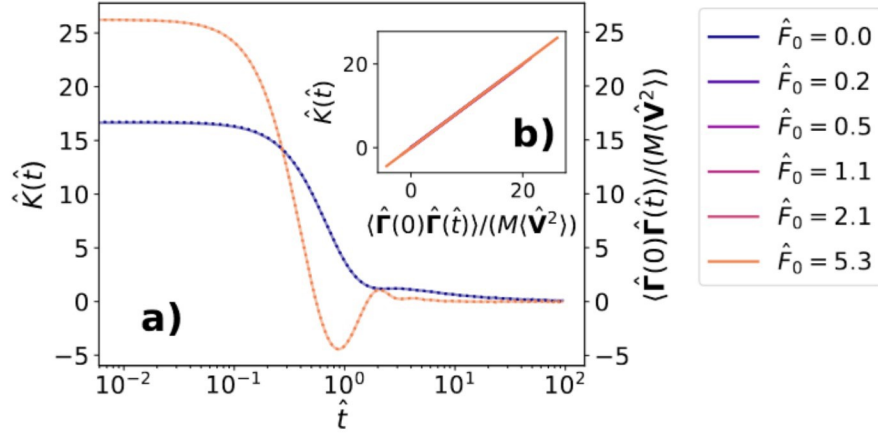


**Figure 9.5.:** Test of the 2FDT for the immersed passive particle in a bath with density  $\rho = 0.4\sigma^{-3}$ . **a)** Memory kernel (solid line) and the stochastic force autocorrelation function (dashed line) as a function of time for values of  $\hat{F}_0 = 0$  and  $\hat{F}_0 = 5.3$ . The prefactor of the memory kernel has been factored out. **b)** The stochastic force autocorrelation function as a function of the memory kernel (prefactor removed) for various  $\hat{F}_0$ .

may also oscillate in equilibrium systems [23, 24, 114], hence this cannot be used to diagnose non-equilibrium.

In Section 2.2, we showed that the dissipative interactions, described by the memory kernel, can be related to the stochastic forces through the 2FDT (see Eq. (2.21)) [9, 33]. Several studies of a passive probe immersed in an active bath have concluded that the non-equilibrium nature of the bath leads to a violation of the 2FDT for the immersed probe [26, 27, 28, 29, 30, 31], which has been touted as a signature of the non-equilibrium nature of this system. In seeming contradiction, Loi et al. [32] found that the 2FDT for the correlation function of the independent scattering function is fulfilled for a passive probe in an active bath. This apparent contradiction is due to a difference in definition of the stochastic and dissipative forces on the probe. In fact, as stated in Section 2.2, Ref. [33] has shown that whenever the stochastic and dissipative forces on the probe are defined according to the Mori-Zwanzig projection operators [9, 10, 11, 13], then the 2FDT will be fulfilled exactly, even if the system is out of equilibrium. Therefore, violation of the 2FDT is not an inherent trait of the non-equilibrium nature of the bath, but rather a matter of definition. Indeed, in accordance with the results of Loi et al. [32] and Ref. [33], we find that the 2FDT for the GLE is fulfilled exactly for the immersed probe for all driving forces  $\hat{F}_0$  (see Fig. 9.5).

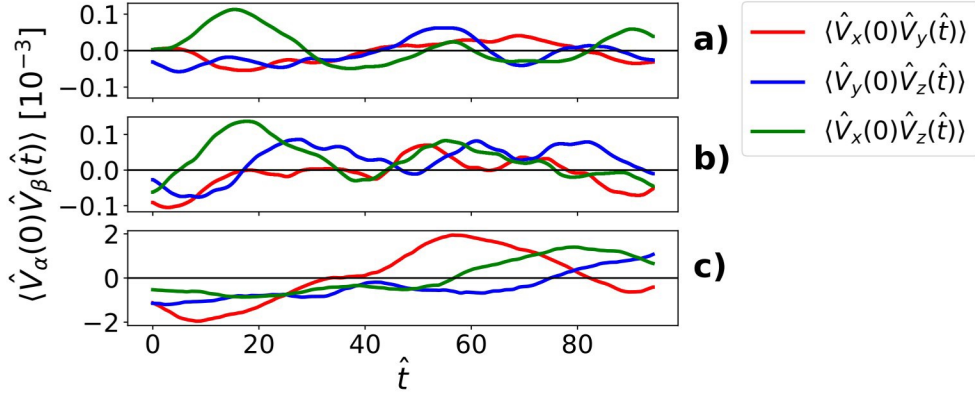


**Figure 9.6.:** Velocity cross correlation functions of the probe particle in a fluid of density  $\rho = 0.4\sigma^{-3}$  for activities **a)**  $\hat{F}_0 = 0$ , **b)**  $\hat{F}_0 = 1.1$ , **c)** and  $\hat{F}_0 = 5.3$ . For all values of  $\hat{F}_0$ , the cross correlations are approximately zero and are orders of magnitude less than the probe VACFs in Figs. 9.4b) and c).

### 9.3 Entropy production

Among other non-equilibrium signatures proposed in the literature [115, 116, 117, 118, 119], one of the most ubiquitous is entropy production associated with a difference of probabilities between forward and time-reversed trajectories, which has been found in a number of active systems including that of an isolated active Langevin particle [62] and that of many interacting active Brownian particles undergoing MIPS [120]. In particular, Ref. [121] found evidence for entropy production through time reversal symmetry breaking in a model used to represent a passive probe immersed in an active bath. However, their model implicitly represents probe interactions with active bath particles through Gaussian colored noise rather than through explicit microscopic processes.

As a means of investigating the possibility of entropy production through the breaking of time reversal symmetry, we examine the stochastic force on the probe as well as the velocity cross-correlation functions of the probe. We find that the velocity cross-correlation functions of the probe are zero, even in the presence of an active bath, as is shown in Fig. 9.6. Thus, we do not see any signatures of time reversal symmetry breaking in the velocity of the probe.

From Eq. (2.19), we calculate the stochastic force on the probe particle directly from our simulation data [17]. We find that, in spite of the non-equilibrium nature of the bath, the stochastic force distribution on the probe remains Gaussian, as is shown in Fig. 9.7. Although we do see some deviations from a Gaussian stochastic force distribution at low densities (see Fig. 9.7a) and Appendix C), these deviations seem



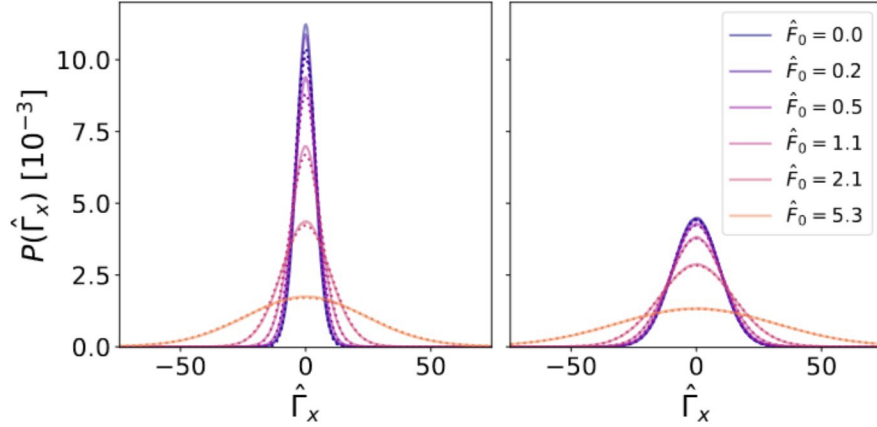


**Figure 9.7.:** Stochastic force distribution on the probe particle immersed in a fluid of ALPs with density **a)**  $\rho = 0.4\sigma^{-3}$  and **b)**  $\rho = 0.8\sigma^{-3}$ . The solid lines show simulation data, whereas the dotted lines show zero-centered Gaussian distributions with the same standard deviation.

to be due to low density effects rather than to the bath activity. In fact, as the activity of the bath increases, the deviations from a Gaussian distribution at low densities actually decrease. Therefore, the stochastic force on the probe also does not reveal any signs of time reversal symmetry breaking. Thus, we, in fact, found no evidence of such a breaking of time reversal symmetry in our probe trajectories.

Evidence of entropy production has also been found for a probe immersed in an active bath without relying on time reversal symmetry breaking [122]. However, this method relies on explicit knowledge of the active bath particle dynamics and, consequently, does not provide a non-equilibrium signature which can be determined solely from knowledge of the probe.

## 9.4 Response to small perturbations

In equilibrium systems, the response of quantities to infinitesimal external perturbations can be described by linear response theory (see Chapter 4). As a last test of non-equilibrium signatures in our active system, we investigate whether the predictions of linear response theory still hold here. Specifically, we investigate the 1FDT, which is described in Chapter 4.

To test the validity of the 1FDT for the immersed passive particle, we apply a perturbation by kicking it slightly at time  $t = 0$ , i.e., we add an instantaneous force of the form  $\alpha(t) = MV_0\delta(t)$ , where  $M$  is the immersed particle mass and  $V_0$  is small.

We then investigate the response of the velocity [33, 113]. For our specific system, in the equilibrium case, the 1FDT (see Eq. (4.12) for the general case) would be given by:

$$\frac{\delta\langle V(t) \rangle}{V_0} = \frac{C_V^{SS}(t)}{C_V^{SS}(0)}, \quad (9.3)$$

where  $C_V^{SS}(t)$  is the steady state (equilibrium) VACF. The question is whether this relation still holds if the system is perturbed from a non-equilibrium steady state, such as our active system.

To test the relation for the immersed passive particle, we perform two simulations simultaneously: one in which the perturbation  $\alpha(t) = MV_0\delta(t)$  is applied to the immersed particle (pert) and one in which no perturbation is applied to the immersed particle (unpert). Aside from this perturbation, the simulations are identical; in particular, the same random numbers are used in the thermostat. We then calculate the response as  $\delta V(t) = V_{\text{pert}}(t) - V_{\text{unpert}}(t)$  and average this function over many systems to reduce statistical noise. This method is identical to that used in Ref. [33, 41, 113]. To ensure that we are within the regime where the response is linear in  $V_0$ , we test multiple values of  $V_0$  ( $V_0 = 0.2, 0.4, 0.5$ ; see Appendix D) and verify that the response function is the same for all values.

The results for  $\delta\langle \hat{V}(t) \rangle / \hat{V}_0$  are summarized in Fig. 9.8 and plotted versus  $C_V^{SS}(t) / C_V^{SS}(0)$ . If Eq. (9.3) holds, the data in such a plot should all collapse onto one diagonal line. Fig. 9.8 shows that this is indeed the case at driving force  $\hat{F}_0 = 0$  (an equilibrium bath), but deviations are observed already at low values of  $\hat{F}_0$ . As the value of  $\hat{F}_0$  increases, thereby driving the system further out of equilibrium, the violation of the 1FDT becomes increasingly large. Thus, even though the immersed passive particle reaches a nonequilibrium steady state, the 1FDT is *not* fulfilled for a passive particle immersed in an active bath. This effect can be used to detect non-equilibrium even if one has only access to the observation of a single probe particle.

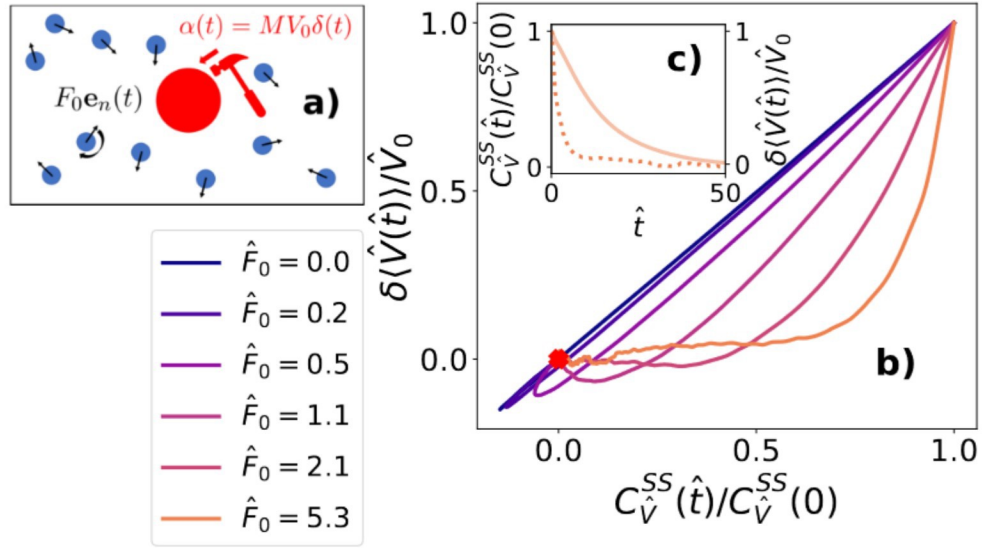


**Figure 9.8.:** Test of the 1FDT for the immersed passive particle in a bath with density  $\rho = 0.4\sigma^{-3}$  for perturbation force  $\alpha(t) = MV_0\delta(t)$  with  $V_0 = 0.5$ . **a)** Schematic diagram of the perturbation applied to the probe. **b)** Response function of the probe velocity versus normalized VACF. The red diamond shows the point (0,0) to which both the functions decay in the long-time limit. If the 1FDT is fulfilled, the curve is a straight line along the diagonal. **c)** Response function of the probe velocity (dotted line) and normalized VACF (solid line) as a function of time for  $\hat{F}_0 = 5.3$ .

## Part II: conclusions and outlook

We have shown that non-equilibrium signatures of a passive particle in an active bath are not as readily available as those of an active particle itself. Although the immersed probe does inherit some properties of the active bath, such as slowly decaying velocity correlations and a partially negative memory kernel, unlike an active bath particle, it does not inherit a non-Gaussian linear velocity distribution. The probe acquires an enhanced kinetic temperature, as does the active bath, but these two temperatures are not equal: the temperature of the immersed probe is even higher than that of the active bath. Therefore, the lack of thermalization in this system is twofold. The failure of the probe to equilibrate to the same temperature as the active bath is one non-equilibrium signature of the system; however, detecting this enhanced temperature requires knowledge of the bath itself. As one way to detect a non-equilibrium signature from only the trajectory of the probe, we propose to slightly perturb the probe. If the bath is not at equilibrium, this will then be revealed through a violation of the first fluctuation dissipation theorem.

In the current work, we have considered active particles with inertia (ALPs), because this allowed us to study velocity-related quantities such as the kinetic temperature and velocity autocorrelation function. Literature studies have often focused on the overdamped limit of active Brownian particles (ABPs) with mass  $m \rightarrow 0$  [28, 71, 72, 87, 89, 88, 98]. We expect that our main results will still persist in that limit, especially given that important fundamental properties of the fluid, such as the quadratic scaling of the effective temperature (or effective diffusion constant in the case of an ABP) and the velocity correlations (see Fig. 9.4a)) are also valid for ABPs. On the other hand, our active particles were coupled to a Langevin thermostat, implying that we do not take into account the possibility of hydrodynamic flows in the implicit solvent. This corresponds to a situation where hydrodynamic interactions are effectively screened, e.g., due to the presence of static obstacles. We should note that even in free solution, active swimmers have reduced hydrodynamic interactions, because they do not act as hydrodynamic monopoles, but as dipoles. Nevertheless, recent experiments found interesting heterogeneous jump-diffusion processes in the

dynamics of tracer particles interacting hydrodynamically with an active fluid [123], which possibly carries additional unambiguous signatures of nonequilibrium.

# Part III

---

Boundary interactions of active matter with  
an immersed passive probe

In Section 6.4, we saw that self-propelled bodies tend to accumulate at boundaries [78, 79, 80, 81, 82, 83, 84], generating a force on said boundary [88, 89]. For asymmetric bodies, this force can lead to directed motion (see Section 6.5), in contrast to free symmetric bodies, on which the net force remains zero [88, 89]. However, even though free symmetric bodies do not experience a net force when in contact with active particles, they do still experience accumulations of active particles at their surfaces.

In Part II, we found that a symmetric probe immersed in an active bath adopts many attributes of active particles themselves, as previously claimed in Refs. [28, 58, 68, 90]. Specifically, we found: the kinetic temperature of the probe scales quadratically with  $\hat{F}_0$ , as it does for an active particle (Section 9.1); in the long time limit, the VACF of the probe decays with the same rate as that of an active particle, in spite of a significant difference in size (Section 9.1); and the memory kernel of the probe becomes negative at intermediate times, as is the case for that of an active particle (Section 9.2).

Yet it remains unclear what mechanism leads the probe to acquire these attributes of an active particle. In particular, it is unclear as to how the properties of the probe vs. the properties of the active bath influence the probe dynamics. In this section, we examine the properties of the active bath as well as how the active bath interacts with the immersed probe at its boundary in order to ascertain this mechanism.

To determine the mechanism underlying the active-particle-like behavior of the immersed probe, we expand our scope to consider passive probes of different sizes (i.e. different probe boundary parameters) immersed in an ALP bath. In Part II, we always studied a probe of mass  $M = 100m$  and radius  $R_p = 3.0\sigma$ . We now maintain the mass to volume ratio of the probe from these chapters —  $M/\mathcal{V} = 25/(9\pi)m\sigma^{-3}$  — but change its radius so that the probe has the parameters shown in Table III.1. The equations of motion for the probe (see Eq. (9.2)) and the interacting ALPs in the bath (see Eq. (9.1)) remain the same.

$R_p$	$M$
$0.5\sigma$	$0.46296m$
$1\sigma$	$3.7037m$
$2\sigma$	$29.623m$
$3\sigma$	$100.00m$
$4\sigma$	$237.04m$

**Tab. III.1.:** List of probe radii ( $R_p$ ) investigated as well as their corresponding masses ( $M$ ), which maintain a constant probe mass to volume ratio of  $M/\mathcal{V} = 25/(9\pi)m\sigma^{-3}$ .

## Kinetic temperature

We first investigate the difference between the kinetic temperature of the probes in Table III.1 and that of the bath ALPs ( $\Delta k_B T \equiv k_B T_{\text{Probe}} - k_B T_{\text{ALP Bath}}$ ) — one active-particle-like property of the immersed probe. Here we define the kinetic temperature of both the probe and a bath ALP as (see Chapter 8):  $k_B T_{\text{eff}} = \frac{m}{d} \langle \mathbf{v}^2 \rangle$ , where  $m$  is the particle mass,  $d$  is the number of dimensions, and  $\langle \mathbf{v}^2 \rangle$  is the particle's mean squared velocity. We confirm in Appendix F that, for probes of all different sizes, the probe velocity distribution remains Gaussian in an active bath, as we found in Section 9.1 for a probe of  $R_p = 3.0\sigma$ .

We found in Section 9.1 that a probe of radius  $R_p = 3.0\sigma$  exhibits a higher kinetic temperature than that of the bath ALPs. As stated in Section 9.1, this is a distinct non-equilibrium signature: in equilibrium, we would expect the probe and ALP bath to have the same kinetic temperature, regardless of probe size. Given that our system is out of equilibrium and that we have already seen that the probe kinetic temperature does not necessarily equilibrate to that of the ALP bath, we would now like to understand how probe size affects kinetic temperature.

As expected in equilibrium, we find that  $\Delta k_B T = 0$  for a probe immersed in a passive bath, regardless of bath density and probe size (see Fig. 11.1). However, once the bath becomes active, the difference becomes dependent on both of these factors. In particular, the behavior of  $\Delta k_B T$  as a function of  $\hat{F}_0$  for a probe of  $R_p = 0.5\sigma$  differs significantly from its behavior for larger probes (compare Fig. 11.1a) with Figs. 11.1b-e)). We infer that this different behavior stems from the fact that, in the  $R_p = 0.5\sigma$  case, the probe radius is the same as that of the ALPs themselves. Therefore, the probe does not pose a significant obstacle and can be shoved relatively easily by the bath ALPs. This is not the case for larger probes, leading to different qualitative behavior of  $\Delta k_B T$  as a function of  $\hat{F}_0$ .

For all probes with radii  $R_p \geq 1.0\sigma$ ,  $\Delta k_B T \geq 0$  for baths of all densities and activities  $\hat{F}_0 > 0$ , meaning that the probe is ‘hotter’ than the ALP bath (see Figs. 12.2b-e)). Furthermore, in looking at Figs. 11.1b'-e'), we can see from graphing  $\Delta k_B T / \hat{F}_0^2$  as a function of  $\hat{F}_0$  that  $\Delta k_B T$  scales approximately quadratically to  $\hat{F}_0$  for probes of all radii  $R_p \geq 1.0\sigma$ . We note that  $\Delta k_B T$  only appears to scale quadratically with  $\hat{F}_0$  in Fig. 11.1a') because the values of  $\Delta k_B T$  are so close to zero. This quadratic



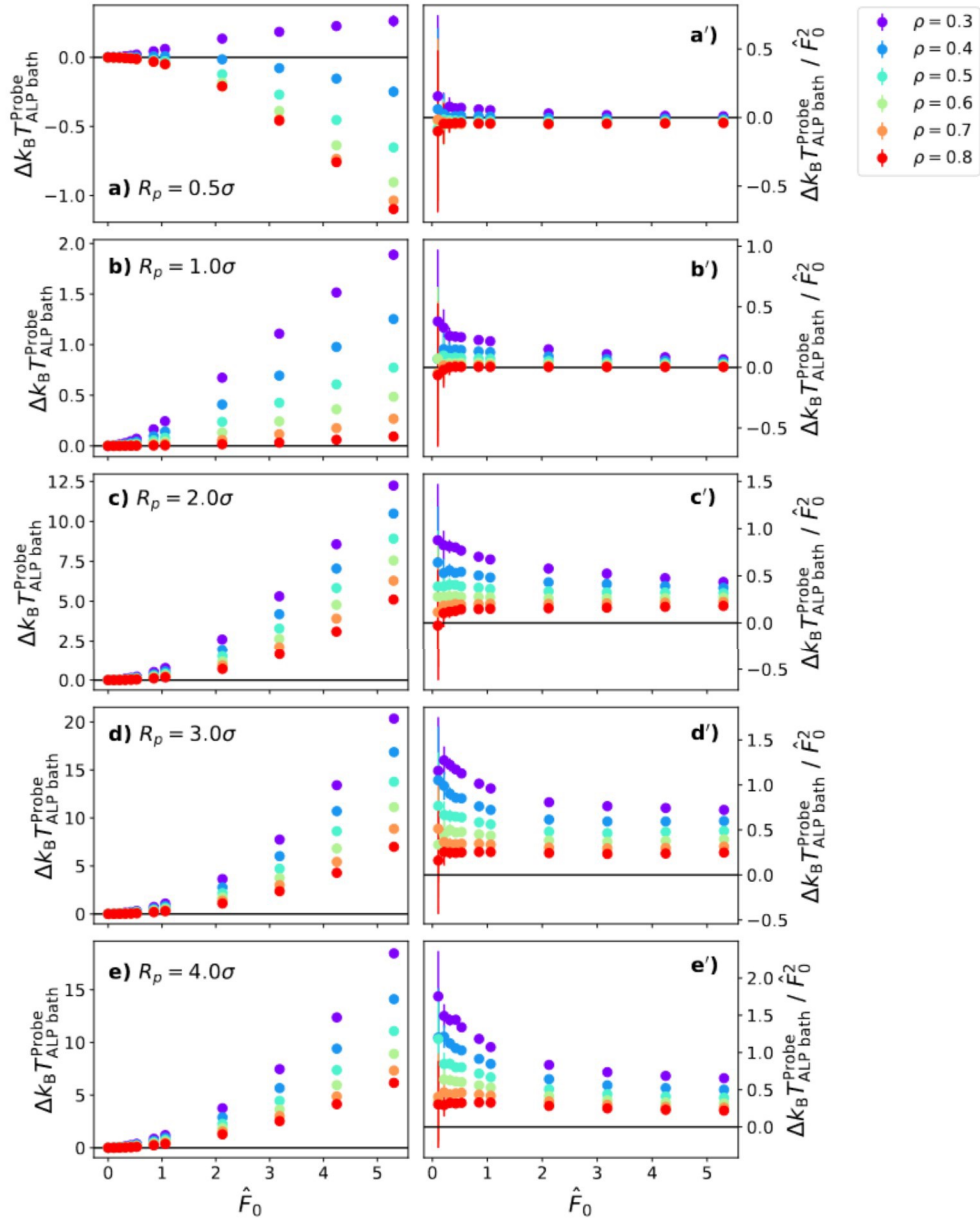


**Figure 11.1.:** Difference between the probe kinetic temperature and that of a bath ALP ( $\Delta k_B T_{\text{ALP Bath}}^{\text{Probe}} = k_B T_{\text{Probe}} - k_B T_{\text{ALP bath}}$ ) plotted as a function of the ALP active force ( $\hat{F}_0$ ) for immersed probes with different radii: **a/a')**  $R_p = 0.5\sigma$ , **b/b')**  $R_p = 1.0\sigma$ , **c/c')**  $R_p = 2.0\sigma$ , **d/d')**  $R_p = 3.0\sigma$ , and **e/e')**  $R_p = 4.0\sigma$ . **a-d)** The left column shows the unscaled difference, whereas **a'-d')** the right column shows the difference scaled by  $\hat{F}_0^2$ . Different colors show different bath densities ( $\rho$ ). All values of the density are expressed in LJ units of  $\sigma^{-3}$ . We show a solid black line at 0.

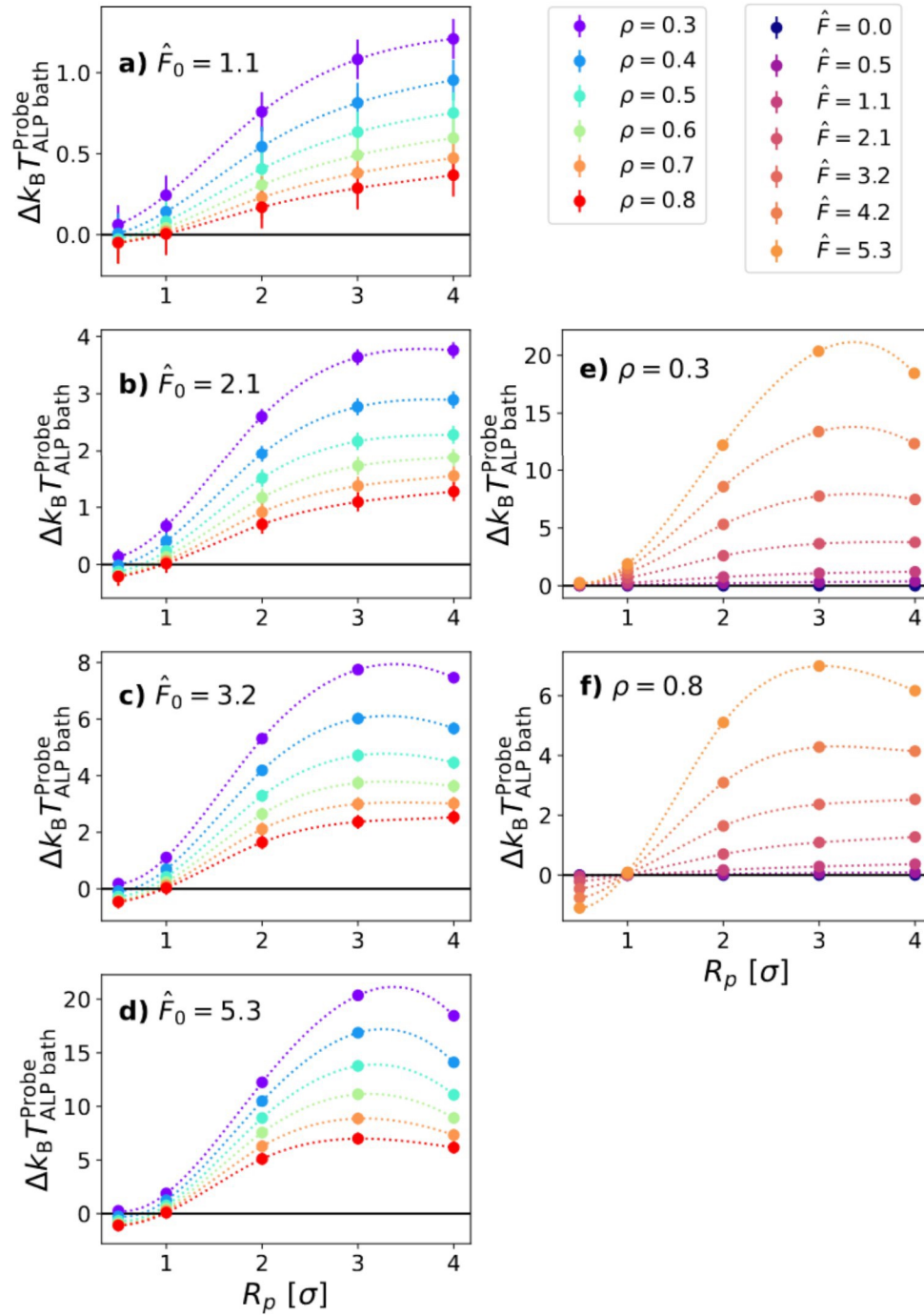
scaling of the kinetic temperature is the same which we found for an isolated ALP in Section 8.

In comparing  $\Delta k_{\text{B}}T$  for probes of different radii, we find that  $\Delta k_{\text{B}}T$  generally increases with the probe radius. However, upon closer examination of Figs. 11.1d) and e), we see that  $\Delta k_{\text{B}}T$  in fact has a non-monotonic relationship with the probe radius. To highlight this non-monotonic behavior, we plot  $\Delta k_{\text{B}}T$  as a function of the probe radius ( $R_p$ ) in Fig. 11.2.

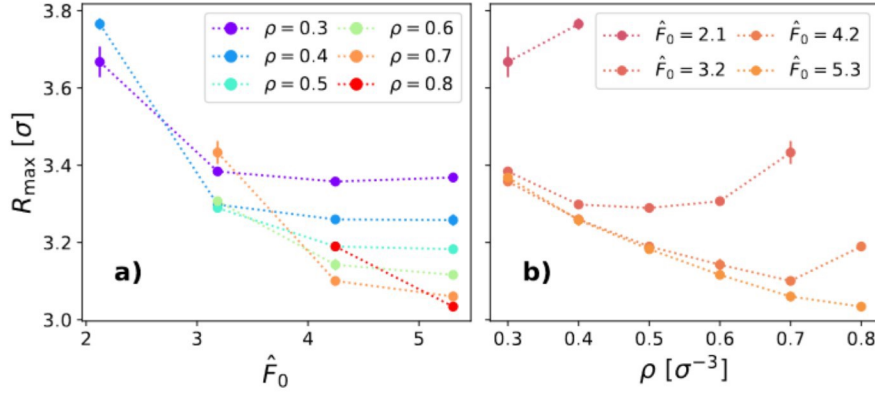
In examining Fig. 11.2, we see that  $\Delta k_{\text{B}}T$  only behaves non-monotonically for sufficiently high bath activities,  $\hat{F}_0 \gtrsim 2$ . This non-monotonicity occurs for ALP baths of all densities; however, the active force at which the onset occurs is density dependent. We also see in Fig. 11.2 that the maximum value of  $\Delta k_{\text{B}}T$  always occurs around  $R_p = 3.0\sigma$ , independent of bath density and activity. To get a better approximation of where this maximum occurs, we fit  $\Delta k_{\text{B}}T$  as a function of  $\hat{F}_0$  with a spline interpolation (shown as dotted lines in Fig. 11.2) and calculate the maximum of this interpolation ( $R_{\text{max}}$ ) if one exists, which is shown in Fig. 11.3. In Fig. 11.3 we only consider activities  $\hat{F}_0 > 0.2$  because of larger relative errors in the value of  $\Delta k_{\text{B}}T$  for very low activities.

Fig. 11.3 confirms that the non-monotonic behavior (i.e. the presence of  $R_{\text{max}}$ ) occurs at all densities, but only at higher active forces. For lower active forces, we do not see non-monotonic behavior; however, we cannot eliminate the possibility that a maximum exists because we have only studied radii up to  $R_p = 4.0\sigma$ . Fig. 11.3a) shows that, the higher the density of the bath, the higher the activity necessary for non-monotonic behavior to occur. We also see that, based on our interpolation,  $R_{\text{max}}$  is not strictly  $3.0\sigma$ , as it seemed in Fig. 11.2. Instead,  $R_{\text{max}}$  depends on both the activity and density of the bath. Based on Fig. 11.3a),  $R_{\text{max}}$  initially decreases with increasing bath activity and then plateaus. The plateau value of  $R_{\text{max}}$  decreases with increasing density. The fact that  $R_{\text{max}}$  decreases as  $\hat{F}_0$  increases indicates that  $R_{\text{max}}$  does not correspond to the persistence length of the ALPs, which grows with an increasing active force (see Appendix G).

We have now seen that probes of all sizes  $R_p \geq 1.0\sigma$  exhibit active-particle-like behavior in that they exhibit an enhanced kinetic temperature which scales quadratically with the bath activity. Furthermore, we have seen that  $\Delta k_{\text{B}}T$  has a non-monotonic relationship with the probe radius  $R_p$ . Therefore, we proceed to investigate the mechanism underlying this active-particle-like behavior as well as the cause of the non-monotonic behavior of  $\Delta k_{\text{B}}T$  as a function of the probe radius.



**Figure 11.2.:** Difference between the probe kinetic temperature and that of the ALP bath ( $\Delta k_B T_{\text{ALP bath}}^{\text{Probe}}$ ) plotted as a function of the probe radius ( $R_\rho$ ). In the left column, each plot shows ALP baths of different densities ( $\rho$ , each a different color) for a specific activity ( $\hat{F}_0$ ): **a)**  $\hat{F}_0 = 1.1$ , **b)**  $\hat{F}_0 = 2.1$ , **c)**  $\hat{F}_0 = 3.2$ , and **d)**  $\hat{F}_0 = 5.3$ . In the right column, each plot shows ALP baths of different activities ( $\hat{F}_0$ , each a different color) for a specific bath density ( $\rho$ ): **e)**  $\rho = 0.3\sigma^{-3}$  and **f)**  $\rho = 0.8\sigma^{-3}$ . All values of the density are expressed in LJ units of  $\sigma^{-3}$ .



**Figure 11.3.:** Radius of the probe ( $R_p$ ) at which  $\Delta k_B T$  reaches a maximum as determined by spline interpolation between the data points in Fig. 11.2. **a)** Maximum as a function of the active force  $\hat{F}_0$  where different colors represent different densities ( $\rho$ ). **b)** Maximum as a function of the bath density  $\rho$  where different colors represent different activities ( $\hat{F}_0$ ). Densities in the legend are expressed in LJ units of  $\sigma^{-3}$ .

We conclude this chapter with the comment that the significant dependence of the probe dynamics on its own boundary provides us with another non-equilibrium signature for a probe immersed in an active bath. In an equilibrium system, we would expect that probes of all sizes would equilibrate to the same kinetic temperature. Therefore, the fact that probes of different sizes achieve different kinetic temperatures in an active bath can be used as a non-equilibrium signature. In Section II, we proposed one non-equilibrium signature of a probe immersed in an active bath which can be determined only from the probe trajectory: the violation of the 1FDT. We now propose another non-equilibrium signature of this system which can be determined from the trajectories of differently sized probes: different kinetic temperatures for probes of different sizes in the same active bath. However, this new non-equilibrium signature requires the simultaneous study of two probes and cannot be identified based on one probe trajectory alone.

## Transparent, convective probe

We have seen that all probes  $R_p \geq 1.0\sigma$  exhibit an enhanced kinetic temperature, which scales quadratically with the bath activity, similar to an ALP itself. But is this active-particle-like behavior purely due to the convective properties of the active bath, or does the interface between the probe and the active bath contribute to this behavior? In order to answer this question, we again consider a bath of ALPs with mass  $m$  and velocity  $\mathbf{v}_i$  in three dimensions. As stated in Chapter 8, the kinetic temperature of a bath ALP is given by  $k_B T_{\text{ALP bath}} = \frac{m}{d} \langle \mathbf{v}^2 \rangle$ , where  $d$  is the dimensionality of the system; hence,  $\langle \mathbf{v}^2 \rangle = \frac{d}{m} k_B T_{\text{ALP bath}}$ . We now consider a transparent, convective probe particle ('bubble') immersed in the bath (see Fig. 12.1). This bubble covers a volume  $\mathcal{V} = 4/3\pi R_p^3$  and swims with the bath ALPs without otherwise affecting them. Namely, if ALPs  $j = 1 \dots N$  are contained in the volume  $\mathcal{V}$  of the bubble, then its velocity is  $\mathbf{V} = \frac{1}{N} \sum_{j=1}^N \mathbf{v}_j$  and its squared velocity is  $\langle \mathbf{V}^2 \rangle = \frac{1}{N^2} \sum_{jk} \langle \mathbf{v}_j \mathbf{v}_k \rangle$ . In the simplest case, if the ALPs are totally uncorrelated, then  $\langle \mathbf{V}^2 \rangle = \frac{1}{N} \langle \mathbf{v}^2 \rangle = \frac{d}{Nm} k_B T_{\text{ALP bath}}$ .

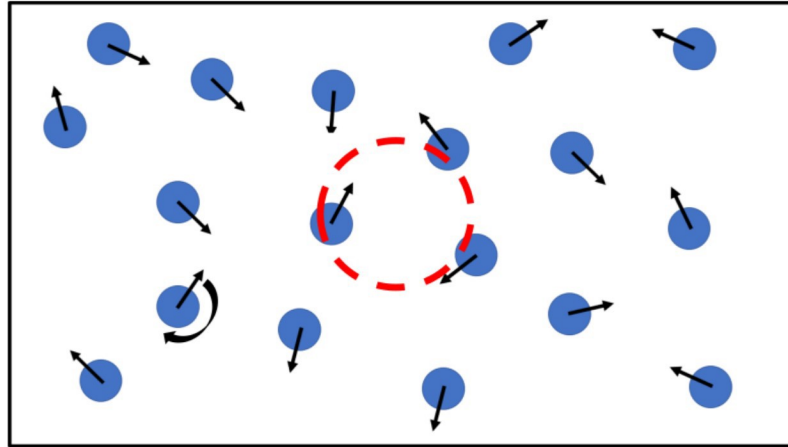


**Figure 12.1.:** System of a transparent, convective probe ('bubble') immersed in a bath of active Langevin particles.

We now assign a hypothetical mass  $M$  to the bubble, so that we can determine its hypothetical kinetic temperature,  $k_B T_{\text{Probe}}$ . For the uncorrelated ALP particles, we obtain  $T_{\text{Probe}} = \frac{M}{Nm} T_{\text{ALP bath}}$ . For an ALP bath of density  $\rho$ , the number of particles contained in volume  $\mathcal{V}$  is  $N = \rho\mathcal{V}$ . Thus, for uncorrelated ALPs:

$$\frac{\rho T_{\text{Probe}}}{T_{\text{ALP bath}}} = \frac{M}{m\mathcal{V}}. \quad (12.1)$$

For purposes of comparison, we now consider bubbles with the radii and corresponding hypothetical masses listed in Table III.1. From Eq. (12.1), given our ALP mass and the probe mass to volume ratio (which is kept constant as  $M/\mathcal{V} = 25/(9\pi)m\sigma^{-3}$  for probes of all radii), we expect that  $T_{\text{Probe}} > T_{\text{ALP bath}}$  for a bubble in a bath of uncorrelated ALPs with  $\rho < 1\sigma^{-3}$ . This relation is thus consistent with the results in Sections 9.1 and 11 for a hard probe. Therefore, without further investigation, it could be inferred that the hard probe's enhanced kinetic temperature is simply due to the convective properties of the bath.

However, our ALPs are not necessarily uncorrelated. To assess the correlations within the ALP bath, we calculate  $\Lambda_{\text{Bubble}} \equiv \rho T_{\text{Probe}}/T_{\text{ALP bath}}$  for simulations of a transparent, convective probe immersed in an ALP bath. We then compare these values to the theoretical value for a bath of uncorrelated ALP particles (Eq. (12.1)) in Figs. 12.2a'-e').

We first remark that analyzing a bubble of radius  $R_p = 0.5\sigma$  (Fig. 12.2a')) does not provide us with additional insight because, in this case, the volume of the bubble is identical to that of an ALP. Therefore, the bubble simply tracks a singular bath ALP. We thus expect that  $T_{\text{Probe}}/M = T_{\text{ALP Bath}}/m$ , so  $\Lambda_{\text{Bubble}} = \rho M/m$  for all values of activity, which agrees with our results in Fig. 12.2a').

In Fig. 12.2b'), we see that the behavior of a bubble with radius  $R_p = 1.0\sigma$  also shows qualitatively different behavior from bubbles with larger radii. We infer that this behavior is due to the small bubble volume. In high density baths, the bubble behavior approaches that of larger bubbles because the bath is sufficiently dense that multiple particles are encompassed within the bubble volume. However, in low density baths, the bubble encompasses, at most times, only one ALP and, consequently, its behavior approaches that of a single ALP.

For bubbles with radii  $R_p > 1.0\sigma$  in passive and low activity baths, we find that  $\Lambda_{\text{Bubble}}$  calculated from simulation data matches that predicted for a bath of uncorrelated ALP particles (Eq. (12.1)) very well, regardless of bath density. This indicates that, in our ALP bath model, for passive and low activity baths, the motion of bath ALPs is uncorrelated. However, as the activity of the bath increases, we see that our theoretical model for the bubble underestimates the value of  $\Lambda_{\text{Bubble}}$ , indicating that correlations between bath particles emerge with increased activity. These correlations become even more pronounced in higher density baths.

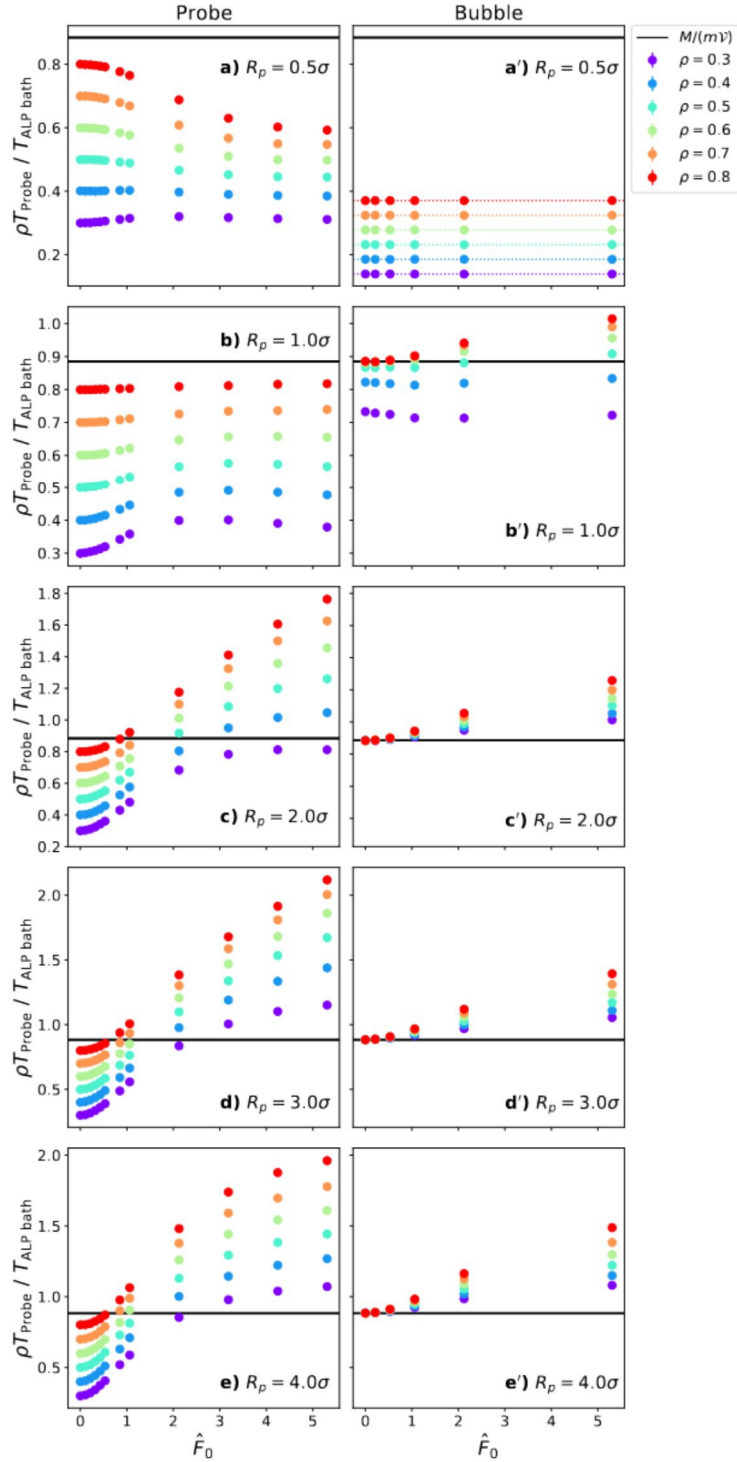


**Figure 12.2.:** Ratio of the probe temperature ( $T_{\text{Probe}}$ ) to that of a bath ALP ( $T_{\text{ALP bath}}$ ) scaled by the bath density ( $\rho$ ) and plotted as a function of the ALP active force ( $\hat{F}_0$ ) for immersed probes with different radii: **a/a')**  $R_p = 0.5\sigma$ , **b/b')**  $R_p = 1.0\sigma$ , **c/c')**  $R_p = 2.0\sigma$ , **d/d')**  $R_p = 3.0\sigma$ , and **e/e')**  $R_p = 4.0\sigma$ . **a-e)** For a probe with a hard boundary. **a'-e')** For a transparent, convective probe. The solid black line in each graph shows the value predicted for a bath of uncorrelated ALPs (Eq. (12.1)). The colored, dotted lines in **a')** show  $\rho M/m$ . Densities in the legend are expressed in LJ units of  $\sigma^{-3}$ .

We now assess how the boundary of the probe affects the correlations among bath ALPs by calculating the ratio  $\Lambda_{\text{Probe}} \equiv \rho T_{\text{Probe}}/T_{\text{ALP bath}}$  for a hard probe (see Figs. 12.2a-e)). We consider hard probes with radius and mass parameters listed in Table III.1. For a hard probe immersed in a passive bath, the probe and bath will be in thermal equilibrium such that  $T_{\text{Probe}} = T_{\text{bath}}$ ; therefore,  $\Lambda_{\text{Probe}} = \rho$ , as is shown for passive probes of all sizes immersed in passive baths of all densities in Fig. 12.2.

Given that, for bubbles of  $R_p = 0.5\sigma$  and  $R_p = 1.0\sigma$ , the bubble often only tracks a single ALP particle, comparing  $\Lambda_{\text{Probe}}$  and  $\Lambda_{\text{Bubble}}$  for probes of these sizes does not reveal the effects of the probe boundary on probe dynamics. Therefore, we do not discuss a comparison between  $\Lambda_{\text{Probe}}$  and  $\Lambda_{\text{Bubble}}$  for probes of  $R_p = 0.5\sigma$  and  $R_p = 1.0\sigma$ . We do, however, note that the behavior of  $\Lambda_{\text{Probe}}$  as a function of  $\hat{F}_0$  for small probes ( $R_p \leq 1.0\sigma$ ) qualitatively differs from that which we see for probes of larger radii. We infer that these qualitative differences result from the fact that the probe and the ALPs are on the same length scale.

For all probes  $R_p > 1.0\sigma$ ,  $\Lambda_{\text{Probe}} < \Lambda_{\text{Bubble}}$  for low bath activities. For high bath activities,  $\Lambda_{\text{Probe}} > \Lambda_{\text{Bubble}}$ . This means that, for low bath activities, the probe boundary *anti-correlates* the bath particles. In the passive case, this anti-correlation is necessary for the probe to come to thermal equilibrium with the bath. For high bath activities, on the other hand, the probe boundary *correlates* the bath particles.

The most important, if perhaps also most general, conclusion to be drawn from comparing  $\Lambda_{\text{Probe}}$  to  $\Lambda_{\text{Bubble}}$  is that — for a given bath density, bath activity, and probe radius — they are not the same (i.e. Figs. 12.2a-e) are not equivalent to Figs. 12.2a'-e')). Therefore, the dynamics of the immersed hard probe are not solely due to the convective properties of the bath. Rather, the probe boundary affects the correlations within the ALP bath, which then influence the probe behavior.



## Spherical harmonics

Given that the probe boundary plays an important role in both the dynamics of the immersed probe and the correlations in the ALP bath, we now examine the properties of the ALP fluid in the vicinity of the probe. We do this for probes of all sizes listed in Table III.1. We examine the ALP fluid properties by calculating the spherical harmonics of the ALP bath with respect to the instantaneous velocity of the probe ( $\mathbf{V}$ ) as a function of distance from the probe (see Appendix H).

From these spherical harmonics, we calculate the density of the bath fluid as a function of the distance from the center of the immersed probe as:

$$\rho(r) = \frac{\sqrt{4\pi}}{\mathcal{V}} \sum_{i \in \delta\mathbf{r}} Y_0^0(\mathbf{r}_i/r_i). \quad (13.1)$$

Here,  $Y_0^0(\mathbf{r}_i/r_i)$  is the spherical harmonic  $l = m = 0$  associated with bath particle  $i$ , which lies within spherical shell  $\delta\mathbf{r}$  of volume  $\mathcal{V}(r) = 4/3\pi((r + \delta r/2)^3 - (r - \delta r/2)^3)$ . Ref. [88] analytically found that, for a sphere immersed in a dilute 3D system of ABPs, the ABP concentration is exponentially screened. We now examine the density profile surrounding a spherical probe immersed in a dense 3D system of ALPs through simulation data. We can see in Figs. 13.1a-e) that, even in a bath of density  $\rho = 0.4\sigma^{-3}$ , our bath is sufficiently dense to show oscillations before approaching the bulk density.

In comparing the density curves for a passive and an active bath in Figs. 13.1a-e), we see that the first peak of the density curve is higher in an active bath for probes of all radii. This means that adding activity to the bath leads to a higher density of bath particles in the vicinity of the probe. Interestingly, we see that the magnitude of increase in the peak density is non-monotonic with the probe radius. Similarly to the behavior of  $\Delta k_B T$ , this difference reaches a maximum for a probe of  $R_p = 3.0\sigma$  and then decreases for a probe of  $R_p = 4.0\sigma$ .

We also see that the initial peak of the active bath density profile is shifted slightly closer to the probe center in comparison with that of the passive bath, again independent of probe radius. This shift indicates that ALPs are able to move closer to the probe than passive bath particles. We infer that this ability stems from the higher

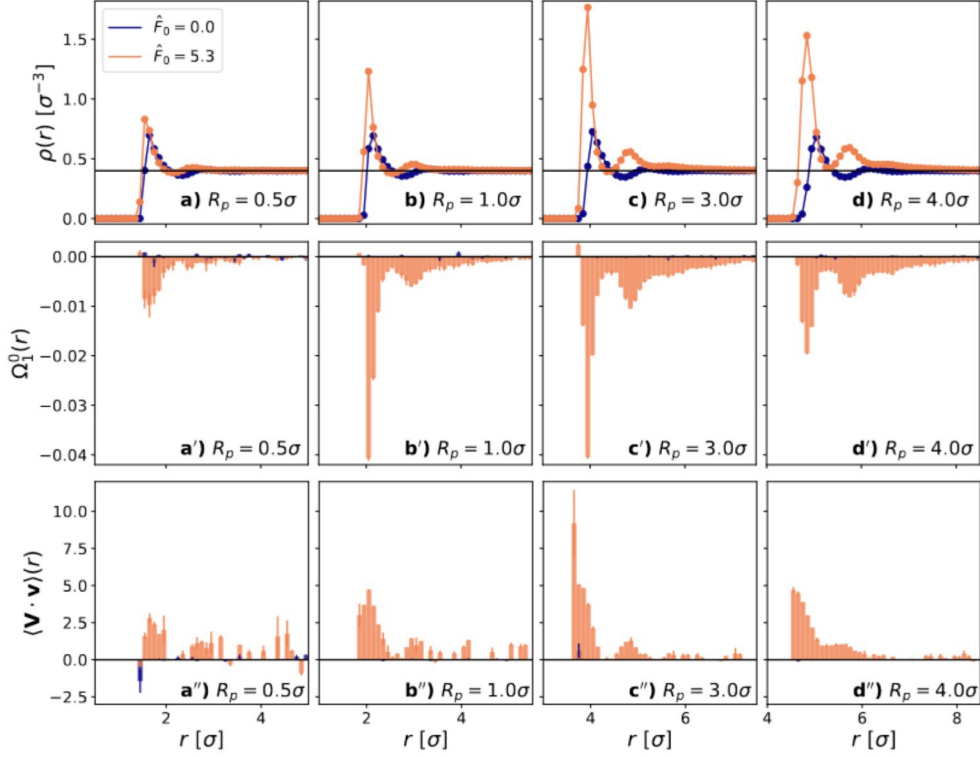


**Figure 13.1.:** **a-d)** Density of the bath ( $\rho(r)$ ) in LJ units of  $\sigma^{-3}$ , **a'-d')** dipole moment of the bath ( $\Omega_1^0(r)$ , see Eq. (13.2)), and **a''-d'')** alignment of the ALP velocities with that of the probe velocity ( $\langle \mathbf{V} \cdot \mathbf{v} \rangle(r)$ , see Eq. 13.3) as a function of distance from the center of the immersed probe ( $r$ ) for baths of average density  $\rho_0 = 0.4\sigma^{-3}$ . Each column shows a probe of a different radius: **a/a'/a''**)  $R_p = 0.5\sigma$ , **b/b'/b''**)  $R_p = 1.0\sigma$ , **c/c'/c''**)  $R_p = 3.0\sigma$ , and **d/d'/d''**)  $R_p = 4.0\sigma$ . For ease of visualization, in **a-d)** we show a black line at the global density and in **a'-d')** and **a''-d'')** we show a black line at 0.

kinetic energy of ALPs due to their active force, which allows them to overcome more of the repulsive potential from WCA interactions with the probe.

In addition to calculating the density, we also calculate higher order spherical harmonics of the bath as a function of distance from the probe:

$$\Omega_l^m(r) = \frac{1}{V} \sum_{i \in \delta \mathbf{r}} Y_l^m(\mathbf{r}_i/r_i). \quad (13.2)$$

From Figs. 13.1**a'-d')**, we see that the ALP bath acquires a negative dipole moment surrounding the probe, which is sustained to large values of  $r$ . This negative dipole moment indicates that ALPs collect behind the probe relative to its instantaneous velocity, even at large distances from the probe. This non-zero dipole moment of an ALP bath surrounding a probe is in contrast to the dipole moment of a passive bath

surrounding a probe, which is zero. We find no significant structure in higher order spherical harmonics for either the active or passive bath.

We can see that the first negative peak in the dipole moment occurs at approximately the same location as the first peak in the fluid density profile. Therefore, we infer that the increased peak density of an active bath fluid (relative to that of a passive bath fluid) is primarily due to the accumulation of ALPs behind the probe relative to its instantaneous velocity. This mechanism of active particles gathering behind an immersed passive probe has previously been seen for a probe dragged through an ABP bath in Ref. [99], where it is framed as a difference between the forces behind and in front of the probe.

The small values of  $\Omega_1^0(r)$  for a probe of radius  $R_p = 0.5\sigma$  demonstrate that the accumulation mechanism is not significant in a probe of this size. The failure of this mechanism can be explained intuitively: the probe has the same size (in volume) as the ALPs themselves, therefore significant accumulation is not possible. This lack of accumulation helps to explain why the behavior of  $\Delta k_B T$  as a function of  $\hat{F}_0$  for a probe of  $R_p = 0.5\sigma$  differs significantly from probes with larger radii (see Fig. 11.1).

We infer that the velocities of the ALPs collected behind the probe become correlated, causing the enhanced correlations among high activity bath ALPs that we saw in comparing  $\Lambda_{\text{Bubble}}$  and  $\Lambda_{\text{Probe}}$  in Fig. 12.2). We then infer that the ALPs proceed to *push* the probe. To assess this hypothesis, we calculate the alignment of ALP velocities with that of the probe as:

$$\langle \mathbf{V} \cdot \mathbf{v} \rangle(r) = \frac{1}{\rho(r)} \sum_{i \in \delta \mathbf{r}} \mathbf{V} \cdot \mathbf{v}_i. \quad (13.3)$$

Figs. 13.1a''-d'', confirm that the ALPs in the vicinity of the probe are, in fact, aligned with that of the probe, supporting our hypothesis of this pushing mechanism. We see in Figs. 13.1a''-d'' that the height of the maximum peak in  $\langle \mathbf{V} \cdot \mathbf{v} \rangle(r)$  has a non-monotonic relationship to the probe radius, much like  $\Delta k_B T$  and the maximum of the density peak. The maximum peak of  $\langle \mathbf{V} \cdot \mathbf{v} \rangle(r)$  occurs, once again, at approximately  $R_p = 3.0\sigma$ .

We furthermore infer that the pushing by the ALPs promotes the enhanced kinetic temperature of the probe and induces its active-particle-like behavior (i.e. VACF and memory kernel behavior). Indeed, we can see in Fig. 13.2 that the kinetic temperature difference between the immersed probe and the ALP bath is positively correlated with the average magnitude of the negative dipole moment ( $\langle \Omega_1^0 \rangle$ ).

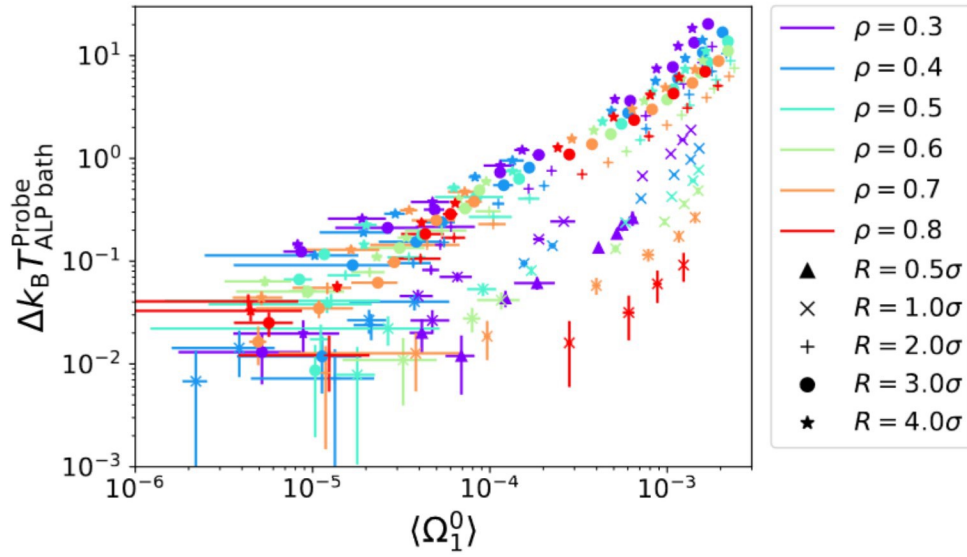


**Figure 13.2.:** Kinetic temperature difference between the immersed probe and the ALP bath as a function of the absolute value of the average dipole moment,  $\langle \Omega_1^0 \rangle$ . Data for all simulated bath densities ( $\rho$ ) and activities ( $\hat{F}_0$ ), as well as for all probe radii ( $R_p$ ), are shown. Different probe radii are distinguished by different symbols and different bath densities are distinguished by different colors. Bath activities are not distinguished. Densities in the legend are expressed in LJ units of  $\sigma^{-3}$ .

We note that this positive correlation primarily occurs for probes of radii  $R_p > 1.0\sigma$ . For probes of  $R_p = 0.5\sigma$ , only very few points are shown because of relatively large errors in  $\langle \Omega_1^0 \rangle$ . For probes of  $R_p = 1.0\sigma$ , we see a cluster of points in the lower right corner of the graph. The location of this cluster indicates that, in spite of high values of  $\langle \Omega_1^0 \rangle$ ,  $k_B T$  remains low. We infer this weaker coupling between  $\langle \Omega_1^0 \rangle$  and  $k_B T$  stems from the similarity in size between the probe and the bath ALPs.

## Part III: conclusions and outlook

We have shown that the active-particle-like behavior and enhanced kinetic temperature of a probe immersed in an active bath cannot simply be attributed to the convective motion of the active bath. The boundary of the probe contributes significantly to these adopted dynamics. The probe boundary causes active bath particles to accumulate behind the probe with respect to its instantaneous velocity. Once gathered behind the probe, particles are forced to move in the same direction, leading to correlations among bath particles with sufficiently high activity. This gathering of active bath particles pushes the probe, which in turn promotes the active-particle-like behavior, in particular the enhanced kinetic temperature, of the probe.

These boundary interactions, and consequently the dynamics of both the probe and the active fluid, are highly contingent on the specific configuration of the probe boundary. For probes with a radius approximately equal to that of the bath particles, the accumulation mechanism is significantly less effective. Furthermore, the kinetic temperature difference between the probe and the active fluid is dependent on the probe radius. The variability the boundary interactions furnishes us with another non-equilibrium signature of a probe immersed in an active bath: probes of different sizes acquire different kinetic temperatures, even when immersed in the same active bath.

We additionally found that the kinetic temperature difference between the immersed probe and the active bath scales non-monotonically with the probe size. Though we found that this non-monotonicity was consistent in other investigated quantities (e.g. alignment between bath particles and probe, peak density, and average negative dipole moment), we did not find the physical reason for the existence of such a maximum. We leave determining this mechanism, and ascertaining whether this behavior is specific to our system or universal, as a question for future work.

Because our active particles are coupled to a Langevin thermostat, the hydrodynamic interactions in the fluid are effectively screened. In future work, it would be interesting to study systems in with hydrodynamic interactions, which would certainly

impact the correlations within both the passive and the active fluid. Furthermore, given the importance of the boundary in both the dynamics of the probe and the active fluid, it would be interesting to consider a boundary with localized deformations. It has been shown that such boundary deformities can induce long-range effects in the bulk active fluid [124], which may in turn alter the dynamics of the immersed probe.

# Part IV

---

Probe immersed in an active bath subject  
to external forces

Many microrheological studies rely on subjecting a probe to an external force to determine the properties of the immersive medium (see Chapter 5). This is true for both experimental and computational microrheological studies. These external forces often take the form of either constant, drag forces or harmonic, trapping forces. Such studies have recently been applied to probe the microrheological properties of active systems [26, 99, 125, 126, 127, 128]. A number of these studies cite violations of [26, 29], or necessary modifications to [127], fluctuation dissipation theorems among their findings.

The dynamics of a probe subject to a constant drag force or a harmonic trapping force can be coarse-grained onto a GLE with an additional external force term. These GLEs can be transformed into Volterra equations in the same way that we transformed Eq. (2.13) into Eq. (2.14) in Chapter 2 [24, 33]. This inverse Volterra equation can then be inverted to define the memory kernel of the probe. Ref. [33] has shown that when a particle's dynamics are mapped onto a GLE where the memory kernel is defined by a Volterra equation, the 2FDT will always be fulfilled. Therefore, probes immersed in active baths and subject to harmonic and constant external forces can be mapped onto GLEs which fulfill the 2FDT. The question remains, however, how to reconcile such a GLE which fulfills a 2FDT with the physical interpretations found in previous studies.

To this end, we now subject a probe immersed in an active bath to two different types of external forces: a constant, 'drag' force and a harmonic, trapping force. We then map the dynamics of the probe onto a GLE and use the inverse Volterra method to determine a memory kernel for the probe which will fulfill the 2FDT. The central goal of this section is to understand the physical implications of such a GLE mapping.



## Harmonic potential

We trap the immersed probe in a harmonic potential such that its equation of motion is:

$$M\dot{\mathbf{V}}(t) = -\nabla U_{\text{Harm}}(|\mathbf{R} - \mathbf{R}_0|) - \sum_n \nabla U_{\text{WCA}}(\mathbf{R} - \mathbf{r}_n), \quad (15.1)$$

where  $M$  is the mass of the probe,  $\mathbf{V}(t)$  is its velocity, and  $U_{\text{WCA}}(\mathbf{R} - \mathbf{r}_n)$  is the WCA potential due to an ALP particle,  $n$ , at position  $\mathbf{r}_n$ .  $U_{\text{Harm}}(|\mathbf{R} - \mathbf{R}_0|) = \frac{1}{2}k|\mathbf{R} - \mathbf{R}_0|^2$  is the harmonic, trapping potential with trapping constant  $k$  and trap center  $\mathbf{R}_0$ . We test three different values of  $k$ :  $k = 1, 5, \text{ and } 10$  in LJ units of  $\epsilon\sigma^{-2}$ . Aside from the external, trapping force, the immersed probe only experiences forces from interactions with the surrounding ALPs. The ALPs are described by Eq. (9.1).

Because the probe is now subject to a potential, we must slightly alter the GLE to which we map our system dynamics. Our GLE now reads:

$$M\dot{\mathbf{V}}(t) = -\nabla U_{\text{Harm}}(|\mathbf{R} - \mathbf{R}_0|) - \int_0^t ds K(t-s)\mathbf{V}(s) + \mathbf{\Gamma}(t). \quad (15.2)$$

Eq. (15.2) can be transformed into a Volterra equation analogously to Eq. (2.13) (see Chapter 2). Following the same procedure outlined in Ref. [17], we can then reconstruct the memory kernel as [24]:

$$K(m\Delta t) = \frac{\frac{1}{M}C_F(m\Delta t) - kC_V(m\Delta t) - \frac{\Delta t}{M} \sum_{n=0}^{m-1} \omega_n C_{FV}((m-n)\Delta t)K(n\Delta t)}{C_V(0) + \frac{\Delta t \omega_m}{M} C_{FV}(0)}, \quad (15.3)$$

where the initial condition is now  $K(0) = \frac{1}{M} \frac{C_F(0)}{C_V(0)} - k$ .

### 15.1 Position probability distribution

In equilibrium, we know that a harmonically trapped particle has a Gaussian position distribution centered at the trap center with variance  $\langle r_i^2(t) \rangle = k_B T/k$  for each harmonically trapped axis  $i$ . As expected, this matches what we find for a probe immersed in a passive bath, as we can see in Fig. 15.1a), which shows the position

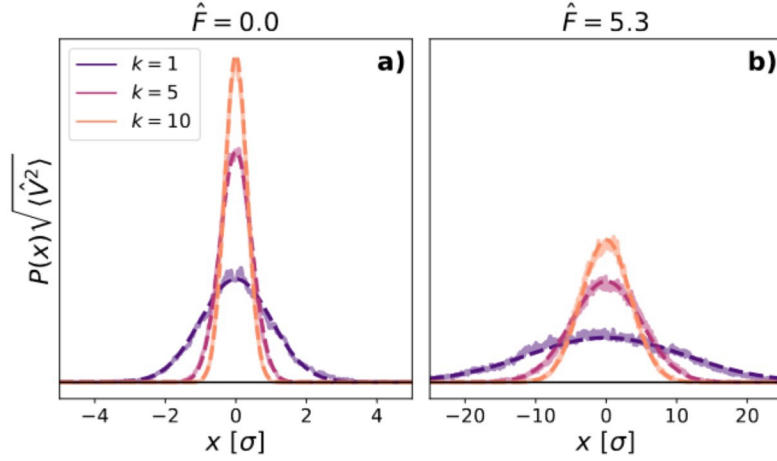


**Figure 15.1.:** Position distribution relative to the trap center ( $P(x)$ ) of a harmonically trapped probe immersed in **a)** a passive ( $\hat{F}_0 = 0.0$ ) and **b)** an active bath ( $\hat{F}_0 = 5.3$ ). Solid lines show simulation data, whereas dashed lines show a Gaussian distribution with mean 0 and the variance **a)** expected for a probe in a harmonic potential with each respective spring constant  $k$  and **b)** of the simulation data. Each bath has average density  $\rho_0 = 0.4\sigma^{-3}$ . Values of  $k$  in the legend are shown in LJ units of  $\epsilon\sigma^{-2}$ .

distribution of the probe in the x-direction relative to the trap center. Although we only show the position distribution in the x-direction, since the probe is confined along all axes, we find the same form of position distribution in both the y and z directions as well.

We see in Fig. 15.1b), that the position distribution of the probe remains Gaussian and centered around the trap center even in an active bath. However, although the position probability distribution is, as in equilibrium, Gaussian distributed around the center of the trap, the variance of the probe position distribution is not that which we expect in equilibrium. Even when we account for the higher kinetic temperature of the probe immersed in an active bath ( $k_B T_{\text{eff}} = m\langle v^2(t) \rangle / 3$  in 3D), we find that  $k_B T_{\text{eff}} / \langle r_i^2(t) \rangle \neq k$ , as can be seen in Fig. 15.2 where we plot  $k_B T_{\text{eff}} / \langle r_i^2(t) \rangle$  as a function of  $k$ . Furthermore, we see in Fig. 15.2 that the value of  $k_B T_{\text{eff}} / \langle r_i^2(t) \rangle$  for a given constraint  $k$  is not density independent in the active case, as we would expect in equilibrium.

Although  $k_B T_{\text{eff}} / \langle r_i^2(t) \rangle \neq k$  for a harmonically confined probe in an active bath, it does appear that  $k_B T_{\text{eff}} / \langle r_i^2(t) \rangle \propto k$ . We therefore posit that, due to the activity of the bath particles, in order to make a coarse-grained model of a probe immersed in an active bath, the external force on the probe needs to be *renormalized*. Then,  $k_B T_{\text{eff}} / \langle r_i^2(t) \rangle = \tilde{k}$  for the active bath, where  $\tilde{k} = \alpha k$  is the renormalized spring constant of the harmonic potential with renormalization factor  $\alpha$ .

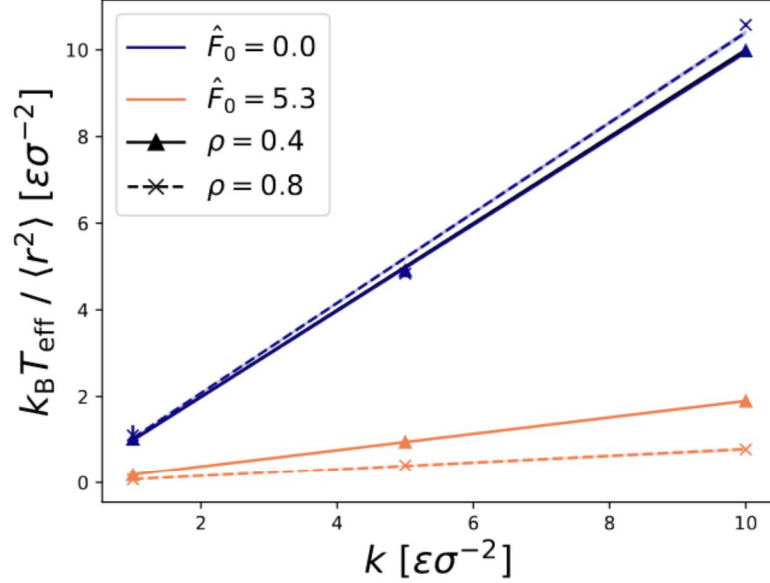


**Figure 15.2.:**  $k_B T_{\text{eff}} / \langle r_i^2(t) \rangle$  as a function of  $k$  for a probe immersed in a passive bath ( $\hat{F}_0 = 0.0$ , indigo) as well as for a probe immersed in an active bath ( $\hat{F}_0 = 5.3$ , orange). We show data for both a bath with a density of  $\rho_0 = 0.4$  (triangles) and of  $\rho_0 = 0.8\sigma^{-3}$  (x-symbol). Solid colored lines show the line of best fit for baths with density  $\rho_0 = 0.4\sigma^{-3}$ , whereas dashed colored lines show the line of best fit for baths with density  $\rho_0 = 0.8\sigma^{-3}$ . The solid black line shows  $k_B T_{\text{eff}} / \langle r_i^2(t) \rangle = k$ . Densities in the legend are expressed in LJ units of  $\sigma^{-3}$ .

To determine the renormalization factor  $\alpha$ , we fit our data in Fig. 15.2 to a line with zero offset. As expected, in the passive case,  $\alpha \approx 1$  for both bath densities because the external force does not need to be renormalized and is density independent. In the active case, we find that for a bath with density  $\rho = 0.4\sigma^{-3}$ ,  $\alpha_{0.4} = 0.190 \pm 0.001$  and for a bath with density  $\rho = 0.8\sigma^{-3}$ ,  $\alpha_{0.8} = 0.079 \pm 0.002$ . In both cases,  $\alpha < 1$ , meaning that the activity of the bath effectively decreases the spring constant of the harmonic potential and, thereby, decreases the trapping force exerted on the probe.

## 15.2 Velocity autocorrelation function and memory kernel

We now examine the VACF and memory kernel of the trapped probe. From Figs. 15.3a) and b), we see that, when immersed in a passive bath, the VACF/memory kernel of a harmonically constrained probe only differs slightly from that of an unconstrained probe. Namely, the oscillation of the VACF for a harmonically con-

strained probe is slightly deeper than that for an unconstrained probe. The increased depth of this oscillation relates to the restoring force on the probe; therefore, we expect that its depth would increase with an increased value of  $k$ , which agrees with what we see in Fig. 15.3a). The memory kernel of a free vs. trapped probe in a passive bath exhibits even fewer differences. In fact, the differences between the memory kernel of a free vs. trapped particle all fall within our error bounds.

When immersed in an active bath, the VACF/memory kernel of the harmonically constrained probe differs more significantly from that of an unconstrained probe. In Fig. 15.3c), we see that the trapped probe has a decreased local kinetic temperature in comparison with that of a free probe. This difference is not surprising given the constraint on the probe.

What is surprising is the long-time tail which the harmonic constraint incites in the VACF. In Fig. 15.3c), we see that the VACF of a free probe immersed in an active bath decays at times  $\hat{t} \sim \mathcal{O}(10^2)$ . This is no longer the case when the probe is constrained. When subject to a harmonic constraint, the VACF exhibits an oscillation which has still not completely decayed at times  $\hat{t} \sim \mathcal{O}(10^3)$ . The oscillation of the VACF in the active case of a harmonically constrained probe can be understood much the same as the increased depth of the oscillation in the passive case: the oscillation results from an increased restoring force on the probe. We suspect that this failure of the VACF to fully decay on the time scale which we studied leads to the slight negative offset in the memory kernel (see the inset of Fig. 15.3d)).

## 15.3 Stochastic force distribution

Once we have determined the memory kernel of the probe, it is straightforward to determine the stochastic force ( $\mathbf{\Gamma}(t)$ ) in Eq. (15.2):

$$\mathbf{\Gamma}(t) = \mathbf{F}(t) + \nabla U_{\text{Harm}}(|\mathbf{R} - \mathbf{R}_0|) + \int_0^t ds K(t-s)\mathbf{V}(s). \quad (15.4)$$

The only difference between Eq. 15.4 and Eq. 2.19 — which we used to derive the stochastic force for a free probe — is the extra term to account for the external, harmonic force.

In Fig. 16.5, we see that in both the case of a passive and an active bath, the stochastic force distribution calculated from simulation data (solid lines) approximately matches a zero-centered Gaussian with the same standard deviation (dashed lines). The only deviations from the zero-centered Gaussian are an enhanced peak in the

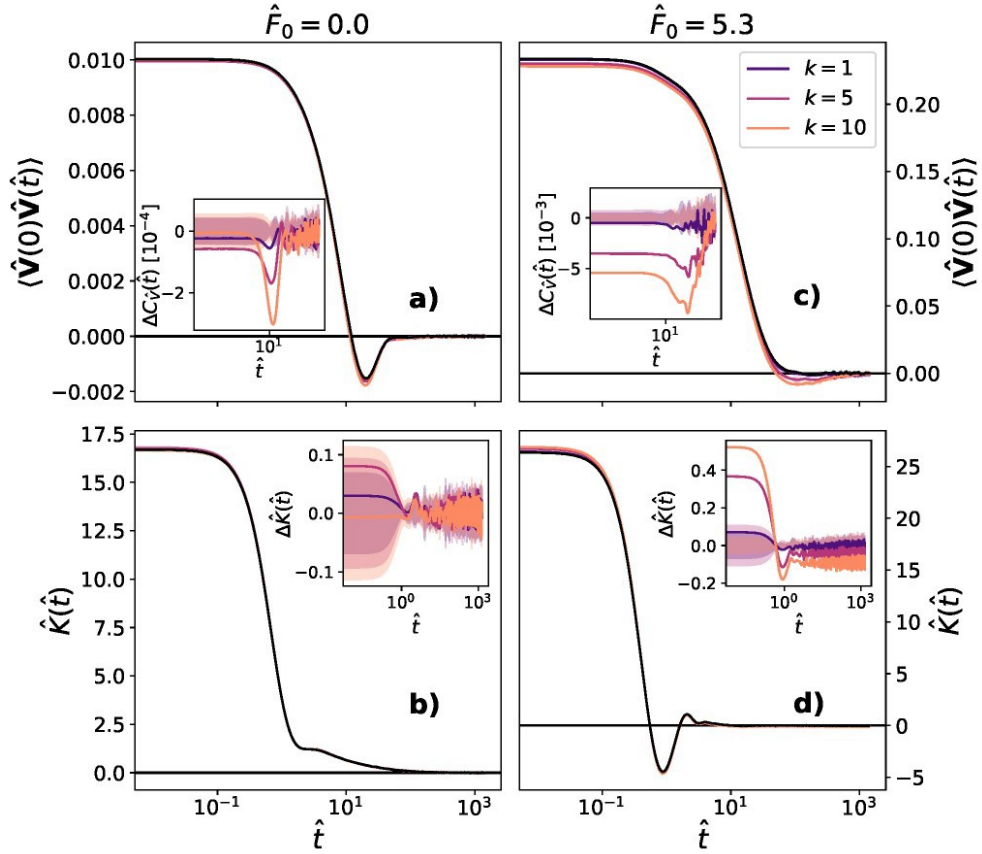


**Figure 15.3.:** Velocity autocorrelation function (VACF) and memory kernel of an immersed probe trapped in a harmonic potential. The left column shows **a)** the VACF and **b)** the memory kernel for a probe immersed in a passive bath ( $\hat{F}_0 = 0.0$ ), whereas the right column shows the **c)** VACF and **d)** memory kernel for a probe immersed in an active bath ( $\hat{F}_0 = 5.3$ ). Each bath has average density  $\rho_0 = 0.4\sigma^{-3}$  and the probe has a radius  $R_p = 3.0\sigma$ . Insets show the difference between the VACF/memory kernel of a free and trapped probe. Values of  $k$  in the legend are shown in LJ units of  $\epsilon\sigma^{-2}$ .

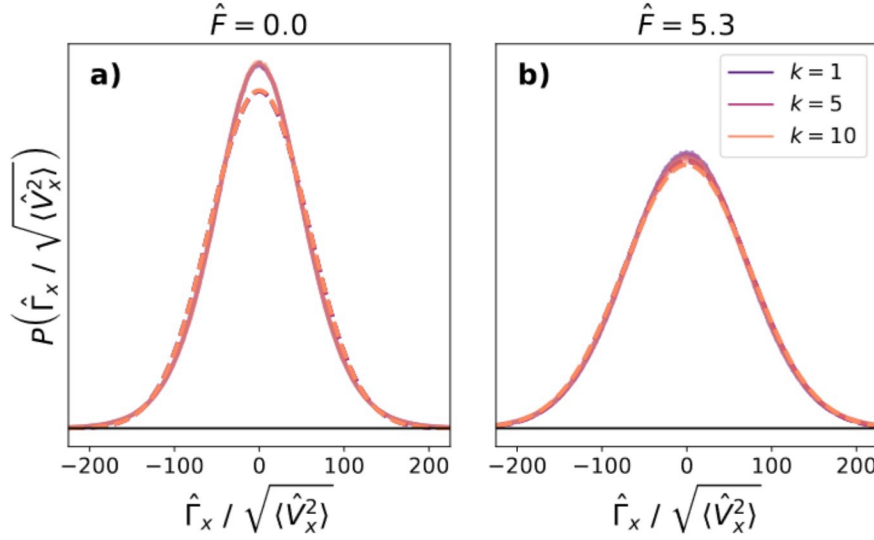


**Figure 15.4.:** Stochastic force distribution of the harmonically trapped probe in a bath of density  $\rho = 0.4\sigma^{-3}$ . **a)** The stochastic force distribution for a passive bath. **b)** The stochastic force distribution for an active bath with activity  $\hat{F}_0 = 5.3$ . The solid lines show simulation data, whereas the dotted lines show zero-centered Gaussian distributions with the same standard deviation. Values of  $k$  in the legend are shown in LJ units of  $\epsilon\sigma^{-2}$ .

distribution, which we infer results from the low density of the bath and which we also saw for the unconstrained probe (see Chapter 9.3 and Appendix C).

## 15.4 Spherical harmonics

In spite of the additional harmonic force on the probe, the density profile of the ALP bath (as calculated from Eq. (13.1)) remains identical for a trapped and a free probe (see Fig. 15.5a). Furthermore, the dipole moment,  $\Omega_1^0(r)$  (see Eq. (13.2)), remains the same whether the probe is trapped or free. This is most likely due to the fact that the forces exerted by the harmonic trap are small, i.e. within the linear response regime. Therefore, we do not see a significant alteration of the bath dynamics due to the external force on the probe, in spite of the changed behavior of the probe itself, which we see in the VACF and memory kernel in Fig. 15.3.

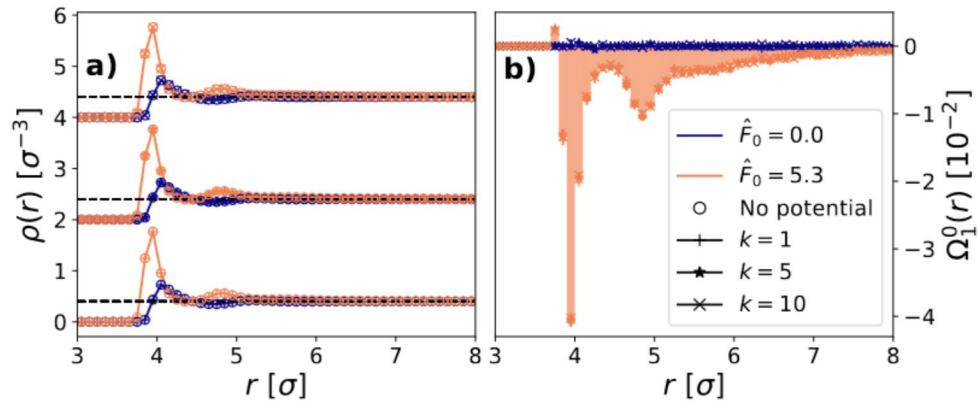


**Figure 15.5.:** **a)** Density expressed in LJ units  $\sigma^{-3}$  ( $\rho(r)$ , see Eq. (13.1)) and **b)** dipole moment ( $\Omega_1^0(r)$ , see Eq. (13.2)), surrounding a harmonically confined probe immersed in a bath with activities  $\hat{F}_0 = 0.0$  (indigo) and  $\hat{F}_0 = 5.3$  (orange). The probe has a radius  $R_p = 3.0\sigma$  and is immersed in a bath with global density  $\rho_0 = 0.4\sigma^{-3}$ . Different symbols show different harmonic trapping strengths  $k = 1\epsilon\sigma^{-3}$  (plus symbol),  $k = 5\epsilon\sigma^{-3}$  (star symbol),  $k = 10\epsilon\sigma^{-3}$  (x symbol). The results for a free probe are shown in **a)** by open circles and in **b)** by bars. For ease of visualization, in **a)** we add a vertical shift between the density profiles for different trapping strengths and show a black dashed line at the global density. In **b)**, we show a black dashed line at zero.

## Drag force

We now pull a passive probe through a bath of interacting ALPs with a constant ‘drag’ force along the x-axis:  $\mathbf{F} = F_{\text{ext}}\hat{\mathbf{x}}$  (see Fig. 16.1). Thus, the equation of motion for the probe is:

$$M\dot{\mathbf{V}}(t) = F_{\text{ext}}\hat{\mathbf{x}} - \sum_n \nabla U_{\text{WCA}}(\mathbf{R} - \mathbf{r}_n), \quad (16.1)$$

where  $M$  is the mass of the probe,  $\mathbf{V}(t)$  is its velocity, and  $U_{\text{WCA}}(\mathbf{R} - \mathbf{r}_n)$  is the WCA potential due to an ALP particle,  $n$ , at position  $\mathbf{r}_n$ . Aside from the constant external force, the immersed probe only experiences forces from interactions with the surrounding ALPs. The ALPs are described by Eq. (9.1). The ALP bath has a global density of  $0.4\sigma^{-3}$  and the probe has a radius  $R_p = 3.0\sigma$ .

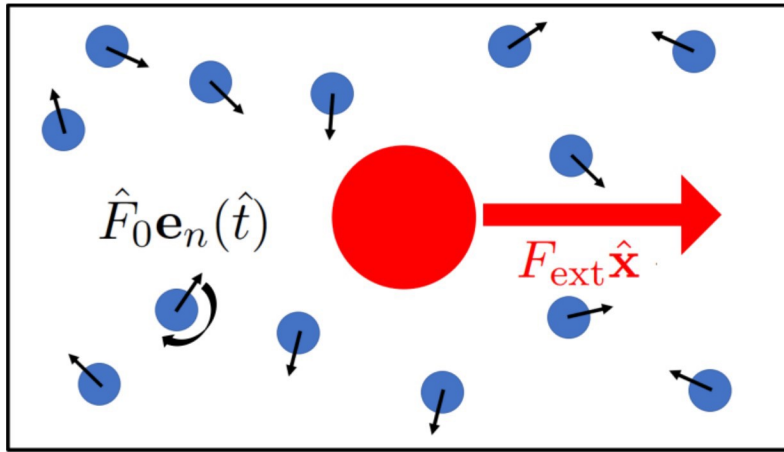


**Figure 16.1.:** System of a passive probe dragged by a constant, external force through a bath of active Langevin particles.

It has been postulated in Ref. [33], that a system with time dependent drift can be mapped onto a GLE of the form:

$$M\dot{\mathbf{V}}(t) = \mathbf{f}(t) - \int_0^t ds K(t-s)\mathbf{V}(s) + \mathbf{\Gamma}(t), \quad (16.2)$$

where  $\mathbf{f}(t)$  is the time dependent drift force. We can split this equation into two parts:

$$M\dot{\mathbf{V}}(t) = \mathbf{f}(t) - \int_0^t ds K(t-s)\bar{\mathbf{V}}(s), \quad (16.3)$$



$$M\dot{\mathbf{U}}(t) = - \int_0^t ds K(t-s)\mathbf{U}(s) + \mathbf{\Gamma}(t). \quad (16.4)$$

Here,  $\mathbf{V}(t) = \mathbf{U}(t) + \bar{\mathbf{V}}(t)$  such that  $\bar{\mathbf{V}}(t) = \langle \mathbf{V}(t) \rangle_{\text{neq}}$  is the non-equilibrium average of the velocity (i.e. the drift velocity).

Eq. (16.4) is of exactly the same form as Eq. (2.13). The only difference is that the velocity  $\mathbf{U}(t)$  is now the velocity of the probe in the *co-moving frame*. Since the equations are of the same form, Eq. (16.4) can also be transformed into a Volterra equation, which can then be inverted to find the memory kernel of the probe. Using such a mapping, the effective drift force on the probe can then be calculated with Eq. 16.3, as  $\mathbf{f}(t) = M\dot{\bar{\mathbf{V}}}(t) + \int_0^t ds K(t-s)\bar{\mathbf{V}}(s)$ .

Ref. [99] has already analyzed a probe dragged through a 2D bath of ALPs. However, they focused on drag forces well beyond the linear response regime. We now focus on drag forces which encompass the transition from being within the linear response regime to being beyond it.

## 16.1 Static mobility

The mobility of a probe dragged through a fluid is defined by Eq. (5.1), which can be written for our system as:

$$\langle V_x \rangle = \mu_{\text{Drag}} \tilde{F}_{\text{ext}}, \quad (16.5)$$

where  $\langle V_x \rangle$  is the average velocity along the x-axis and  $\mu_{\text{Drag}}$  is the mobility. Here we have used  $\tilde{F}_{\text{ext}} = \alpha F_{\text{ext}}$  as our external force because we saw in Section 15.1 that, for a probe immersed in an active bath, the external force exerted on the probe needs to be renormalized. To assess the range of the linear response regime, we define a Peclet number for the probe:  $\text{Pe} = \langle V_x \rangle / V_{\text{diff}}$ . Here, we define  $V_{\text{diff}} = D_{\text{eff}} / R_p$  based on the probe radius  $R_p = 3.0\sigma$  and the effective diffusion coefficient of an isolated ALP:  $D_{\text{eff}} = k_B T_{\text{eff}} / \gamma$ , where  $k_B T_{\text{eff}} = k_B T [1 + \hat{F}_0^2 / (3 + 6\hat{D}_R)]$  as defined in Eq. (8.6). In terms of  $\tilde{F}_{\text{ext}}$ ,  $\text{Pe} = \mu_{\text{Drag}} \tilde{F}_{\text{ext}} / V_{\text{diff}}$  (see Appendix J).

We graph the force dependent mobility ( $\mu_{\text{Drag}}(\tilde{F}_{\text{ext}}) = \langle V_x \rangle / \tilde{F}_{\text{ext}}$ ) as a function of the Peclet number in Fig. 16.2a). We expect that  $\mu_{\text{Drag}}(\tilde{F}_{\text{ext}})$  is constant within the linear response regime for a probe immersed in a passive bath. We also find this to be the case for a probe immersed in an active bath. However, for a probe immersed in an active bath, the linear response regime is less clear because of large fluctuations in  $\mu_{\text{Drag}}(\tilde{F}_{\text{ext}})$  for low values of Pe, as shown in Fig. 16.2. We infer that

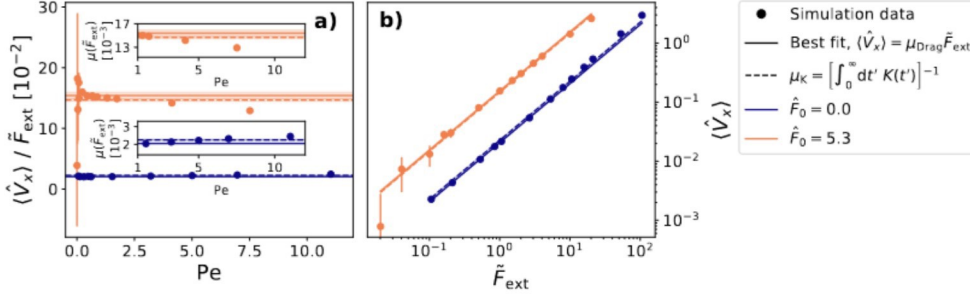


**Figure 16.2.:** Probe mobility and Peclet number. **a)** Force dependent mobility as a function of Peclet number. Insets zoom in on the mobility beyond the linear response regime. **b)** Average velocity along the x-axis,  $\langle V_x \rangle$ , as a function of the renormalized external drag force,  $\tilde{F}_{\text{ext}}$ . The circles show the simulation data and the solid lines show the best fit for these data, the slope of which is  $\mu_{\text{Drag}}$ . The dashed lines have a slope corresponding to  $\mu_K$ . Each bath has average density  $\rho_0 = 0.4\sigma^{-3}$  and the probe has a radius  $R_p = 3.0\sigma$ .

these fluctuations result from the fact that the activity of the bath induces larger variations in the probe velocity.

Linear response generally holds for Peclet numbers up to  $Pe \sim 1$ , which agrees with what we find in Fig. 16.2a) for both a probe immersed in a passive and an active bath. We therefore consider Peclet numbers  $Pe < 1$  to be within the linear response regime. We would like to note that, due to the enhanced diffusion of the active bath particles in comparison to the passive bath particles, equivalent Peclet numbers for a probe in an active and a passive bath correspond to different external drag forces (see Appendix J). Much larger drag forces are required to achieve the same Peclet number for an active bath in comparison with a passive bath.

In Fig. 16.2b), we now graph  $\langle V_x \rangle$  as a function of  $\tilde{F}_{\text{ext}}$  to determine  $\mu_{\text{Drag}}$  within the linear response regime using Eq. (16.5). We extract a mobility  $\mu_{\text{Drag}} = 0.02057 \pm 0.00006$  for a probe immersed in a passive bath ( $\hat{F}_0 = 0.0$ ) with a density  $\rho = 0.4\sigma^{-3}$ . For a probe in an active bath ( $\hat{F}_0 = 5.3$ ) of density  $\rho = 0.4\sigma^{-3}$ , we extract a mobility of  $\mu_{\text{Drag}} = 0.154 \pm 0.006$ . Comparing these values, we see that increasing the activity of the bath also increases the mobility of the probe particle.

Eq. (16.5) is not the only way to define mobility. The mobility can also be defined by the memory kernel of a free probe through the equation:

$$\mu_K = \left[ \int_0^\infty dt' K(t') \right]^{-1}. \quad (16.6)$$

Using the memory kernels calculated in Section 9.2, we calculate  $\mu_K = 0.0226 \pm 0.0003$  for a probe in a passive bath of density  $\rho = 0.4\sigma^{-3}$  and  $\mu_K = 0.147 \pm 0.002$  for a probe in an active bath of density  $\rho = 0.4\sigma^{-3}$  with  $\hat{F}_0 = 5.3$ . As expected, for the

probe dragged through a passive bath, the mobility calculated from Eq. (16.6) agrees well with that calculated from Eq. (16.5). The slight discrepancy between values is most likely due to the reconstruction of the memory, which becomes less accurate at longer times. For an active bath the two methods of calculating the mobility also agree. However, we would like to emphasize that using the renormalized external force to define  $\mu_{\text{Drag}}(\tilde{F}_{\text{ext}})$  is essential to this agreement.

## 16.2 Beyond linear response

The insets of Fig. 16.2a) show us that the behavior beyond the linear response regime is qualitatively different for a probe immersed in an active vs. a passive bath. As mentioned in Chapter 5, both ‘thinning’ (increased mobility) [48, 49, 50, 51, 52] and ‘thickening’ (decreased mobility) [33, 50, 52, 53, 54] behavior have been observed for different systems beyond the linear response regime. We find that (for our particular system), whereas a probe dragged through a passive bath exhibits thinning behavior, a probe dragged through a bath of ALPs exhibits thickening behavior. Due to these opposite behaviors, the values of  $\mu_{\text{Drag}}(\tilde{F}_{\text{ext}})$  for a passive and an active bath at the same Peclet number approach each other beyond the linear response regime.

## 16.3 Velocity autocorrelation function and memory kernel

Having looked at the active microrheological properties of the active bath, we turn to the dynamic properties of the dragged probe: namely, the VACF and the memory kernel. We map the dynamics of our system onto Eq. (16.2). We examine the VACF in the co-moving frame because, for a probe dragged through a passive bath, this should be the same for all drag forces within the linear response regime [33]. We would like to evaluate the universality of the co-moving VACF for a probe dragged through an active bath as well.

As we would expect, within the linear response regime ( $\text{Pe} < 1$ ), the VACF and memory kernel are isotropic and independent of  $\tilde{F}_{\text{ext}}$  for a probe dragged through a passive bath. We additionally find that the VACF and memory kernel are isotropic and independent of  $\tilde{F}_{\text{ext}}$  for a probe dragged through an active bath (Figs. 16.3 and 16.4).

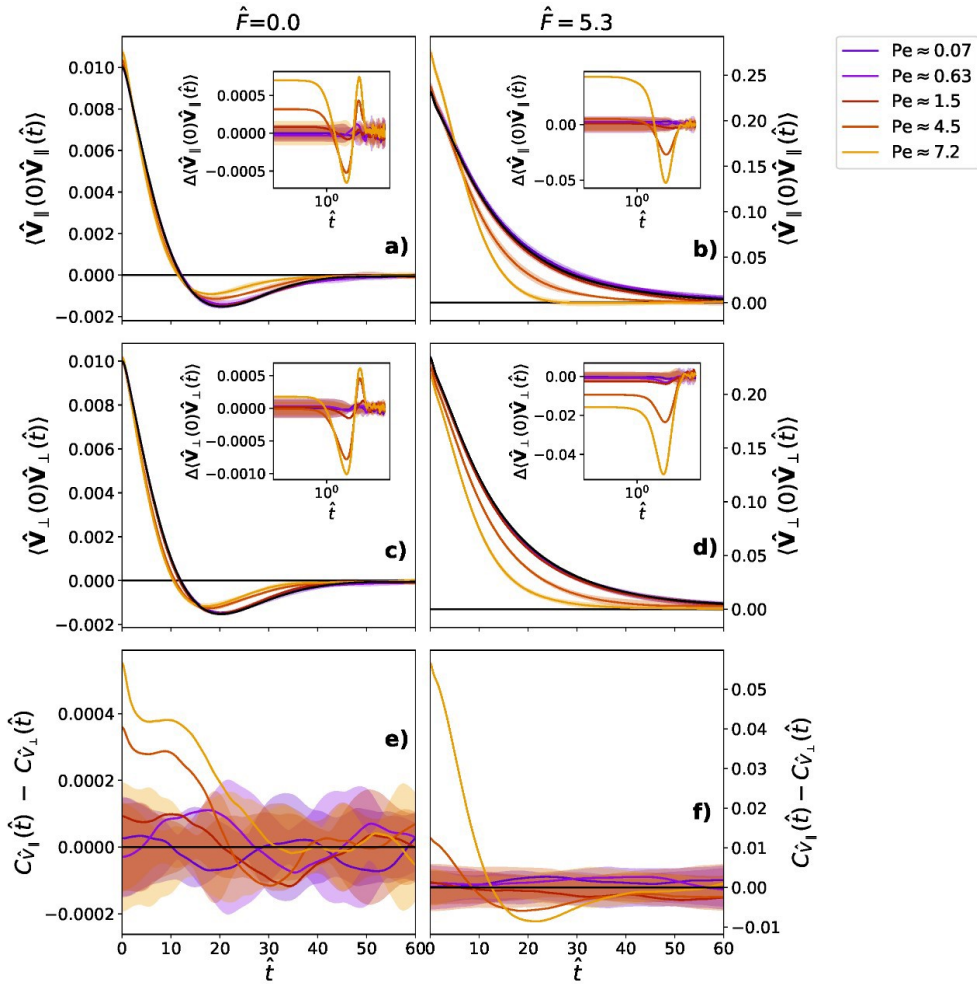


**Figure 16.3.:** Velocity autocorrelation function (VACF) of the dragged, immersed probe. Each bath has global density  $\rho_0 = 0.4\sigma^{-3}$  and the probe has a radius  $R_p = 3.0\sigma$ . **a,b)** The top row shows the component of the VACF which is parallel to the drag force, whereas **c,d)** the middle row shows the perpendicular component. **e,f)** The bottom row shows the difference between parallel and perpendicular components of the memory kernel. **a,c,e)** The left column is for a passive bath, whereas **b,d,f)** the right column is for an active bath ( $\hat{F}_0 = 5.3$ ). The black curves in plots **a-d)** show the VACF for a probe which is not dragged and insets show the difference between the VACF of a free and a dragged probe. We show a black line at zero in each graph for ease of visualization.

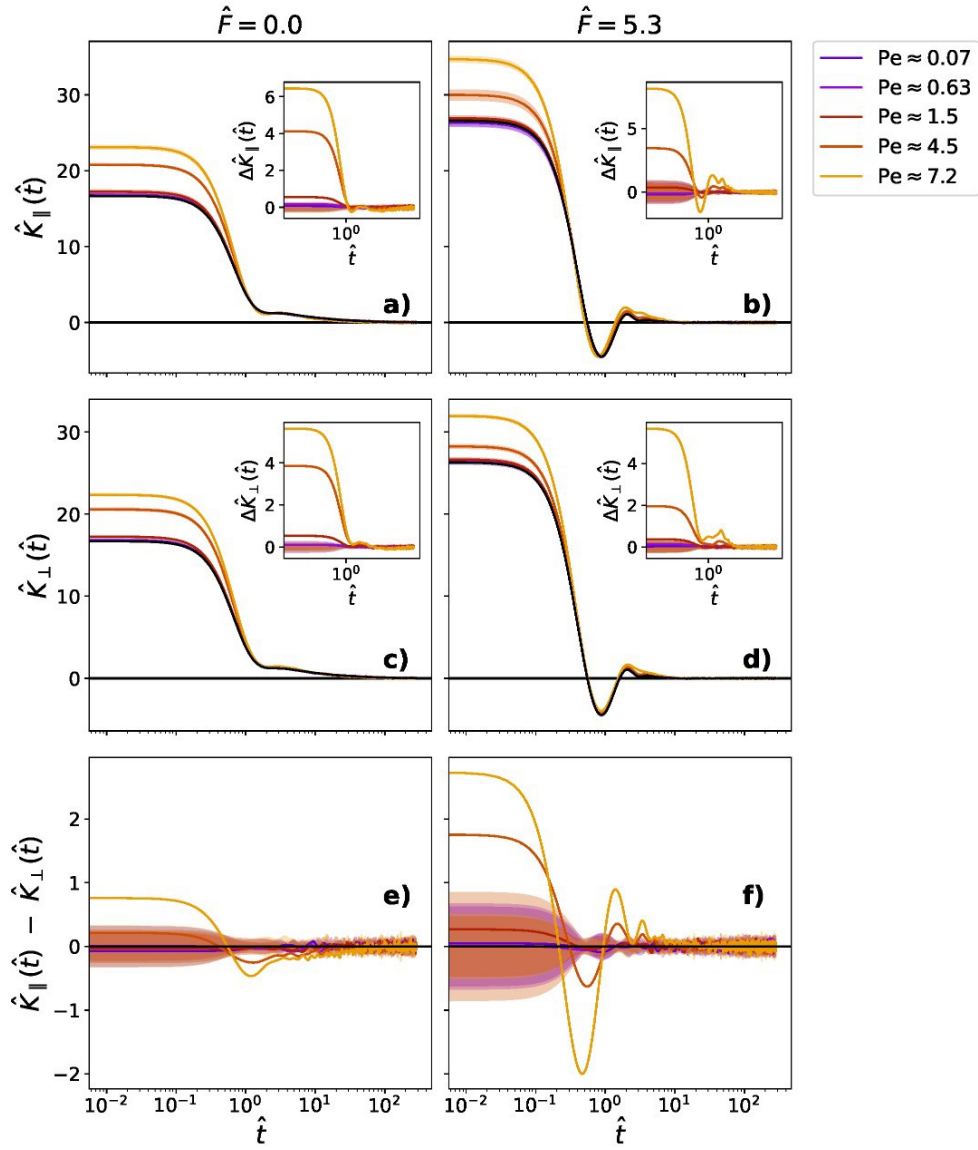


**Figure 16.4.:** Memory kernel of the dragged, immersed probe. Each bath has global density  $\rho_0 = 0.4\sigma^{-3}$  and the probe has a radius  $R_p = 3.0\sigma$ . **a,b)** The top row shows the component of the memory kernel which is parallel to the drag force, whereas **c,d)** the middle row shows the perpendicular component. **e,f)** The bottom row shows the difference between parallel and perpendicular components of the memory kernel. **a,c,e)** The left column is for a passive bath, whereas **b,d,f)** the right column is for an active bath ( $\hat{F}_0 = 5.3$ ). The black curves in plots **a-d)** show the memory kernel for a probe which is not dragged and insets show the difference between the memory kernel of a free and a dragged probe. We show a black line at zero in each graph for ease of visualization.

Beyond the linear response regime, however, the VACF and memory kernel are neither isotropic (see Figs. 16.3e,f) and 16.4e,f)) nor independent of  $\tilde{F}_{\text{ext}}$  for both passive and active systems. In both the case of a passive and active bath, a drag force beyond the linear response regime causes the VACF to decay more rapidly in both its parallel and perpendicular components. The behavior of the memory kernel is primarily affected at short times, during which its value is greater than that of a free probe. This is, again, true for both a probe dragged through a passive and an active bath.

However, the other aspects of the VACF/memory kernel form differ based on whether the bath is passive or active. In a passive bath, we see that the dragged probe acquires an increased local kinetic temperature in both its parallel and perpendicular components. In an active bath, on the other hand, the dragged probe only acquires an increased local kinetic temperature in its parallel component. In fact, in its perpendicular component, the probe dragged through an active bath actually experiences a decrease in local kinetic temperature.

## 16.4 Stochastic force distribution

Once we have determined the memory kernel of the probe, it is straightforward to determine the stochastic force ( $\Gamma(t)$  in Eq. (16.2)) using Eq. 2.19, the probability distribution of which we show in Fig. 16.5. In Fig. 16.5, we see that in both the case of a passive and an active bath, for low Peclet numbers (within the linear response regime), the stochastic force distribution calculated from simulation data (solid lines) approximately matches a zero-centered Gaussian with the same standard deviation (dashed lines). The only deviations from the zero-centered Gaussian are an enhanced peak in the distribution, which we infer results from the low density of the bath (see Section 9.3 and Appendix C).

However, at higher drag forces, the distribution calculated from simulation data develops an asymmetry in both components parallel and perpendicular to the drag force. This asymmetry has already been seen for a passive bath in Ref. [33]; we now show that it also occurs for an active bath, though the magnitude of the asymmetry appears to be slightly lower in the active case. We infer that the lower asymmetry in the active case stems from the already enhanced fluctuations due to the bath activity.

The asymmetry takes the form of a long tail in the negative forces of the distribution. This long tail occurs because, outside of the linear response regime, bath particles

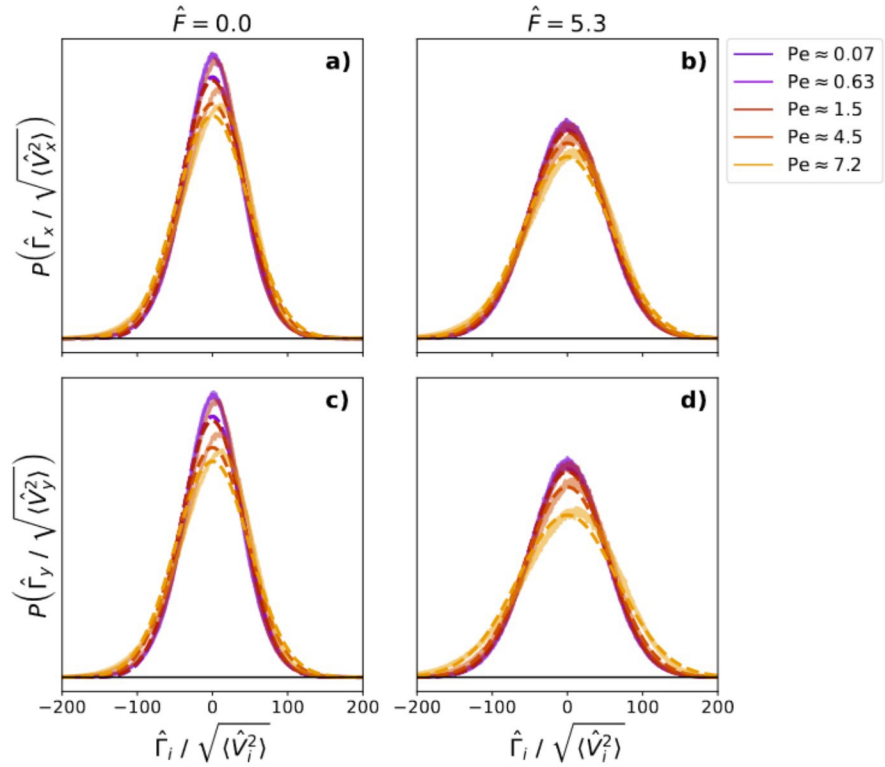


**Figure 16.5.:** Stochastic force distribution of the dragged, immersed probe in a bath of density  $\rho = 0.4\sigma^{-3}$ . **a,b)** The top row shows the component of the stochastic force which is parallel to the drag force, whereas **c,d)** the bottom row shows one of the perpendicular components (the other perpendicular component is identical). **a,c)** The left column is for a passive bath, whereas **b,d)** the right column is for an active bath ( $\hat{F}_0 = 5.3$ ). The solid lines show simulation data, whereas the dotted lines show zero-centered Gaussian distributions with the same standard deviation. We show a black horizontal line at zero for ease of visualization.

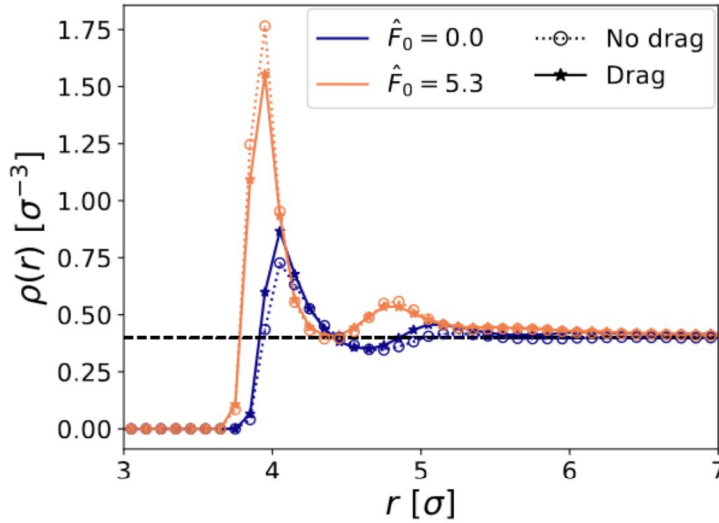


**Figure 16.6.:** Density in LJ units  $\sigma^{-3}$  ( $\rho(r)$ , see Eq. (13.1)) of the immersed probe in baths with activities  $\hat{F}_0 = 0.0$  (indigo) and  $\hat{F}_0 = 5.3$  (orange). Open circles with dotted lines show  $\rho(r)$  for a probe which is not dragged, whereas solid lines with stars show  $\rho(r)$  for a probe dragged with  $\text{Pe} \approx 7.2$ . The probe has a radius  $R_p = 3.0\sigma$ . For ease of visualization, we show a black dashed line at the global density,  $\rho_0 = 0.4\sigma^{-3}$ .

in the vicinity of the probe do not necessarily travel at the same relative velocity as the probe [129]. This leads some bath particles to ‘crash,’ with relatively high forces, into the probe, promoting the long tail. Because the average of the stochastic force distribution remains zero, the distribution also exhibits a slightly enhanced probability for positive forces. The distribution outside the linear response regime can be described by a split normal Gaussian [33].

## 16.5 Spherical harmonics

We infer that the behavior of the probe mobility beyond the linear response regime results primarily from the different number of contacts experienced by a dragged probe. We see in Fig. 16.6 that the density profile (calculated from Eq. (13.1)) for both a passive and active bath differs for a free vs. a dragged particle. However, whereas a probe dragged through a passive bath has a higher number of contacts in its immediate vicinity, a probe dragged through an active bath has a lower number of contacts. The different behavior of the contact number beyond the linear response regime for a passive vs. active bath hints at the reasoning for thinning vs. thickening behavior in each respective case.



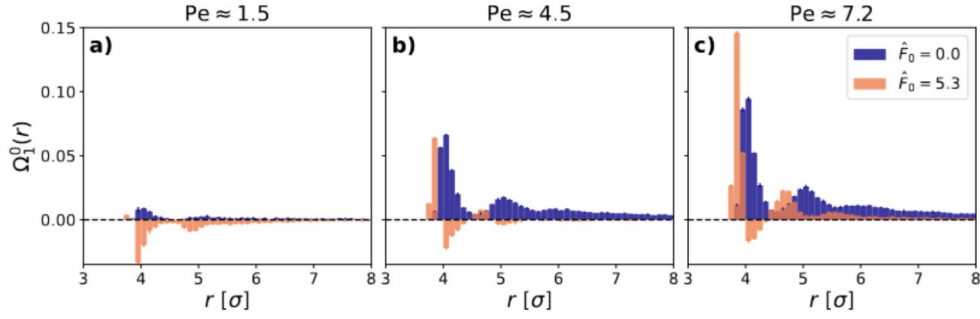


**Figure 16.7.:** Dipole moment ( $\Omega_1^0(r)$ , see Eq. (13.2)) of the bath as a function of distance from the center of the immersed probe ( $r$ ) for a probe dragged with a Peclet number **a)**  $Pe \approx 1.5$ , **b)**  $Pe \approx 4.5$ , and **c)**  $Pe \approx 7.2$  for both a passive ( $\hat{F}_0 = 0.0$ , indigo) and an active ( $\hat{F}_0 = 5.3$ , orange) bath. Each bath has average density  $\rho_0 = 0.4\sigma^{-3}$  and the probe has a radius  $R_p = 3.0\sigma$ . For ease of visualization we show a black dashed line at 0.

It has previously been shown that a probe dragged with sufficient force through a passive bath experiences an increased density of particles in front of it [33, 52]. By examining the dipole moment in the vicinity of the probe (see Fig. 16.7, calculated from Eq. (13.2)), we verify this buildup of particles in front of a probe dragged through a passive bath with  $Pe > 1$ .

A similar frontal buildup is exhibited by a probe dragged through an active bath with  $Pe \approx 7.2$ . However, for a lower Peclet number (e.g.  $Pe \approx 1.5$  and  $Pe \approx 4.5$ ), we do not see such a buildup in an active bath. In fact, in spite of the drag force, we still see a buildup of ALPs *behind* the probe for  $Pe \lesssim 1.5$ .

We reason this qualitative difference in the bath behavior at the probe interface following the arguments of Ref. [99]. For small Peclet numbers, the speed of the ALPs is greater than that of the dragged probe. Thus, the ALPs are able to accumulate behind the probe and push, as was the case for a probe without an external drag force. Consequently, we still see a negative dipole moment in the active bath for  $Pe \approx 1.5$  in Fig. 16.7a). For intermediate Peclet numbers, the dragged probe and the ALPs move at similar speeds. Therefore, the dipole moment of the active bath goes to zero, which we see happening for  $Pe \approx 4.5$  in Fig. 16.7b). Although for this value of  $Pe$  the dipole moment is not entirely zero, we can see that its magnitude and range are smaller. For large Peclet numbers, ALPs can no longer catch up to the probe and, consequently, the active bath acquires a positive dipole moment in the vicinity of the probe, as seen for  $Pe \approx 7.2$  in Fig. 16.7c).

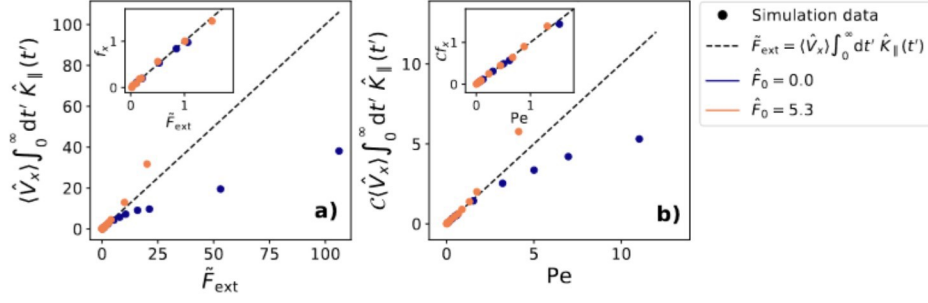


**Figure 16.8.:** Effective drift force ( $f_x$ ) determined by our coarse-grained model (see Eq. (16.7)) **a)** as a function of the applied external force ( $\tilde{F}_{\text{ext}}$ ), **b)** as a function of the Peclet number. In **b)**,  $f_x$  has been rescaled by  $C = \mu_{\text{Drag}}/V_{\text{diff}}$  because  $\text{Pe} = C\tilde{F}_{\text{ext}}$  (see Appendix J). The dashed, black line in each plot shows  $f_x = \tilde{F}_{\text{ext}}$ , what we would expect for a good coarse-grained mapping. Each bath has average density  $\rho_0 = 0.4\sigma^{-3}$  and the probe has a radius  $R_p = 3.0\sigma$ .

## 16.6 Effective drift force

To understand the external force in our GLE mapping, we evaluate the effective drift force in our coarse-grained mapping. In our particular system, the effective drift force is:

$$f_x = \langle V_x \rangle \int_0^\infty dt' K_\parallel(t'). \quad (16.7)$$

We now compare the value of  $f_x$ , which we find from our coarse-grained model, to the renormalized, applied external force ( $\tilde{F}_{\text{ext}}$ ) as shown in Fig. 16.8. In the case that our mapping is successful, we expect that  $f_x = \tilde{F}_{\text{ext}}$ .

Within the linear response regime, we find that, for both passive and active cases, this relation holds (see insets of Figs. 16.8a) and b)). Therefore, with the renormalized drag force, our coarse-grained model works.

Beyond the linear response regime, however, the relation breaks down both in the case of a passive and an active bath (see Figs. 16.8a) and b)). In the case of a passive bath, our coarse-grained model underestimates the value of  $\tilde{F}_{\text{ext}}$ . In the case of an active bath, our coarse-grained model overestimates the value of  $\tilde{F}_{\text{ext}}$ . We attribute the difference in the way the relation breaks down (underestimation vs. overestimation) for a passive vs. active system to the opposite behavior of the mobility beyond linear response (thinning vs. thickening).

## Part IV: conclusions and outlook

We have shown that the system of a probe immersed in an active bath and subject to an external force can be mapped onto a physically meaningful GLE which satisfies the 2FDT. For such a mapping, the dissipative and stochastic forces should be defined using an inverse Volterra equation. Due to the activity of the bath, the external force in such an equation is not equal to the physical external force, but rather a renormalized external force. The necessity of a renormalized force explains citations of violations or necessary modifications to FDTs in previous research works [26, 29, 127]. The ability to map this non-equilibrium system onto a GLE which satisfies the 2FDT enables the use of many recently developed coarse-grained methods which rely on its fulfillment [130, 131, 132].

However, the ability to map the probe's behavior onto a physically meaningful GLE breaks down for external forces beyond the linear response regime. Consequently, developing coarse-grained methods for external forces beyond the linear response regime will be an important area for future research.

Additionally, it has been shown that a harmonically confined active particle exhibits different behavior from a harmonically confined passive particle [133, 134, 135]. Namely, the radial probability distribution of the active particle exhibits two 'phases' which depend on the particle activity and the trap strength: a 'passive' phase described by a Boltzmann-like distribution around the trap center, and an 'active' phase described by a non-Boltzmann distribution which is peaked away from the trap center [135]. Given the shared behaviors of a probe immersed in an active bath with an active particle itself [28, 58, 68], it would be interesting to determine if there exists an 'active' phase probability distribution for a probe immersed in an active bath for other values of activity and constraint. If such an 'active' phase exists, a GLE which satisfies the 2FDT would likely be insufficient to describe it, and would therefore also require further research to develop a coarse-grained model.

## Conclusions and outlook

A passive probe particle immersed in an active bath behaves differently from a passive probe particle immersed in a passive bath. We have shown that, in fact, a probe immersed in an active bath acquires a number of properties reminiscent of an active particle itself, such as slowly decaying velocity correlations, an enhanced kinetic temperature, and a partially negative memory kernel. The apparent mechanism for these active-particle-like behaviors is an accumulation of active particles behind the probe (with respect to its instantaneous velocity), which push the probe at sufficiently high activities.

Although the probe does exhibit these active-particle-like behaviors, unlike an active particle, it does not exhibit a non-Gaussian linear velocity distribution. Non-equilibrium signatures of a probe immersed in an active bath prove difficult to detect. As one way to detect a non-equilibrium signature from only the trajectory of the probe, we propose to slightly perturb the probe, which will reveal a violation of the first fluctuation dissipation theorem if the bath is not at equilibrium. Alternatively, we propose to examine the trajectories of multiple probes of different sizes, which will acquire different kinetic temperatures if the bath is active. We found the kinetic temperature to behave non-monotonically with respect to the probe radius; however, an explanation for this behavior remains unclear and should be addressed in future research.

Despite the probe's inherently non-equilibrium dynamics due to the activity of the bath, when subject to an external force, we found that the probe dynamics can still be mapped onto a physically meaningful generalized Langevin equation which satisfies the second fluctuation dissipation theorem. In this case, the external force in the effective generalized Langevin equation is not equal to the physical external force, but rather a renormalized external force. The ability to map this non-equilibrium system onto such a generalized Langevin equation enables the use of previously established coarse-grained methods; however, it also raises the question as to when such a coarse-grained model breaks down. We have already seen one such instance: when the external force on the probe is beyond the linear response regime.

# Calculation of an isolated ALP VACF

We know that the VACF can be calculated as:

$$\langle \hat{v}(\hat{t})\hat{v}(\hat{t}') \rangle = \frac{1}{\mathcal{T}} \int_0^{\mathcal{T}} ds \hat{v}(\hat{t} + s) \hat{v}(\hat{t}' + s), \quad (\text{A.1})$$

in the limit  $\mathcal{T} \rightarrow \infty$ . We additionally know that, in rescaled quantities  $\hat{F}_0$  and  $\hat{D}_R$ , the equation for the velocity of a non-interacting ALP is:

$$\hat{v}(\hat{t}) = \hat{v}(0) \exp(-\hat{t}) + \hat{F}_0 \int_0^{\hat{t}} ds \exp(-(\hat{t} - s)) e(s) + \int_0^{\hat{t}} ds \exp(-(\hat{t} - s)) \hat{\xi}(s) \quad (\text{A.2})$$

We now assume that the initial time is in the infinite past, as done in Ref. [9], so that the instantaneous velocity is only determined by the noise terms in Eq. (A.2). Under this assumption, our ALP instantaneous velocity is:

$$\hat{v}(\hat{t}) = \hat{F}_0 \int_0^{\hat{t}} du \exp(-u) e(\hat{t} - u) + \int_0^{\hat{t}} du' \exp(-u') \hat{\xi}(\hat{t} - u'), \quad (\text{A.3})$$

where we have slightly rearranged the time integral for convenience. Following Eq. (A.1), we then multiply this velocity by the velocity at some other time ( $\hat{v}(\hat{t}')$ ), average over the noise, and integrate over the time interval  $\mathcal{T}$  in the limit  $\mathcal{T} \rightarrow \infty$ . From Eqs. (2.2), (6.2), and (6.3) we know that  $\langle e(\hat{t})\hat{\xi}(\hat{t}') \rangle = 0$ ; therefore, we can eliminate the cross terms. We also know that  $\langle e(\hat{t})e(\hat{t}') \rangle = \exp(-2\hat{D}_R|\hat{t} - \hat{t}'|)$  and  $\langle \hat{\xi}(\hat{t})\hat{\xi}(\hat{t}') \rangle = 2\delta(\hat{t} - \hat{t}')$ . Therefore, performing all the above integrations, we recover:

$$\langle \hat{v}(\hat{t})\hat{v}(\hat{t}') \rangle = 3 \exp(-|\hat{t} - \hat{t}'|) + \frac{\hat{F}_0^2}{1 - 4\hat{D}_R^2} \left( \exp(-2\hat{D}_R|\hat{t} - \hat{t}'|) - 2\hat{D}_R \exp(-|\hat{t} - \hat{t}'|) \right), \quad (\text{A.4})$$

given as Eq. (8.2) in Chapter 8.

## Calculation of $P(\hat{\mathbf{v}})$

### B.1 From simulation data

To calculate  $P(\hat{\mathbf{v}})$  from our simulation data, we calculate the absolute velocity,  $|\mathbf{v}|$ , of the particle for each time step. We then assign this value of  $|\mathbf{v}|$  to an appropriate bin, each of length  $dv$ , to find the absolute velocity distribution  $N[|\mathbf{v}|]$ . We divide each of these bins by its true volume,  $\delta V = \frac{4}{3}\pi\left((v + \frac{dv}{2})^3 - (v - \frac{dv}{2})^3\right)$ , and scale the distribution by a factor of  $\sqrt{m/k_B T}$  to find  $P(\hat{\mathbf{v}})$ . The distribution calculated from simulation data is normalized such that  $\sum_{|\hat{\mathbf{v}}|} P(\hat{\mathbf{v}})\delta V = 1$ . Theoretical distributions of  $P(\hat{\mathbf{v}})$  are normalized such that  $\int_{\infty} d\hat{v} 4\pi\hat{v}^2 P(\hat{\mathbf{v}}) = 1$ .

### B.2 From the Fokker-Planck equation

The stochastic equations of motion for an isolated ALP (Eqs. (8.1) in Chapter 8) are equivalent to a Fokker-Planck equation for the time-dependent distribution function  $P(\hat{\mathbf{v}}, \mathbf{e}, \hat{t})$ :

$$\frac{\partial}{\partial \hat{t}} P(\hat{\mathbf{v}}, \mathbf{e}, \hat{t}) = -\nabla_{\hat{\mathbf{v}}} (\hat{\mathbf{v}} + \nabla_{\hat{\mathbf{v}}} - \hat{F}_0 \mathbf{e}) P(\hat{\mathbf{v}}, \mathbf{e}, \hat{t}) - \hat{D}_R \Delta_{\mathbf{e}} P(\hat{\mathbf{v}}, \mathbf{e}, \hat{t}), \quad (\text{B.1})$$

where  $\Delta_{\mathbf{e}}$  denotes the angular part of the Laplace operator. The stationary solution of this equation ( $P_s(\hat{\mathbf{v}}, \mathbf{e})$ ) solves,

$$0 = \left[ \nabla_{\hat{\mathbf{v}}} (\hat{\mathbf{v}} + \nabla_{\hat{\mathbf{v}}} - \hat{F}_0 \mathbf{e}) + \hat{D}_R \Delta_{\mathbf{e}} \right] P_s(\hat{\mathbf{v}}, \mathbf{e}). \quad (\text{B.2})$$

In the limit  $\hat{D}_R \rightarrow 0$ , Eq. (B.2) is solved by

$$P_s(\hat{\mathbf{v}}, \mathbf{e}) = \mathcal{N} \exp\left(-\frac{\hat{\mathbf{v}}^2}{2} + \hat{F}_0 (\mathbf{e} \cdot \hat{\mathbf{v}})\right), \quad (\text{B.3})$$

where  $\mathcal{N} = \frac{1}{2\pi^{3/2}\sqrt{2}}e^{-\hat{F}_0^2/2}$  is the normalization constant. Taking the average over all orientations  $\mathbf{e}$  gives the velocity distribution at  $\hat{D}_R \rightarrow 0$ :

$$P(\hat{\mathbf{v}}) = \int d^2\mathbf{e} \mathbf{P}_S(\hat{\mathbf{v}}, \mathbf{e}) \propto e^{-\hat{\mathbf{v}}^2/2} \frac{1}{\hat{F}_0|\hat{\mathbf{v}}|} \sinh(\hat{F}_0|\hat{\mathbf{v}}|), \quad (\text{B.4})$$

which is quoted as Eq. (8.7) in Chapter 8. The mean squared velocity calculated from this distribution is given by  $\langle \hat{\mathbf{v}}^2 \rangle = 3 + \hat{F}_0^2$ , which has the same functional form as Eq. (8.5) with  $\hat{F}_0/\sqrt{1 + 2\hat{D}_R}$  replaced by  $\hat{F}_0$ . Based on this observation, we conjecture that  $P(\hat{\mathbf{v}})$  at finite  $\hat{D}_R$  has the same functional form as Eq. (B.4) with  $\hat{F}_0$  replaced by  $\hat{F}_0/\sqrt{1 + 2\hat{D}_R}$ . This results in Eq. 8.8 of Chapter 8.

## Stochastic force distribution relative entropy

In Section 9.3, we saw qualitatively that the stochastic force distribution of a passive probe remains Gaussian even when immersed in an active bath. To quantify this, we calculate the relative entropy between the simulation data and zero-centered Gaussian distributions with the same standard deviation (see Eq. (8.9)). From Fig. C.1, we see that there are deviations from a Gaussian distribution at low densities. However, these deviations occur even in a passive bath. In fact, as the activity of the bath increases, the deviations from a Gaussian distribution at low densities actually decrease. Thus, we attribute these deviations to low density effects rather than activity effects.

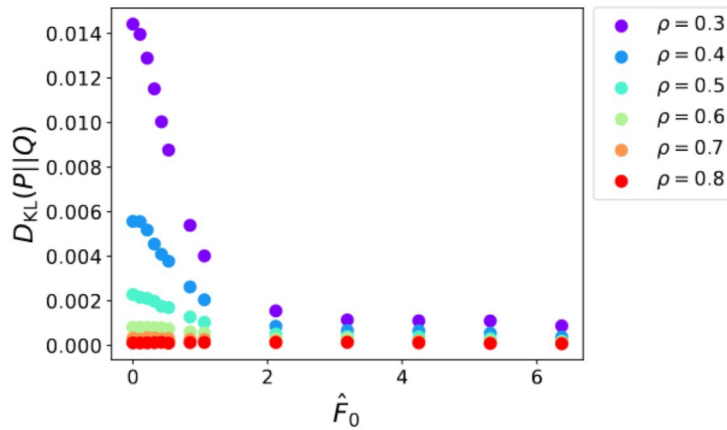


**Figure C.1.:** Relative entropy (Eq. (8.9)) between the stochastic force distribution calculated from simulation data and a Gaussian distribution with the same standard deviation. Densities in the legend are expressed in LJ units of  $\sigma^{-3}$ .



## Test of linear response regime for perturbation force

We would like to check that the perturbation force we use to test the 1FDT in Section 9.4 is within the linear response regime for both a probe immersed in a passive and an active bath. To do this, we test perturbation forces ( $\alpha(t) = MV_0\delta(t)$ ) for different values of  $V_0$ :  $V_0 = 0.2, 0.4,$  and  $0.5$ . For perturbation forces within the linear response regime, we expect that  $\delta\langle\hat{V}(t)\rangle/\hat{V}_0$  collapses.

Indeed, this is what we see for all our tested values of the perturbation force for both a probe immersed in a passive bath (Fig. D.1a)) and an active bath (Fig. D.1b)). Furthermore, we note that, in the case of a passive bath,  $\delta\langle\hat{V}(t)\rangle/\hat{V}_0$  always matches  $C_{\hat{V}}^{SS}(t)/C_{\hat{V}}^{SS}(0)$  curve meaning that the 1FDT is fulfilled as we would expect for this equilibrium system. This is not the case for a probe immersed in an active bath, in which case the 1FDT is not fulfilled, as we saw in Section 9.4.

We note that perturbation forces with  $V_0 = 0.2$  and  $0.4$  have fewer statistics than that with  $V_0 = 0.5$ , leading to deviations in  $\delta\langle\hat{V}(t)\rangle/\hat{V}_0$  at longer times. However, it is already clear that these curves collapse based on the short time dynamics of  $\delta\langle\hat{V}(t)\rangle/\hat{V}_0$ .

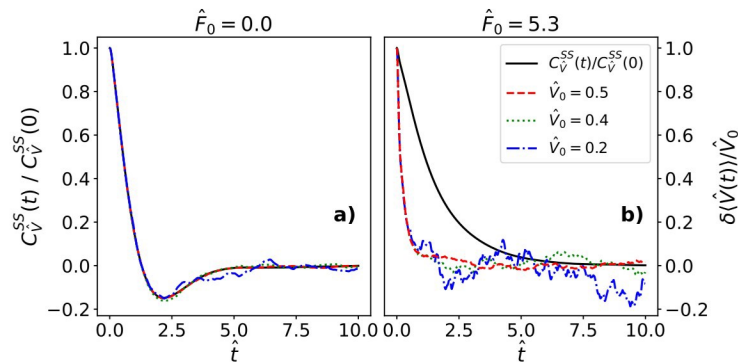


**Figure D.1.:** Test of linear response for the perturbation force applied in Chapter 9.4.  $\delta\langle\hat{V}(t)\rangle/\hat{V}_0$  collapses for the different values of the perturbation force tested —  $\alpha(t) = MV_0\delta(t)$ , with  $V_0 = 0.2, 0.4,$  and  $0.5$  — confirming that the perturbation force is within the linear response regime for both **a)** a passive and **b)** an active bath of density  $\rho = 0.4\sigma^{-3}$ .

# 1FDT for an isolated ALP

In Section 9.4, we tested the 1FDT for a passive probe immersed in an active bath and found that it is violated. We now test the 1FDT for an isolated ALP. We find that the 1FDT is also violated for an isolated ALP (see Fig. E.1). Furthermore, the curves in Fig. E.1 are qualitatively very similar to those in Fig. 9.8. The similarity of the curves in these figures highlights the similarities between the dynamics of a passive probe immersed in an active bath and those of an isolated ALP.

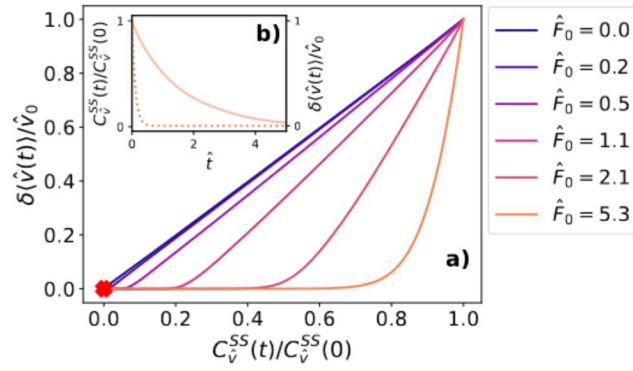


**Figure E.1.:** Test of the 1FDT for an isolated ALP using a perturbation force  $\alpha(t) = MV_0\delta(t)$  with  $\hat{V}_0 = 0.5$ . **a)** Response function of the ALP velocity versus its normalized VACF. The red 'x' shows the point (0,0) to which both functions decay in the long-time limit. If the 1FDT is fulfilled, the curve is a straight line along the diagonal. **b)** Response function of the probe velocity (dotted line) and normalized VACF (solid line) as a function of time for  $\hat{F}_0 = 5.3$ .

## Velocity distribution for probes of different sizes

In Figs. F.1a-e), we plot the velocity distributions —  $P(\hat{v})$ , calculated as detailed in Appendix B.1 — of the different sized probes listed in Table III.1 in a bath of density  $\rho = 0.8\sigma^{-3}$ . We also show zero-centered Gaussian distributions with the same standard deviation as the simulation data. At least qualitatively, the Gaussian distributions seem to match the simulation data very well.

In order to gather a more quantitative understanding of the differences between the distribution from simulation data and a zero-centered Gaussian with the same standard deviation, we plot the relative entropy (Eq. (8.9)) between these two distributions in Figs. F.1a'-e'). From Figs. F.1a'-e'), we see that the deviations from a Gaussian distribution are generally very small. However, we do see some relatively large deviations for small probes ( $R_p \leq 2.0\sigma$ ) immersed in active baths of low density ( $\rho = 0.3\sigma^{-3}$ ) in Figs. F.1a'-c'). We attribute these deviations to poorer statistics for such systems: because the bath has a low density, the probe experiences fewer collisions with bath particles, which is only exacerbated by the small size of the probe. Therefore, we conclude that the deviations from a Gaussian distribution are due more to the less robust statistics in these systems than a fundamental lack of Gaussianity in the probe velocity distribution.

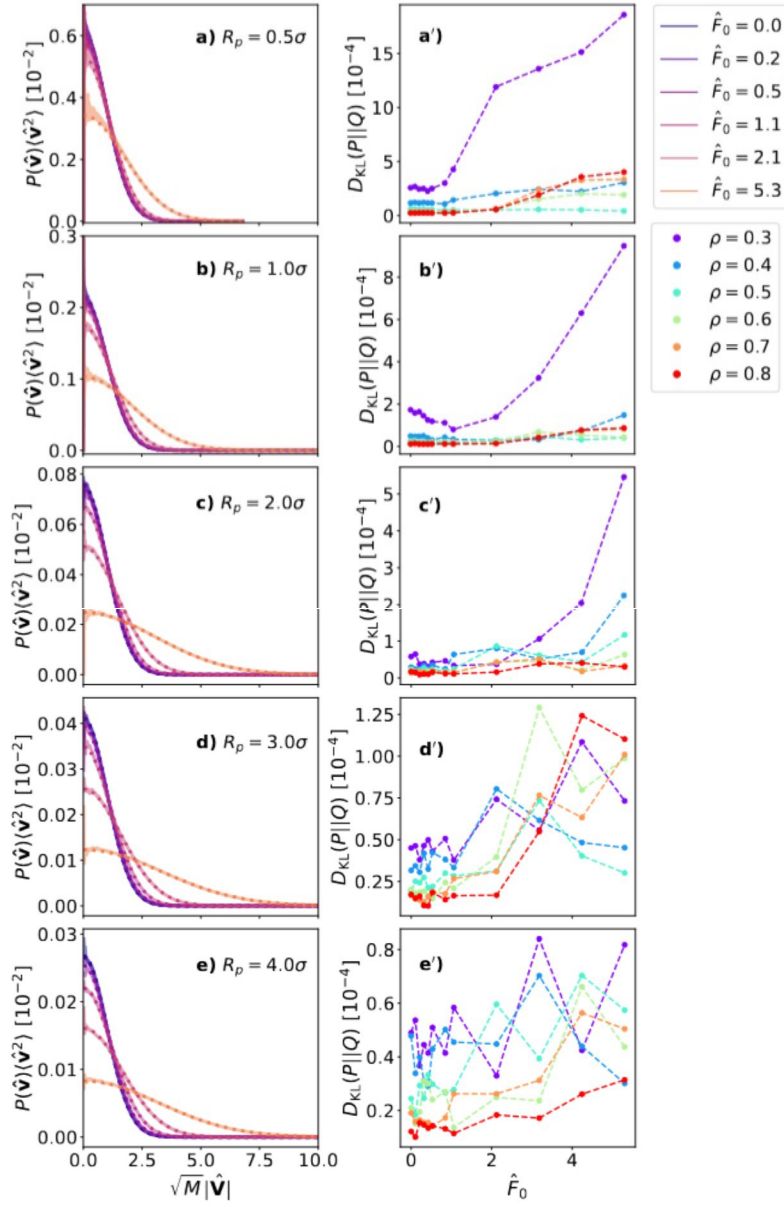


**Figure F.1.:** **a-e)** Velocity distributions of different sized probes immersed in a bath of density  $\rho = 0.8\sigma^{-3}$  for different driving forces  $\hat{F}_0$ . Solid lines show simulation data, whereas dotted lines show zero-centered Gaussian distributions with the same standard deviation for comparison. The x-axis has been rescaled by  $\sqrt{M}$  for better visibility and the x-axis has been rescaled by  $\langle \hat{V}^2 \rangle$ . **a'-e')** Corresponding relative entropies (Eq. (8.9)) between the simulation data and Gaussian distributions with the same standard deviation. Each row corresponds to a different sized probe from Table III.1: **a/a')**  $R_p = 0.5\sigma$ , **b/b')**  $R_p = 1.0\sigma$ , **c/c')**  $R_p = 2.0\sigma$ , **d/d')**  $R_p = 3.0\sigma$ , and **e/e')**  $R_p = 4.0\sigma$ . Densities in the legend are expressed in LJ units of  $\sigma^{-3}$ .

## Active Langevin particle persistence length

The dynamics of active particles can generally be characterized by two parameters: the speed of propulsion and the rotational diffusion time. These two parameters can be used to define a persistence length during which an active particle travels without reorienting. For an active Brownian particle, this persistence length is typically defined as  $\ell_p = v_0/((d-1)D_R)$ , where  $v_0$  is the propulsion velocity,  $d$  is the dimensionality of the system, and  $D_R$  is the rotational diffusion constant. In analogy with this definition, we define the persistence length of an ALP as:

$$\ell_p = \frac{\sqrt{\langle \mathbf{v}^2 \rangle}}{(d-1)D_R}. \quad (\text{G.1})$$

We show the ALP persistence length for different densities as a function of  $\hat{F}_0$  in Fig. G.1.

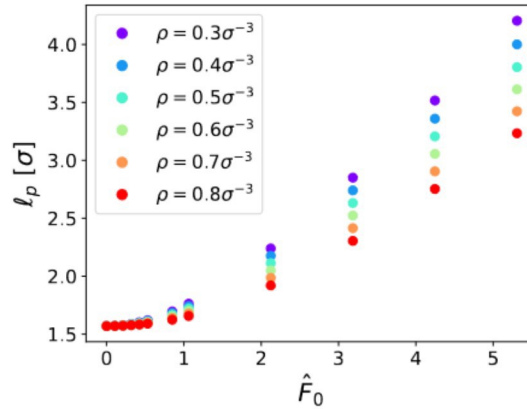


**Figure G.1.:** Persistence length of an ALP for different densities (shown as different colors) as a function of the active force  $\hat{F}_0$ .

From Fig. G.1, we see that  $\ell_p > R_p$  at all active forces for probes of  $R_p \lesssim 1.5$ . This characteristic of the ALPs likely contributes to the qualitatively different behavior we saw for probes of radii  $R_p = 0.5\sigma$  and  $R_p = 1.0\sigma$  in Part III. Furthermore,  $\ell_p$  grows with the active force of the ALPs. In Chapter 11, we saw that the kinetic temperature difference between the probe and the bath ALPs exhibits non-monotonic

behavior as a function of probe radius, reaching a maximum at some probe radius  $R_{\max}$ . We found in Chapter 11 that the value of  $R_{\max}$  decreases with increasing bath activity (see Fig. 11.3a)); therefore, given the opposite behavior of  $\ell_p$  and  $R_{\max}$  as function of  $\hat{F}_0$ , we conclude that the persistence length of the ALPs cannot explain the non-monotonic behavior of the kinetic temperature difference.

## Spherical harmonics calculation

To calculate the spherical harmonics of the ALP bath, we transform the coordinates of all our bath ALPs into a coordinate system in which  $\hat{z}$  aligns with  $\mathbf{V}$ , the instantaneous velocity of the probe. We then calculate the spherical harmonics ( $Y_l^m(\mathbf{r}_i/r_i)$ ) of each particle  $i$  within radius  $r = 10\sigma$  from the center of the probe. Each particle  $i$  is assigned to a spherical shell  $\delta r$  according to its distance from the center of the probe, where the total number of shells is 100. The spherical shells have volume  $\mathcal{V}(r) = 4/3\pi((r + \delta r/2)^3 - (r - \delta r/2)^3)$ , where  $\delta r$  is the radial distance between two shells. In any given shell, we then sum the  $Y_l^m(\mathbf{r}_i/r_i)$  values over all particles within the bin, giving us Eq. (13.2) of the main text. We do these spherical harmonics calculations for values of  $l$  and  $m$  up to  $l = 12$ .

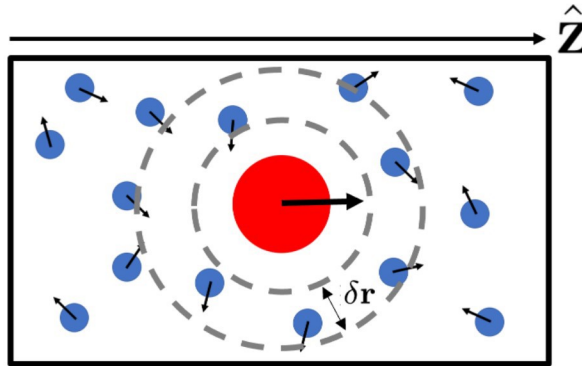


**Figure H.1.:** Schematic diagram describing the calculation of the ALP bath spherical harmonics in the vicinity of the probe.

# Correlations and density in an active Langevin particle bath

In Chapter 11, we saw that the kinetic temperature difference between the probe and the bath ALPs exhibits non-monotonic behavior as a function of probe radius, reaching a maximum at some probe radius  $R_{\max}$ . We have already shown that the persistence length of the bath ALPs cannot explain this non-monotonic behavior in Appendix G. For baths of all densities and activities, we found the value of  $R_{\max} \approx 3.0\sigma$ . Therefore, we would like to assess whether the length  $3.0\sigma$  somehow characterizes the bath dynamics. Here, we specifically investigate correlations among ALPs.

For the purpose of this investigation, we examine a bath of ALPs (described by Eq. 9.1), absent of the probe. For a single, randomly selected ALP, we then calculate the alignment of other ALPs in the vicinity using Eq. 13.3. In Eq. 13.3, we simply replace  $\mathbf{V}$  with  $\mathbf{v}_1$ , the velocity of the randomly selected ALP (see Fig. I.1a)). We are especially interested in correlations between  $\mathbf{v}_1$  and the velocities of ALPs which are positioned on the axis perpendicular to  $\mathbf{v}_1$ . Correlations amongst these perpendicularly located particles would allow for coordinated pushing of the probe. Therefore, in Fig. I.1b), we specifically examine the quantity:

$$\langle \mathbf{v}_1 \cdot \mathbf{v} \rangle_{\perp}(r) = \frac{1}{\rho(r)} \sum_{i \in \delta \mathbf{r}} \mathbf{v}_1 \cdot \mathbf{v} \frac{|\mathbf{v}_1 \times \mathbf{r}_i|}{|\mathbf{v}_1| |\mathbf{r}_i|}, \quad (\text{I.1})$$

where  $\mathbf{r}_i$  is the distance vector from ALP  $i$  to the selected ALP.

In agreement with our results in Chapter 12, we see that the motion of particles in a passive bath is uncorrelated. In an active bath, we see that the velocities of the ALPs do become correlated, again in agreement with Chapter 12. We find these correlations up to a length of  $\sim 1.0\sigma$ . A significant amount of these correlations are among particles positioned along the axis perpendicular to  $\mathbf{v}_1$  (see Fig. I.1b)). On larger length scales, the ALPs become uncorrelated again. The correlation length scale of  $\sim 1.0\sigma$  does not match the value of  $R_{\max} \approx 3.0\sigma$  which we saw in Chapter 11. Therefore, these correlations cannot explain such a value of  $R_{\max}$ .



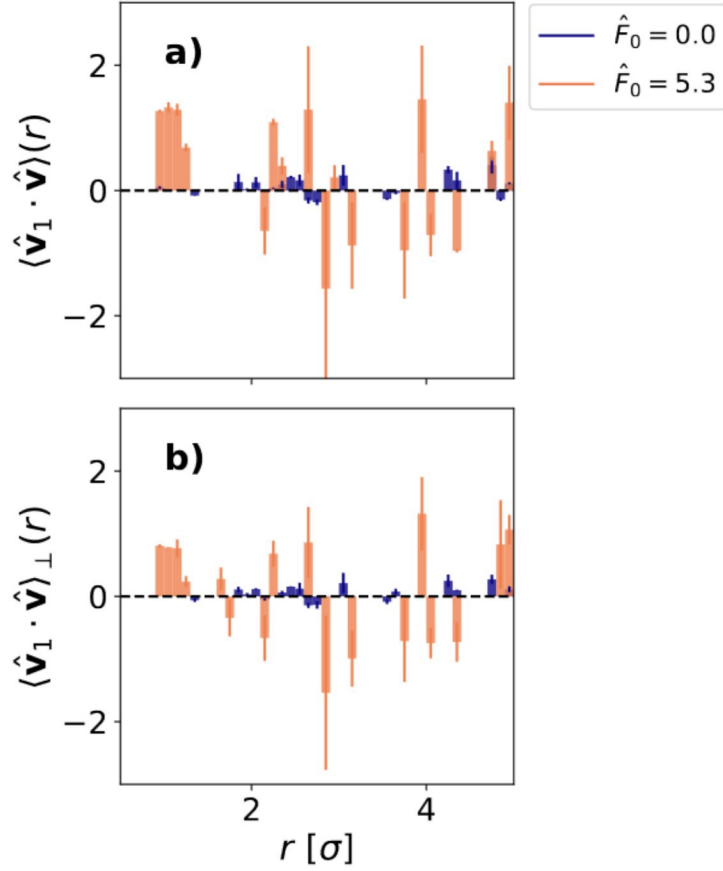


**Figure I.1.:** Velocity alignment among active Langevin particles in a bath of global density  $\rho_0 = 0.8\sigma^{-3}$ . **a)** Alignment of ALP velocities with that of a randomly chosen ALP ( $\langle \mathbf{v}_1 \cdot \mathbf{v} \rangle(r)$ , see Eq. 13.3). **b)** Alignment of ALP velocities located on the axis perpendicular to the velocity of a randomly chosen ALP ( $\langle \mathbf{v}_1 \cdot \mathbf{v} \rangle_{\perp}(r)$ , see Eq. I.1).

## Peclet number as a function of drag force

In Section 16.1, we define the Peclet number  $Pe = \langle V_x \rangle / V_{\text{diff}}$  for the dragged probe, with  $V_{\text{diff}} = D_{\text{eff}} / R_p$ . Given that the average force exerted on the probe can be related to its average velocity through Eq. (16.5), we can rewrite the Peclet number in terms of  $\tilde{F}_{\text{ext}}$  as  $Pe = \mu_{\text{Drag}} \tilde{F}_{\text{ext}} / V_{\text{diff}}$ . We found in Section 16.1 that, for both a probe immersed in an passive and an active bath,  $\mu_{\text{Drag}}$  is a constant within the linear response regime. Therefore, we expect that  $Pe$  is proportional to  $\tilde{F}_{\text{ext}}$  with proportionality constant  $\mu_{\text{Drag}} / V_{\text{diff}}$  within the linear response regime. This is indeed what we see in Fig. J.1.

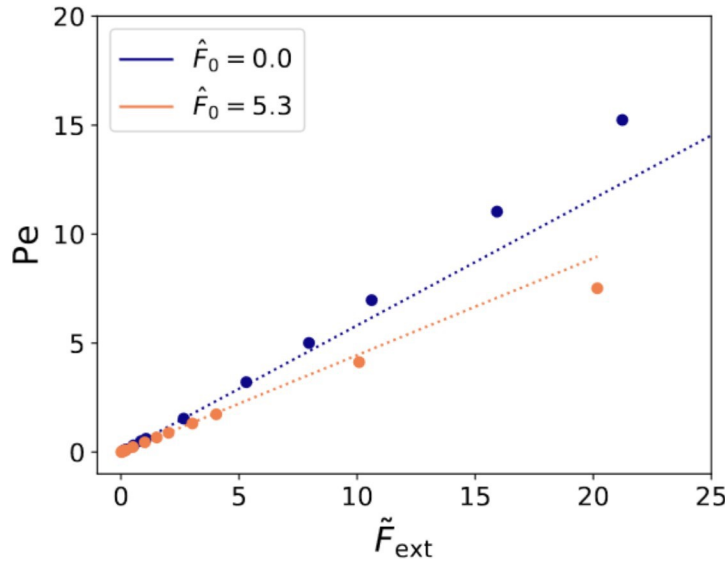


**Figure J.1.:** Peclet number ( $Pe$ ) as a function of the renormalized external drag force ( $\tilde{F}_{\text{ext}}$ ). The dotted lines show  $Pe = \mu_{\text{Drag}} \tilde{F}_{\text{ext}} / V_{\text{diff}}$  in the linear response regime, where  $\mu_{\text{Drag}}$  is constant.

# Bibliography

- [1]R. Brown. “A brief account of microscopical observations made in the months of June, July and August 1827, on the particles contained in the pollen of plants; and on the general existence of active molecules in organic and inorganic bodies”. In: *The Philosophical Magazine Series 2* 4.21 (1828), pp. 161–173. DOI: 10.1080/14786442808674769. eprint: <https://doi.org/10.1080/14786442808674769>.
- [2]A. Einstein. “The motion of elements suspended in static liquids as claimed in the molecular kinetic theory of heat”. In: *Annalen der Physik* 17.8 (1905), pp. 549–560.
- [3]A. Einstein. “Zur Theorie der Brownschen Bewegung”. In: *Annalen der Physik* 324.2 (1906), pp. 371–381.
- [4]M. von Smoluchowski. “Zur kinetischen Theorie der Brownschen Molekularbewegung und der Suspensionen”. In: *Annalen der Physik* 326.14 (1906), pp. 756–780.
- [5]P. Langevin. “The theory of brownian motion”. In: *Comptes Rendus Hebdomadaires des Seances de L'Academie des Sciences* 146 (1908), pp. 530–533.
- [6]G. G. Stokes. “On the effect of the internal friction of fluids on the motion of pendulums”. In: *Transactions of the Cambridge Philosophical Society* 9 (1851), p. 8.
- [7]A. Einstein. “Eine neue Bestimmung der Moleküldimensionen”. In: *Annalen der Physik* 19.289 (1906).
- [8]W. Sutherland. “LXXV. A dynamical theory of diffusion for non-electrolytes and the molecular mass of albumin”. In: *The London, Edinburgh, and Dublin Philosophical Magazine and Journal of Science* 9.54 (1905), pp. 781–785. DOI: 10.1080/14786440509463331. eprint: <https://doi.org/10.1080/14786440509463331>.
- [9]R. Zwanzig. *Nonequilibrium Statistical Physics*. Oxford University Press, 2001.
- [10]H. Mori. “Transport, Collective Motion, and Brownian Motion”. In: *Progress of Theoretical Physics* 33.3 (1965), pp. 423–455. DOI: 10.1143/PTP.33.423. eprint: <https://academic.oup.com/ptp/article-pdf/33/3/423/5428510/33-3-423.pdf>.
- [11]R. Zwanzig. “Memory Effects in Irreversible Thermodynamics”. In: *Phys. Rev.* 124 (4 1961), pp. 983–992. DOI: 10.1103/PhysRev.124.983.
- [12]V. Klippenstein, M. Tripathy, G. Jung, F. Schmid, and N. van der Vegt. “Introducing Memory in Coarse-Grained Simulations”. In: *J. Phys. Chem. B* 125 (2021), p. 4931.
- [13]T. Kinjo and S.-a. Hyodo. “Equation of motion for coarse-grained simulation based on microscopic description”. In: *Phys. Rev. E* 75 (5 2007), p. 051109. DOI: 10.1103/PhysRevE.75.051109.

- [14]F. Glatzel and T. Schilling. “The interplay between memory and potentials of mean force: A discussion on the structure of equations of motion for coarse-grained observables”. In: *Europhysics Letters* 136.3 (2022), p. 36001. DOI: 10.1209/0295-5075/ac35ba.
- [15]T. Schilling. “Coarse-grained modelling out of equilibrium”. In: *Physics Reports* 972 (2022), pp. 1–45. DOI: 10.1016/j.physrep.2022.04.006.
- [16]H. Vroylandt and P. Monmarché. “Position-dependent memory kernel in generalized Langevin equations: Theory and numerical estimation”. In: *The Journal of Chemical Physics* 156.24 (2022), p. 244105. DOI: 10.1063/5.0094566.
- [17]H. K. Shin, C. Kim, P. Talkner, and E. K. Lee. “Brownian motion from molecular dynamics”. In: *Chemical Physics* 375.2-3 (2010), pp. 316–326. DOI: 10.1016/j.chemphys.2010.05.019.
- [18]B. Schnurr, F. Gittes, F. C. MacKintosh, and C. F. Schmidt. “Determining Microscopic Viscoelasticity in Flexible and Semiflexible Polymer Networks from Thermal Fluctuations”. In: *Macromolecules* 30.25 (1997), pp. 7781–7792. DOI: 10.1021/ma970555n. eprint: <https://doi.org/10.1021/ma970555n>.
- [19]J. Fricks, L. Yao, T. C. Elston, and M. G. Forest. “Time-Domain Methods for Diffusive Transport in Soft Matter”. In: *SIAM Journal on Applied Mathematics* 69.5 (2009), pp. 1277–1308. DOI: 10.1137/070695186. eprint: <https://doi.org/10.1137/070695186>.
- [20]A. Carof, R. Vuilleumier, and B. Rotenberg. “Two algorithms to compute projected correlation functions in molecular dynamics simulations”. In: *The Journal of Chemical Physics* 140.12 (2014), p. 124103. DOI: 10.1063/1.4868653. eprint: <https://doi.org/10.1063/1.4868653>.
- [21]D. Lesnicki, R. Vuilleumier, A. Carof, and B. Rotenberg. “Molecular Hydrodynamics from Memory Kernels”. In: *Phys. Rev. Lett.* 116 (14 2016), p. 147804. DOI: 10.1103/PhysRevLett.116.147804.
- [22]H. Lei, N. A. Baker, and X. Li. “Data-driven parameterization of the generalized Langevin equation”. In: *Proceedings of the National Academy of Sciences* 113.50 (2016), pp. 14183–14188. DOI: 10.1073/pnas.1609587113.
- [23]N. Bockius, J. Shea, G. Jung, F. Schmid, and M. Hanke. “Model reduction techniques for the computation of extended Markov parameterizations for generalized Langevin equations”. In: *J. Phys.: Cond. Matter* 33 (2021), p. 214003.
- [24]G. Jung, M. Hanke, and F. Schmid. “Iterative Reconstruction of Memory Kernels”. In: *Journal of Chemical Theory and Computation* 13.6 (2017), pp. 2481–2488. DOI: 10.1021/acs.jctc.7b00274.
- [25]R. Kubo. “The fluctuation-dissipation theorem”. In: *Reports on Progress in Physics* 29.1 (1966), pp. 255–284. DOI: 10.1088/0034-4885/29/1/306.
- [26]D. T. N. Chen, A. W. C. Lau, L. A. Hough, et al. “Fluctuations and Rheology in Active Bacterial Suspensions”. In: *Phys. Rev. Lett.* 99 (14 2007), p. 148302. DOI: 10.1103/PhysRevLett.99.148302.

- [27]A. W. C. Lau and T. C. Lubensky. “Fluctuating hydrodynamics and microrheology of a dilute suspension of swimming bacteria”. In: *Phys. Rev. E* 80 (1 2009), p. 011917. DOI: 10.1103/PhysRevE.80.011917.
- [28]S. Steffenoni, K. Kroy, and G. Falasco. “Interacting Brownian dynamics in a nonequilibrium particle bath”. In: *Physical Review E* 94 (2016). DOI: 10.1103/PhysRevE.94.062139.
- [29]C. Maggi, M. Paoluzzi, L. Angelani, and R. Leonardo. “Memory-less response and violation of the fluctuation-dissipation theorem in colloids suspended in an active bath”. In: *Scientific Reports* 7 (2017). DOI: 10.1038/s41598-017-17900-2.
- [30]A. Argun, A.-R. Moradi, E. ğ. Pin çe, et al. “Non-Boltzmann stationary distributions and nonequilibrium relations in active baths”. In: *Phys. Rev. E* 94 (6 2016), p. 062150. DOI: 10.1103/PhysRevE.94.062150.
- [31]C. Maggi, M. Paoluzzi, N. Pellicciotta, et al. “Generalized Energy Equipartition in Harmonic Oscillators Driven by Active Baths”. In: *Phys. Rev. Lett.* 113 (23 2014), p. 238303. DOI: 10.1103/PhysRevLett.113.238303.
- [32]D. Loi, S. Mossa, and L. F. Cugliandolo. “Effective temperature of active matter”. In: *Phys. Rev. E* 77 (5 2008), p. 051111. DOI: 10.1103/PhysRevE.77.051111.
- [33]G. Jung and F. Schmid. “Fluctuation-dissipation relations far from equilibrium: a case study”. In: *Soft matter* 17.26 (2021), pp. 6413–6425. DOI: 10.1039/d1sm00521a.
- [34]H. Kramers. “Brownian motion in a field of force and the diffusion model of chemical reactions”. In: *Physica* 7.4 (1940), pp. 284–304. DOI: [https://doi.org/10.1016/S0031-8914\(40\)90098-2](https://doi.org/10.1016/S0031-8914(40)90098-2).
- [35]J. E. Moyal. “Stochastic Processes and Statistical Physics”. In: *J. R. Stat. Soc. Ser. B (Methodol.)* 11 (1949), pp. 150–210.
- [36]D. Forster. *Hydrodynamic Fluctuations, Broken Symmetry, And Correlation Functions*. CRC Press, 1975.
- [37]D. Chandler. *Introduction to modern statistical mechanics*. Oxford University Press, 1987.
- [38]R. Kubo. “Statistical-Mechanical Theory of Irreversible Processes. I. General Theory and Simple Applications to Magnetic and Conduction Problems”. In: *Journal of the Physical Society of Japan* 12.6 (1957), pp. 570–586. DOI: 10.1143/JPSJ.12.570. eprint: <https://doi.org/10.1143/JPSJ.12.570>.
- [39]G. S. Agarwal. “Fluctuation-dissipation theorems for systems in non-thermal equilibrium and applications”. In: *Zeitschrift fur Physik* 252.1 (1972), pp. 25–38. DOI: 10.1007/BF01391621.
- [40]T. Speck and U. Seifert. “Extended fluctuation-dissipation theorem for soft matter in stationary flow”. In: *Phys. Rev. E* 79 (4 2009), p. 040102. DOI: 10.1103/PhysRevE.79.040102.

- [41]U. Seifert and T. Speck. “Fluctuation-dissipation theorem in nonequilibrium steady states”. In: *EPL (Europhysics Letters)* 89.1 (2010), p. 10007. DOI: 10.1209/0295-5075/89/10007.
- [42]R. Larson. *The structure and rheology of complex fluids*. Oxford University Press, 1999.
- [43]F. MacKintosh and C. Schmidt. “Microrheology”. In: *Current Opinion in Colloid and Interface Science* 4.4 (1999), pp. 300–307. DOI: [https://doi.org/10.1016/S1359-0294\(99\)90010-9](https://doi.org/10.1016/S1359-0294(99)90010-9).
- [44]T. A. Waigh. “Microrheology of complex fluids”. In: *Reports on Progress in Physics* 68.3 (2005), p. 685. DOI: 10.1088/0034-4885/68/3/R04.
- [45]P. Cicuta and A. M. Donald. “Microrheology: a review of the method and applications”. In: *Soft Matter* 3 (12 2007), pp. 1449–1455. DOI: 10.1039/B706004C.
- [46]L. G. Wilson and W. C. K. Poon. “Small-world rheology: an introduction to probe-based active microrheology”. In: *Phys. Chem. Chem. Phys.* 13 (22 2011), pp. 10617–10630. DOI: 10.1039/C0CP01564D.
- [47]R. N. Zia. “Active and Passive Microrheology: Theory and Simulation”. In: *Annual Review of Fluid Mechanics* 50.1 (2018), pp. 371–405. DOI: 10.1146/annurev-fluid-122316-044514. eprint: <https://doi.org/10.1146/annurev-fluid-122316-044514>.
- [48]I. Carpen and J. Brady. “Microrheology of colloidal dispersions by Brownian dynamics simulations”. In: *Journal of Rheology - J RHEOL* 49 (2005). DOI: 10.1122/1.2085174.
- [49]D. Winter, J. Horbach, P. Virnau, and K. Binder. “Active Nonlinear Microrheology in a Glass-Forming Yukawa Fluid”. In: *Phys. Rev. Lett.* 108 (2 2012), p. 028303. DOI: 10.1103/PhysRevLett.108.028303.
- [50]A. M. Puertas and T. Voigtmann. “Microrheology of colloidal systems”. In: *Journal of Physics: Condensed Matter* 26.24 (2014), p. 243101. DOI: 10.1088/0953-8984/26/24/243101.
- [51]C. J. Harrer, D. Winter, J. Horbach, M. Fuchs, and T. Voigtmann. “Force-induced diffusion in microrheology”. In: *Journal of Physics: Condensed Matter* 24.46 (2012), p. 464105. DOI: 10.1088/0953-8984/24/46/464105.
- [52]T. Wang and M. Sperl. “Thinning and thickening in active microrheology”. In: *Physical Review E* 93.2 (2016). DOI: 10.1103/physreve.93.022606.
- [53]V. Buchholtz and T. Pöschel. “Interaction of a granular stream with an obstacle”. In: *Granular Matter* 1 (1997), pp. 33–41.
- [54]T. Wang, M. Grob, A. Zippelius, and M. Sperl. “Active microrheology of driven granular particles”. In: *Phys. Rev. E* 89 (4 2014), p. 042209. DOI: 10.1103/PhysRevE.89.042209.
- [55]T. Vicsek and A. Zafeiris. “Collective motion”. In: *Physics Reports* 517.3-4 (2012), pp. 71–140. DOI: 10.1016/j.physrep.2012.03.004.

- [56] T. Vicsek, A. Czirók, E. Ben-Jacob, I. Cohen, and O. Shochet. “Novel Type of Phase Transition in a System of Self-Driven Particles”. In: *Phys. Rev. Lett.* 75 (6 1995), pp. 1226–1229. DOI: 10.1103/PhysRevLett.75.1226.
- [57] H. C. Berg and D. A. Brown. “Chemotaxis in *Escherichia coli* analysed by Three-dimensional Tracking”. In: *Nature* 239.5374 (1972), pp. 500–504. DOI: 10.1038/239500a0.
- [58] A. Callegari and G. Volpe. “Numerical Simulations of Active Brownian Particles”. In: *Flowing Matter*. Ed. by F. Toschi and M. Sega. Cham: Springer International Publishing, 2019, pp. 211–238. DOI: 10.1007/978-3-030-23370-9\_7.
- [59] H. Löwen. “Inertial effects of self-propelled particles: From active Brownian to active Langevin motion”. In: *The Journal of Chemical Physics* 152.4 (2020), p. 040901. DOI: 10.1063/1.5134455.
- [60] S. C. Takatori and J. F. Brady. “Inertial effects on the stress generation of active fluids”. In: *Phys. Rev. Fluids* 2 (9 2017), p. 094305. DOI: 10.1103/PhysRevFluids.2.094305.
- [61] C. Scholz, S. Jahanshahi, A. Ldov, and H. Löwen. “Inertial delay of self-propelled particles”. In: *Nature Communications* 9 (2018), p. 5156. DOI: 10.1038/s41467-018-07596-x.
- [62] S. Shankar and M. C. Marchetti. “Hidden entropy production and work fluctuations in an ideal active gas”. In: *Phys. Rev. E* 98 (2 2018), p. 020604. DOI: 10.1103/PhysRevE.98.020604.
- [63] A. Baskaran and M. C. Marchetti. “Enhanced Diffusion and Ordering of Self-Propelled Rods”. In: *Physical review letters* 101 (2009), p. 268101. DOI: 10.1103/PhysRevLett.101.268101.
- [64] S. Mandal, B. Liebchen, and H. Löwen. “Motility-Induced Temperature Difference in Coexisting Phases”. In: *Phys. Rev. Lett.* 123 (22 2019), p. 228001. DOI: 10.1103/PhysRevLett.123.228001.
- [65] S. Das, G. Gompper, and R. Winkler. “Local stress and pressure in an inhomogeneous system of spherical active Brownian particles”. In: *Scientific Reports* 9 (2019), p. 6608. DOI: 10.1038/s41598-019-43077-x.
- [66] A. R. Sprenger, S. Jahanshahi, A. V. Ivlev, and H. Löwen. “Time-dependent inertia of self-propelled particles: The Langevin rocket”. In: *Phys. Rev. E* 103 (4 2021), p. 042601. DOI: 10.1103/PhysRevE.103.042601.
- [67] U. Basu, S. N. Majumdar, A. Rosso, and G. Schehr. “Active Brownian motion in two dimensions”. In: *Physical Review E* 98.6 (2018). DOI: 10.1103/physreve.98.062121.
- [68] C. Bechinger, R. Di Leonardo, H. Löwen, et al. “Active particles in complex and crowded environments”. In: *Rev. Mod. Phys.* 88 (4 2016), p. 045006. DOI: 10.1103/RevModPhys.88.045006.

- [69] J. R. Howse, R. A. L. Jones, A. J. Ryan, et al. “Self-Motile Colloidal Particles: From Directed Propulsion to Random Walk”. In: *Phys. Rev. Lett.* 99 (4 2007), p. 048102. DOI: 10.1103/PhysRevLett.99.048102.
- [70] M. E. Cates and J. Tailleur. “Motility-Induced Phase Separation”. In: *Annual Review of Condensed Matter Physics* 6.1 (2015), pp. 219–244. DOI: 10.1146/annurev-conmatphys-031214-014710.
- [71] J. Stenhammar, A. Tiribocchi, R. J. Allen, D. Marenduzzo, and M. E. Cates. “Continuum Theory of Phase Separation Kinetics for Active Brownian Particles”. In: *Phys. Rev. Lett.* 111 (14 2013), p. 145702. DOI: 10.1103/PhysRevLett.111.145702.
- [72] G. S. Redner, M. F. Hagan, and A. Baskaran. “Structure and Dynamics of a Phase-Separating Active Colloidal Fluid”. In: *Phys. Rev. Lett.* 110 (5 2013), p. 055701. DOI: 10.1103/PhysRevLett.110.055701.
- [73] L. Caprini, R. K. Gupta, and H. Löwen. “Role of rotational inertia for collective phenomena in active matter”. In: *Phys. Chem. Chem. Phys.* 24 (40 2022), pp. 24910–24916. DOI: 10.1039/D2CP02940E.
- [74] M. J. Schnitzer. “Theory of continuum random walks and application to chemotaxis”. In: *Phys. Rev. E* 48 (4 1993), pp. 2553–2568. DOI: 10.1103/PhysRevE.48.2553.
- [75] J. Bialké, H. Löwen, and T. Speck. “Microscopic theory for the phase separation of self-propelled repulsive disks”. In: *EPL (Europhysics Letters)* 103.3 (2013), p. 30008. DOI: 10.1209/0295-5075/103/30008.
- [76] J. Palacci, S. Sacanna, S.-H. Kim, et al. “Light-activated self-propelled colloids”. In: *Philosophical transactions. Series A, Mathematical, physical, and engineering sciences* 372 (2014). DOI: 10.1098/rsta.2013.0372.
- [77] J. Stenhammar, D. Marenduzzo, R. J. Allen, and M. E. Cates. “Phase behaviour of active Brownian particles: the role of dimensionality”. In: *Soft Matter* 10 (10 2014), pp. 1489–1499. DOI: 10.1039/C3SM52813H.
- [78] X. Yang, M. L. Manning, and M. C. Marchetti. “Aggregation and Segregation of Confined Active Particles”. In: *Soft matter* 10 (2014). DOI: 10.1039/c4sm00927d.
- [79] A. P. Berke, L. Turner, H. C. Berg, and E. Lauga. “Hydrodynamic Attraction of Swimming Microorganisms by Surfaces”. In: *Physical Review Letters* 101.3 (2008). DOI: 10.1103/physrevlett.101.038102.
- [80] G. Li and J. X. Tang. “Accumulation of Microswimmers near a Surface Mediated by Collision and Rotational Brownian Motion”. In: *Phys. Rev. Lett.* 103 (7 2009), p. 078101. DOI: 10.1103/PhysRevLett.103.078101.
- [81] G. Li, J. Besson, L. Nisimova, et al. “Accumulation of swimming bacteria near a solid surface”. In: *Phys. Rev. E* 84 (4 2011), p. 041932. DOI: 10.1103/PhysRevE.84.041932.
- [82] B. Ezhilan and D. Saintillan. “Transport of a dilute active suspension in pressure-driven channel flow”. In: *Journal of Fluid Mechanics* 777 (2015), pp. 482–522. DOI: 10.1017/jfm.2015.372.



- [83]K. Schaar, A. Zöttl, and H. Stark. “Detention Times of Microswimmers Close to Surfaces: Influence of Hydrodynamic Interactions and Noise”. In: *Phys. Rev. Lett.* 115 (3 2015), p. 038101. DOI: 10.1103/PhysRevLett.115.038101.
- [84]A. Duzgun and J. V. Selinger. “Active Brownian particles near straight or curved walls: Pressure and boundary layers”. In: *Physical Review E* 97.3 (2018). DOI: 10.1103/physreve.97.032606.
- [85]V. Kantsler, J. Dunkel, M. Polin, and R. Goldstein. “Ciliary contact interactions dominate surface scattering of swimming eukaryotes”. In: *Proceedings of the National Academy of Sciences of the United States of America* 110 (2013). DOI: 10.1073/pnas.1210548110.
- [86]S. C. Takatori, W. Yan, and J. F. Brady. “Swim Pressure: Stress Generation in Active Matter”. In: *Phys. Rev. Lett.* 113 (2 2014), p. 028103. DOI: 10.1103/PhysRevLett.113.028103.
- [87]T. Speck and A. Jayaram. “Vorticity Determines the Force on Bodies Immersed in Active Fluids”. In: *Phys. Rev. Lett.* 126 (13 2021), p. 138002. DOI: 10.1103/PhysRevLett.126.138002.
- [88]W. Yan and J. F. Brady. *The force on a body in active matter*. 2015. arXiv: 1510.07731 [cond-mat.soft].
- [89]W. Yan and J. F. Brady. “The curved kinetic boundary layer of active matter”. In: *Soft Matter* 14.2 (2018), pp. 279–290. DOI: 10.1039/c7sm01643c.
- [90]X.-L. Wu and A. Libchaber. “Particle Diffusion in a Quasi-Two-Dimensional Bacterial Bath”. In: *Phys. Rev. Lett.* 84 (13 2000), pp. 3017–3020. DOI: 10.1103/PhysRevLett.84.3017.
- [91]K. C. Leptos, J. S. Guasto, J. P. Gollub, A. I. Pesci, and R. E. Goldstein. “Dynamics of Enhanced Tracer Diffusion in Suspensions of Swimming Eukaryotic Microorganisms”. In: *Phys. Rev. Lett.* 103 (19 2009), p. 198103. DOI: 10.1103/PhysRevLett.103.198103.
- [92]G. Foffano, J. S. Lintuvuori, K. Stratford, M. E. Cates, and D. Marenduzzo. “Colloids in Active Fluids: Anomalous Microrheology and Negative Drag”. In: *Phys. Rev. Lett.* 109 (2 2012), p. 028103. DOI: 10.1103/PhysRevLett.109.028103.
- [93]G. L. Miño, J. Dunstan, A. Rousselet, E. Clément, and R. Soto. “Induced diffusion of tracers in a bacterial suspension: theory and experiments”. In: *Journal of Fluid Mechanics* 729 (2013), pp. 423–444. DOI: 10.1017/jfm.2013.304.
- [94]A. Suma, L. Cugliandolo, and G. Gonnella. “Tracer motion in an active dumbbell fluid”. In: *Journal of Statistical Mechanics: Theory and Experiment* 2016 (2016), p. 054029. DOI: 10.1088/1742-5468/2016/05/054029.
- [95]S. Chaki and R. Chakrabarti. “Effects of active fluctuations on energetics of a colloidal particle: Superdiffusion, dissipation and entropy production”. In: *Physica A: Statistical Mechanics and its Applications* 530 (2019), p. 121574. DOI: 10.1016/j.physa.2019.121574.

- [96]C. Maes. “Fluctuating Motion in an Active Environment”. In: *Phys. Rev. Lett.* 125 (20 2020), p. 208001. DOI: 10.1103/PhysRevLett.125.208001.
- [97]O. Granek, Y. Kafri, and J. Tailleur. *The Anomalous Transport of Tracers in Active Baths*. 2022. arXiv: 2108.11970 [cond-mat.soft].
- [98]S. Ye, P. Liu, F. Ye, K. Chen, and M. Yang. “Active noise experienced by a passive particle trapped in an active bath”. In: *Soft Matter* 16 (19 2020), pp. 4655–4660. DOI: 10.1039/D0SM00006J.
- [99]M. Knežević, L. Podgurski, and H. Stark. “Oscillatory active microrheology of active suspensions”. In: *Scientific Reports* 11 (2021). DOI: 10.1038/s41598-021-02103-7.
- [100]M. Knežević and H. Stark. “Effective Langevin equations for a polar tracer in an active bath”. In: *New Journal of Physics* 22.11 (2020), p. 113025. DOI: 10.1088/1367-2630/abc91e.
- [101]J. Reichert and T. Voigtmann. “Tracer dynamics in crowded active-particle suspensions”. In: *Soft Matter* 17 (46 2021), pp. 10492–10504. DOI: 10.1039/D1SM01092A.
- [102]G. Miño, T. E. Mallouk, T. Darnige, et al. “Enhanced Diffusion due to Active Swimmers at a Solid Surface”. In: *Phys. Rev. Lett.* 106 (4 2011), p. 048102. DOI: 10.1103/PhysRevLett.106.048102.
- [103]A. Datta, P. Pietzonka, and A. C. Barato. “Second Law for Active Heat Engines”. In: *Physical Review X* 12.3 (2022). DOI: 10.1103/physrevx.12.031034.
- [104]P. Pietzonka, É. Fodor, C. Lohrmann, M. E. Cates, and U. Seifert. “Autonomous Engines Driven by Active Matter: Energetics and Design Principles”. In: *Physical Review X* 9.4 (2019). DOI: 10.1103/physrevx.9.041032.
- [105]Q. Martinet, A. Aubret, and J. Palacci. *Rotation Control, Interlocking and Self-positioning of Active Cogwheels*. 2022. DOI: 10.48550/ARXIV.2201.03333.
- [106]M. Trivedi, D. Saxena, W. K. Ng, R. Sapienza, and G. Volpe. “Self-organized lasers from reconfigurable colloidal assemblies”. In: *Nature Physics* 18.8 (2022), pp. 939–944. DOI: 10.1038/s41567-022-01656-2.
- [107]B. J. Alder and T. E. Wainwright. “Studies in Molecular Dynamics. I. General Method”. In: *The Journal of Chemical Physics* 31.2 (1959), pp. 459–466. DOI: 10.1063/1.1730376. eprint: <https://doi.org/10.1063/1.1730376>.
- [108]L. Verlet. “Computer “Experiments” on Classical Fluids. I. Thermodynamical Properties of Lennard-Jones Molecules”. In: *Phys. Rev.* 159 (1 1967), pp. 98–103. DOI: 10.1103/PhysRev.159.98.
- [109]D. Frenkel and B. Smit. *Understanding molecular simulation*. Elsevier, 2002.
- [110]M. Allen and D. Tildesley. *Computer simulation of liquids*. Clarendon Press, 1987.
- [111]S. Plimpton. *Fast Parallel Algorithms for Short-Range Molecular Dynamics*. 1995.
- [112]J. D. Weeks, D. Chandler, and H. C. Andersen. “Role of Repulsive Forces in Determining the Equilibrium Structure of Simple Liquids”. In: *J. Phys. Chem.* 54.12 (1971), pp. 5237–5247. DOI: 10.1063/1.1674820.

- [113]G. Ciccotti and G. Jacucci. “Direct Computation of Dynamical Response by Molecular Dynamics: The Mobility of a Charged Lennard-Jones Particle”. In: *Phys. Rev. Lett.* 35 (12 1975), pp. 789–792. DOI: 10.1103/PhysRevLett.35.789.
- [114]A. Carof, R. Vuilleumier, and B. Rotenberg. “Two algorithms to compute projected correlation functions in molecular dynamics simulations”. In: *The Journal of Chemical Physics* 140.12 (2014), p. 124103. DOI: 10.1063/1.4868653.
- [115]S. Cerasoli, S. Ciliberto, E. Marinari, et al. *Spectral fingerprints of non-equilibrium dynamics: The case of a Brownian gyrator*. 2022. DOI: 10.48550/ARXIV.2201.04903.
- [116]J. P. Gonzalez, J. C. Neu, and S. W. Teitsworth. “Experimental metrics for detection of detailed balance violation”. In: *Phys. Rev. E* 99 (2 2019), p. 022143. DOI: 10.1103/PhysRevE.99.022143.
- [117]B. Lander, J. Mehl, V. Blickle, C. Bechinger, and U. Seifert. “Noninvasive measurement of dissipation in colloidal systems”. In: *Phys. Rev. E* 86 (3 2012), p. 030401. DOI: 10.1103/PhysRevE.86.030401.
- [118]É. Roldán and J. M. R. Parrondo. “Estimating Dissipation from Single Stationary Trajectories”. In: *Phys. Rev. Lett.* 105 (15 2010), p. 150607. DOI: 10.1103/PhysRevLett.105.150607.
- [119]S. K. Manikandan, S. Ghosh, A. Kundu, et al. “Quantitative analysis of non-equilibrium systems from short-time experimental data”. In: *Communications Physics* 4.1 (2021), p. 258. DOI: 10.1038/s42005-021-00766-2.
- [120]B. Guo, S. Ro, A. Shih, et al. *Play. Pause. Rewind. Measuring local entropy production and extractable work in active matter*. 2021. DOI: 10.48550/ARXIV.2105.12707.
- [121]L. Dabelow, S. Bo, and R. Eichhorn. “Irreversibility in Active Matter Systems: Fluctuation Theorem and Mutual Information”. In: *Phys. Rev. X* 9 (2 2019), p. 021009. DOI: 10.1103/PhysRevX.9.021009.
- [122]P. Pietzonka and U. Seifert. “Entropy production of active particles and for particles in active baths”. In: *Journal of Physics A: Mathematical and Theoretical* 51.1 (2017), 01LT01. DOI: 10.1088/1751-8121/aa91b9.
- [123]R. Jeanneret, V. Kantsler, and M. Polin. “Entrainment dominates the interaction of microalgae with micron-sized objects”. In: *Nature Communications* 7 (2016). DOI: 10.1038/ncomms12518.
- [124]Y. B. Dor, S. Ro, Y. Kafri, M. Kardar, and J. Tailleur. “Disordered boundaries destroy bulk phase separation in scalar active matter”. In: *Physical Review E* 105.4 (2022). DOI: 10.1103/physreve.105.044603.
- [125]Z. Peng and J. F. Brady. “Trapped-particle microrheology of active suspensions”. In: *The Journal of Chemical Physics* 157.10 (2022), p. 104119. DOI: 10.1063/5.0108014. eprint: <https://doi.org/10.1063/5.0108014>.
- [126]H. Seyforth, M. Gomez, W. B. Rogers, J. L. Ross, and W. W. Ahmed. “Nonequilibrium fluctuations and nonlinear response of an active bath”. In: *Phys. Rev. Res.* 4 (2 2022), p. 023043. DOI: 10.1103/PhysRevResearch.4.023043.

- [127]E. Burkholder and J. Brady. “Fluctuation-dissipation in active matter”. In: *The Journal of Chemical Physics* 150 (2019), p. 184901. DOI: 10.1063/1.5081725.
- [128]E. W. Burkholder and J. F. Brady. “Nonlinear microrheology of active Brownian suspensions”. In: *Soft Matter* 16 (4 2020), pp. 1034–1046. DOI: 10.1039/C9SM01713E.
- [129]T. Squires and J. Brady. “A simple paradigm for active and nonlinear microrheology”. In: *Physics of Fluids* 17 (2005). DOI: 10.1063/1.1960607.
- [130]Z. Li, X. Bian, X. Li, and G. Karniadakis. “Incorporation of memory effects in coarse-grained modeling via the Mori-Zwanzig formalism”. In: *The Journal of Chemical Physics* 143 (2015), p. 243128. DOI: 10.1063/1.4935490.
- [131]S. Wang, Z. Ma, and W. Pan. “Data-driven coarse-grained modeling of non-equilibrium systems”. In: *Soft Matter* 17 (26 2021), pp. 6404–6412. DOI: 10.1039/D1SM00413A.
- [132]G. Jung, M. Hanke, and F. Schmid. “Generalized Langevin dynamics: construction and numerical integration of non-Markovian particle-based models”. In: *Soft Matter* 14 (46 2018), pp. 9368–9382. DOI: 10.1039/C8SM01817K.
- [133]S. Takatori, R. De Dier, J. Vermant, and J. Brady. “Acoustic trapping of active matter”. In: *Nature Communications* 7 (2016), p. 10694. DOI: 10.1038/ncomms10694.
- [134]M. Caraglio and T. Franosch. “Analytic Solution of an Active Brownian Particle in a Harmonic Well”. In: *Phys. Rev. Lett.* 129 (15 2022), p. 158001. DOI: 10.1103/PhysRevLett.129.158001.
- [135]K. Malakar, A. Das, A. Kundu, K. V. Kumar, and A. Dhar. “Steady state of an active Brownian particle in a two-dimensional harmonic trap”. In: *Phys. Rev. E* 101 (2 2020), p. 022610. DOI: 10.1103/PhysRevE.101.022610.

# Acknowledgements

Where to begin.

First, I would like to thank my parents, for all the hours you put into my education from the beginning. I won't forget the countless hours you spent quizzing me on EK terms (Mom) or explaining to me how a pulley worked (Dad). Without you and all your support, I wouldn't be here.

My sister, for always being one call away and providing me with a funny story about anything or nothing. You never failed to make my day with a call and make me feel less stressed.

Niara, for calling and talking with me every day when I first moved to Germany. You made me feel at home even when I was far away.

To my supervisor, Friederike, for all of your support and encouragement to follow my research interests. I will carry the things I learned from you (both academically and personally) during this PhD process throughout my career and life.

To Gerhard, for all your insights (and code) which helped me throughout my PhD process. Whenever I had doubts about my work, I was always able to go to you for sanity checks and encouragement.

To Maike, without whom I don't think I would have become registered at the university. Thank you for walking around the university with me and helping me search for the offices I needed to find.

To all my work colleagues, but especially Yannick and Ilin. Yannick, for bearing through those master courses with me (throwback to Experimentalphysik 5a, the lab courses, and the 'herpines' project). And (more importantly) for all those many Sundays hiking and playing music, during which we talked about work or anything but work. You kept me sane through COVID. Ilin, for your ability to turn any random subject into an impassioned debate. You never failed to distract me from whatever problem had been pestering me at the moment.

Am I forgetting anyone? Hmmmm... Don't think so... Oh, wait: to Jörn. My rock throughout it all. Thanks for sticking with me through the ups (when I got back cool results) and downs (when I thought nothing worked) that come with a PhD. Thanks for just being there and being you. Thanks for helping me with my "internet problems." Every day with you is a little brighter than one without.

# Jeanine Shea

## Education

**2019 - 2023:** Fast Track PhD in Statistical Physics

*Johannes-Gutenberg University, Mainz, Germany*

Thesis title: Effective equation of motion of a passive particle immersed in an active fluid.

Advisor: Prof. Dr. Friederike Schmid

**2015 - 2019:** Bachelor's Degree in Physics (4.0, *summa cum laude*)

*Bucknell University, Lewisburg, Pennsylvania, USA*

**2015 - 2019:** Bachelor's Degree in French (4.0, *summa cum laude*)

*Bucknell University, Lewisburg, Pennsylvania, USA*

## Research Appointments

**06/2018 - 08/2018:** European Organization for Nuclear Research (CERN)

Topic: Study of misalignment in the H4-VLE beamline of the CERN North Area.

**06/2017 - 08/2017:** Physics and Astronomy Department Research, Bucknell University

Topic: Statistical mechanics in small systems – non-equilibrium thermal systems.

**05/2016 - 08/2016:** National Radio Astronomy Observatory

Topic: The Southern HII region discovery survey.

## Awards

2021-2023: Gutenberg Akademie for Interdisciplinary Excellence

Member: Phi Beta Kappa, Honor Society

Member: Sigma Pi Sigma, Physics Honor Society

2022: Edwards Symposium, Royal Society of Chemistry poster prize

2016, 2017, 2018, 2019: Bucknell University President's Award for distinguished academic achievement

2019: Bucknell University W. Norwood Lowry Prize for physics

2019: Bucknell University Samuel Lewis Ziegler Prize for French

2019: Bucknell University Oliver J. Decker Prize for academic achievement

## Teaching and mentoring

**Tutorials:** Advanced statistical mechanics, Computer in der Wissenschaft, computer simulations in statistical physics.

**Supervision:** Supervision of one bachelor student project.

## Organization of academic events

**2022/3:** Winter semester lecture cycle, SFB TRR146

**2022:** Diversity workshop “Introduction to intersectionality,” SFB TRR146

**2022:** PhD student retreat, SFB TRR146

**2022:** Round table “Globalization and international networking opportunities,” Gutenberg Akademie

**2021:** Round table “Balancing family life and an academic career,” Gutenberg Akademie

**2016:** Pennsylvania young women in physics conference, Bucknell University

## Languages

**English:** Mother tongue

**German:** intermediate written, conversationally fluent

**French:** Diplôme d'études de langue française (DELF) B2

## Programming

**Python**

**C++**

# Publications

Passive probe particle in an active bath: can we tell it is out of equilibrium?  
**J. Shea**, G. Jung, F. Schmid, *Soft Matter* **18**, 6965-6973 (2022).

Model reduction techniques for the computation of extended Markov parameterizations for generalized Langevin equations (Open Access).  
N. Bockius, **J. Shea**, G. Jung, F. Schmid, M. Hanke, *JCMP* **33**, 214003 (2021).

The Southern HII Region Discovery Survey: I. The Bright Catalog.  
T.V. Wenger, J.M. Dickey, C.H. Jordan, D.S. Balsaer, W.P. Armentrout, L.D. Anderson, T.M. Bania, J.R. Dawson, N.M. McClure-Griffiths, **J. Shea**, *Astrophysical Journal Supplement Series* 240:2 (2019).